Search for Nearly Mass Degenerate Charginos and Neutralinos in e^+e^- Collisions

Dissertation

zur Erlangung des Doktorgrades
des Fachbereichs Physik
der Universität Hamburg

vorgelegt von

Carsten Hensel

aus Beckum

Hamburg
2002

Gutachter der Dissertation	:	Prof. Dr. R.-D. Heuer Prof. Dr. B. Naroska
Gutachter der Disputation	:	Prof. Dr. R.-D. Heuer Prof. Dr. F.-W. Büßer
Datum der Disputation	:	28. November 2002
Vorsitzender des Prüfungsausschusses	:	Dr. E. Fretwurst
Vorsitzender des Promotionsausschusses	:	Prof. Dr. G. Huber
Dekan des Fachbereichs Physik	:	Prof. Dr. F.-W. Büßer

Kurzfassung

Es werden die Ergebnisse einer Suche nach Charginos mit Massen nahe der Neutralinomasse in e^+e^- Kollisionen bei Schwerpunktsenergien zwischen 189 und 209 GeV vorgestellt. Die Daten wurden aufgenommen mit dem OPAL Detektor am LEP Speicherring. Mit der Beschränkung auf Ereignisse mit einem hochenergetischen Photon, abgestrahlt im Anfangszustand, kann der Untergrund, bestehend aus Zwei-Photon Ereignissen, auf ein vernachlässigbares Niveau reduziert werden. Es wurde keine signifikante Diskrepanz zwischen Daten und Standard Modell Erwartung im gesamten analysierten Datensatz, entsprechend einer integrierten Luminosität von 570 pb^{-1}, beobachtet. Obere Grenzen auf den Chargino-Wirkungsquerschnitt wurden abgeleitet und untere Grenzen auf die Chargino-Masse für verschiedene Szenarien von Supersymmtriebrechung im Rahmen der minimalen supersymmetrischen Erweiterung des Standard Modells berechnet.

Eine Studie bezüglich der Suche nach fast masseentarteten Charginos und Neutralinos für das Linear Collider Projekt TESLA wird präsentiert. Von besonderem Interesse war hier der Einfluss des strahlinduziertem Untergrunds auf das Detektordesign und das Detektorverhalten.

Abstract

A search was performed for charginos with masses close to the mass of the lightest neutralino in e^+e^- collisions at centre-of-mass energies of 189–209 GeV recorded by the OPAL detector at LEP. Events were selected if they had an observed high-energy photon from initial state radiation, reducing the dominant background from two-photon scattering to a negligible level. No significant excess over Standard Model expectations has been observed in the analysed data set corresponding to an integrated luminosity of 570 pb^{-1}. Upper limits were derived on the chargino pair-production cross-section, and lower limits on the chargino mass were derived in the context of the Minimal Supersymmetric Extension of the Standard Model for the gravity and anomaly mediated supersymmetry breaking scenarios.

Studies concerning searches for nearly mass degenerate charginos and neutralinos at the next generation Linear Collider project, TESLA, are presented. A matter of particular interest was the influence of beam-induced background enviroment on the detector design and performance.

All my life I’ve been searching for something…
F. F.

And I kept on looking for a sign…
F.L.C.

Contents

Preface

Beyond the boundaries of various disciplines symmetries are a fascinating phenomenon and seem to be a central building block if not a driving force of Nature. The vision-driven human brains have learned to recognise symmetry as something special, and this has been exploited in human art and aesthetics but also in science.

Symmetry became to the maybe most crucial concept of modern physics when in 1905 Emmy Noether proved the following theorem which now bears her name [1]:

For every continuous symmetry of the laws of physics, there must exist a conservation law.
For every conservation law, there must exist a continuous symmetry.

The conservation laws of energy, momentum and angular momentum connected with the time translational symmetry, space translational symmetry, and the rotational symmetry, respectively, are probably the most popular examples for this theorem. Additional examples can be cited to show that the theorem also holds for discrete symmetries, that is to say, symmetries where the symmetry operations come in distinct steps. These symmetries can not be expressed in terms of infinitesimal symmetry operations.

Especially in the field of particle physics discrete symmetries are the more interesting since they show that the fundamental forces of Nature may have different levels of symmetry. Parity symmetry (P transformation), describing reflections in space, is perfectly respected in strong and electromagnetic interactions, but the weak force ignores this symmetry. Similar effects were found for the C symmetry, the symmetry of replacing all particles by their anti-particles (charge conjugation), and for the time reversal symmetry, T, describing reflections in time. However, quantum mechanics requires that the combined operations of CPT must be an exact symmetry of Nature, otherwise probability would not be conserved. So far all experimental results are consistent with this assumption.

Besides the differentiation between discrete and continuous symmetries, it is useful to distinguish between internal and space-time symmetries. In addition to the already mentioned temporal invariance, translational invariance and rotational invariance the Lorentz invariance is a fourth symmetry which belongs to space-time symmetries. All of them imply a symmetry between one spatio-temporal point and another. Internal symmetries are responsible for the fundamental forces of Nature. For example, the performance of an electric circuit is invariant to a global change of the phase of the electric field. In other words, internal symmetries are closely related with the degrees of freedom of fields. The underlying theory of particle physics is the so-called Standard Model, a theoretical framework based on quantum field theories, internal degrees of freedom are known as gauge degrees of freedom. These gauge symmetries give rise to the fields associated with the fundamental forces.

This excursion shows the importance of the question for the symmetries which a theory respects or violates. At least the question for the number of possible space-time symmetries of the Standard Model can be answered. In 1967 Coleman and Mandula [2] found that the Standard Model contains its full share of so-called bosonic space-time symmetries. These are symmetries for which the order of two symmetry transformations is indistinguishable. To put it in a more technical way, these are symmetries whose generators commute. The introduction of additional bosonic symmetries would lead to an illegal constraint on the allowed interactions of the Standard Model.

However, in 1975 Haag, Lopuszanski and Sohnius proved [3] that the introduction of any number of fermionic symmetry generators, anti-commuting generators, to the Standard Model would not spoil the theory, provided the generators satisfy a special algebra, a set of commutation and anti-commutation rules, which they called supersymmetry algebra.

Ever since that time supersymmetry became one of the most extensively considered extensions to the Standard Model. There are many reasons to believe that supersymmetry belongs to the basic properties of Nature. As it turned out it leads to a theory with improved predictive power and solves at the same time a series of conceptual problems of the Standard Model. Yet, an experimental proof is still missing. A supersymmetric theory should reveal itself by the introduction of new degrees of freedom, manifesting themselves as new particles. The discovery of such particles would be the first step towards a verification of supersymmetry. In a second step the properties of these particles would have to be examined and compared with the theoretical predictions.

If supersymmetry is realised in Nature and if the supersymmetric particles are light enough then they should also be produced in the collision of high energetic particles. This thesis deals with the search for two of these new particles, the so-called chargino and neutralino, in electron positron collisions. The first Chapter gives a compressed overview on the theoretical and phenomenological aspects of supersymmetry. Chapter 2 motivates the search scenario and explains the search strategy which was applied. This Chapter is followed by an introduction of the experimental apparatus used for this search. Chapter 4 describes in detail the search results and their interpretation. No evidence for supersymmetry was found in e^+e^- collisions up to a centre-of-mass energy of 209 GeV, a result which not necessarily rules out the existence of supersymmetry. The next generation of collider experiments will profit from a much larger discovery potential. Chapter 5 deals with the results of a study exploiting the possibility of precision measurements with special respect to charginos and neutralinos at the e^+e^- Linear Collider TESLA.

Chapter 1

Supersymmetry – Theory and Phenomenology

The Standard Model (SM) provided the cornerstone of elementary particle physics for more than 30 years. This Chapter will describe the step from the SM to a more fundamental theory, namely Supersymmetry (SUSY). After a short review on the SM and a description of its shortcomings and motivations for SM extensions, a more theoretical based introduction of SUSY follows. In a third part the phenomenological aspects of SUSY will be discussed.

1.1 The Standard Model and Beyond

1.1.1 The Status of the Standard Model

The SM is a theory of fermions and of gauge bosons mediating the $SU(3)_c \times SU(2)_L \times U(1)_Y$ colour and electroweak gauge interactions. It summarises the fundamental interactions of Nature, apart from gravity, in terms of relativistic gauge theories. Gauge invariant field theories are consistent theories only if all introduced particles are massless. Obviously, this is not the case in Nature. In the SM, the Higgs mechanism [4] is used to describe the observation of massive particles. A spontaneous breaking of the $SU(2)_L \times U(1)_Y$ weak isospin $\times$ weak hypercharge electroweak symmetry is forced by introducing one complex scalar field with non-zero vacuum expectation value. SM particles interacting with this field gain mass as a result of this interaction. The particle associated with the complex field is the Higgs boson. It is the only missing part in the SM puzzle. The complete list of the SM particles can be found in Table 1.1.

The overwhelming success of the SM, the almost perfect agreement between predictions and measurements was proven many times. So far none of the measurements shows a clear evidence for a SM failure. This is shown in Figure 1.1 which compares the results of the most important SM electroweak measurements with the SM predictions.

However, it is generally not believed that the SM is the ultimate theory. Although there are no questions which are wrongly answered within the SM concept so far, there are quite a few questions which are not answered by the SM at all. Why are there three generations of quarks and leptons? Do quarks and leptons consist of smaller constituents? Why are the absolute values

names	boson	fermion
W bosons	$W^{\pm}$	
Z boson	Z^0	
photon	γ	
gluon	g	
quarks (three families)		$(u_L\, d_L)$ u_R d_R
leptons (three families)		$(\nu\, e_L)$ e_R
Higgs	H	

Table 1.1: Particle content of the Standard Model (SM).

of the electron charge and the proton charge identical? Are the three interactions described by the SM three different appearances of a single one? The list of questions can be continued.

One of the strongest arguments that the SM is rather an effective theory of a more general one is related with the Planck scale ($M_{\mathrm{P}} \sim 10^{19}\,\mathrm{GeV}$). At this scale the gravitational force is not negligible any more and the SM has to be modified in order to incorporate the gravitational force. Apparently, the SM can be viewed as a low energy approximation of a more general theory. If something like the primary theory [5] exist, a theory which should describe Nature on all scales, the way to this theory will lead over a series of effective theories. Anyhow, going from one effective theory to the next one might open a window to the Planck scale which helps to complete our picture of Nature. The best way to pin down the demands on an consistent extension or replacement of the SM is to start with the conceptual problems of the SM.

1.1.2 The Conceptual Problems of the Standard Model

The Origin of the Higgs Mechanism

The Higgs mechanism of the SM can be reduced to the scalar Higgs field, Φ, and an appropriate scalar potential, $V(\Phi)$

$$V(\Phi) = m^2\Phi\Phi^\dagger + \lambda(\Phi\Phi^\dagger)^2, \text{ with } m^2 < 0,\ \lambda > 0. \tag{1.1}$$

In other words, the two main ingredients are the existence of the scalar field and a negative square of the mass parameter m. Technically the Higgs mechanism solves the problem of the origin of mass, but in the SM the condition of a negative m^2 has to be imposed by hand. It does not emerge from the theory itself. The origin of the Higgs mechanism cannot be explained within the SM framework.

The Gauge Unification

The success of the unification of the electric and magnetic force and later on the unification of electromagnetic and weak interaction was very promising. It is the motivation to assume that all fundamental interactions unify at a high energy scale (GUT scale).

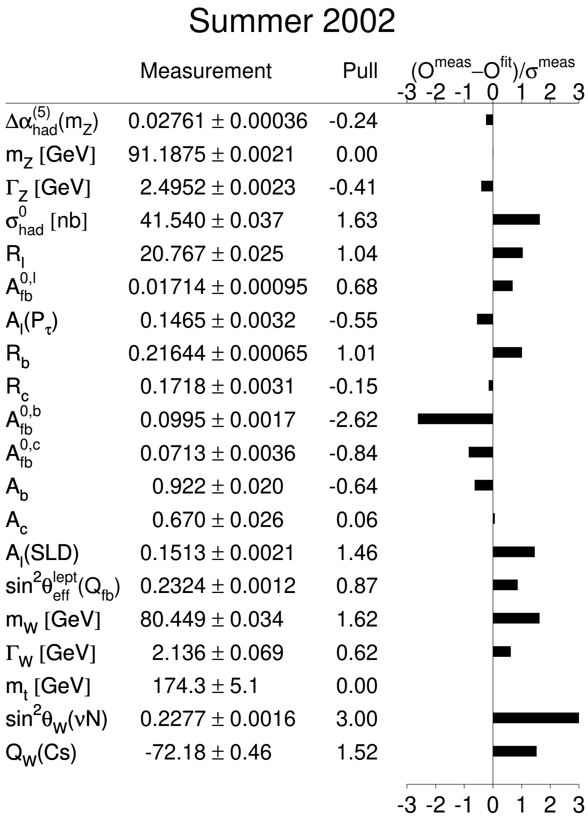

Figure 1.1: Comparison between SM electroweak measurements and the SM predictions for the global best fit values.

Using the renormalisation group (RG) formalism the coupling constants can be extrapolated. Assuming only the SM matter content at all energies the three couplings of the $SU(3)$, $SU(2)$ and $U(1)$ interactions fail to unify as indicated in Figure 1.2. The nice concept of unification seems unlikely and is impossible to establish within the SM.

The Hierarchy Problem

The SM as a quantum theory suffers from the so-called hierarchy problem [8]. The reason for two, very distinct energy scales, the electroweak scale and the Planck scale is not apparent. That is to say, the SM can neither explain the separation of the electroweak and the Planck scale, not to mention the very different sizes of the energy scales, nor how the separation can be maintained in a mathematically consistent way.

The Naturalness Problem

The naturalness problem is often referred to as the hierarchy problem. We know from experiments that the Higgs vacuum expectation value is given by $\langle\Phi\rangle = 174$ GeV. This value requires

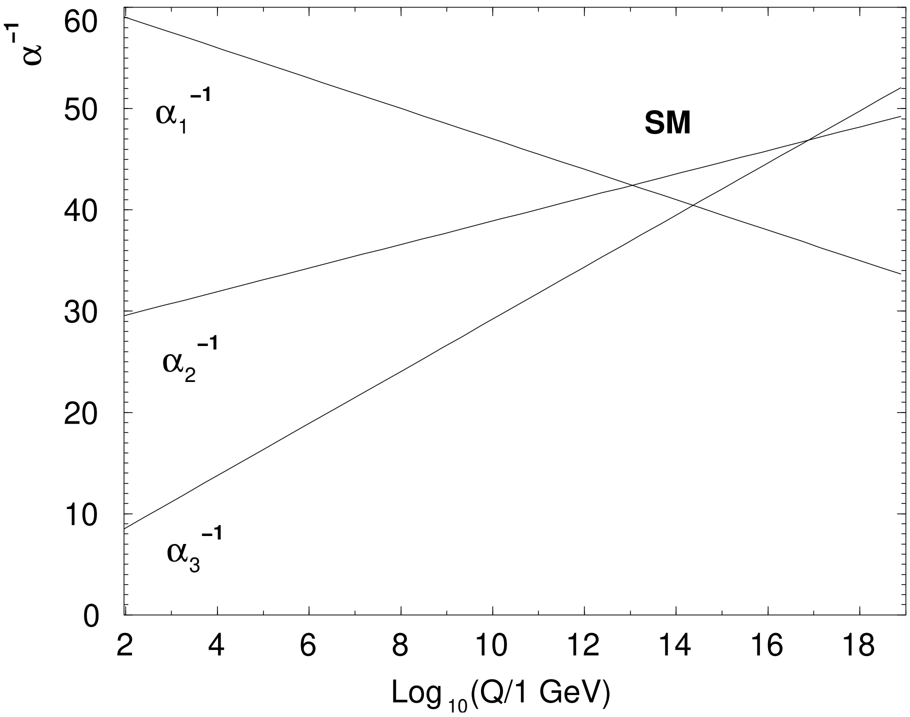

Figure 1.2: RG evolution of the inverse gauge couplings $\alpha_a^{-1}(Q)$ of the $U(1)$, $SU(2)$, $SU(3)$ gauge groups in the SM [6, 7].

that m^2 is roughly of order $O(-(100\,\mathrm{GeV})^2)$. But m^2 does not represent a robust value since it receives quantum corrections via virtual effects of every particle coupling directly or indirectly to the Higgs field. One-loop quantum corrections to m^2 from fermions and bosons as depicted in Figure 1.3 lead to the following corrections

$$\text{fermion corrections: } \Delta m^2 \sim -\sum_f C_f \frac{y_f^2}{16\pi^2}\Lambda_{\mathrm{UV}}^2, \tag{1.2}$$

$$\text{boson corrections: } \Delta m^2 \sim C_W \frac{g^2}{16\pi^2}\Lambda_{\mathrm{UV}}^2, \tag{1.3}$$

where C_i are numerical coefficients whose values are immaterial here , y_f and g are the Yukawa and gauge couplings and Λ_{UV} is the ultraviolet cut-off. Note the negative sign for the fermion contributions. The problem now is that if Λ_{UV} is of order M_{P} then the quantum corrections are some 30 orders of magnitude larger than the aimed-for value of m^2. It is interesting to note that this problem applies directly only to corrections to the Higgs mass. Corrections to fermion or gauge boson masses do not depend on Λ_{UV}^2. However, since all SM particles gain their mass through $\langle\Phi\rangle$ the entire SM particle mass spectrum is sensitive to Λ_{UV}^2. The only way out seems to require a rather unnatural adjustment of the quadratic divergences and thus retain the m^2 value. This is called the naturalness problem [9]. The SM offers no answer why electroweak symmetry breaking occurs at the electroweak scale and not close to the Planck scale. The solution to this problem and any understanding of the specific choice of the electroweak scale must lie outside the SM.

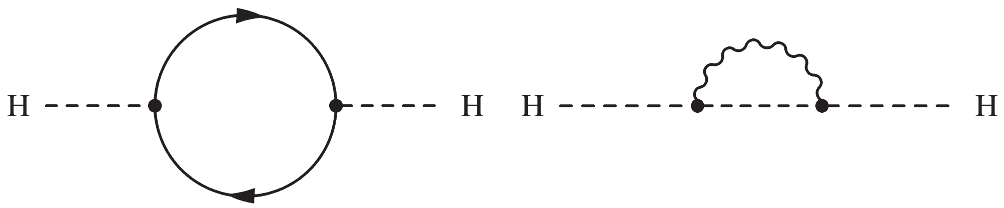

Figure 1.3: Quantum corrections to the Higgs (mass)^2. Left: fermion contributions, right: boson contributions.

1.1.3 Theoretical Ways Out

There exist a couple of theoretical frameworks which might solve the problems mentioned above. A few of them should be briefly described before the concept of SUSY will be introduced.

Strong Interactions

Assuming that the Higgs is a composite of fermions rather than a fundamental particle the naturalness problem can be solved by removing elementary scalar bosons from the particle spectrum [10]. These kind of models, technicolor models are representatives, copy the mechanism of QCD, where mesons and baryons are the degrees of freedom at low energies while quarks and gluons are the ones at higher energies. The models predict not only additional matter, but also strong dynamics at energies close to current experimental energies [9]. However, a construction of such a model consistent with experimental results involving electroweak gauge bosons and flavour changing neutral currents (FCNC) is subtle.

Extra Spatial Dimensions

The fine-tuning problem can be avoided if the Planck scale would be brought down close to the electroweak scale. This could be reached when the well known four space-time dimensions would reside in a higher dimensional extension of space time [11]. In order to be consistent with gravity measurements, extra dimensions must be compactified at radii $R \lesssim 1$ mm. The four-dimensional Planck scale and the Planck scale in $(4+n)$ dimension is related via R

$$M_{\mathrm{P}}^{4d} = \left(M_{\mathrm{P}}^{(4+n)d}\right)^{\frac{n+2}{2}} R^{\frac{n}{2}} \tag{1.4}$$

This relation also explains the weakness of gravity in terms of extra large dimensions rather than in terms of a large Planck mass.

Conformal Theories

It might be possible to build theories which are scale invariant above the electroweak scale [12]. Since in these conformal theories no other scales occur the hierarchy problem is apparently solved. These kind of approaches suffer from the fact that so far no consistent example could be constructed.

1.2 Supersymmetry Introduction

Following the historical development this introduction starts with a description of the basic idea of supersymmetry before its details and implications are discussed. For more extensive and elaborate reviews on this topic see for example [6, 13–16].

1.2.1 Basics

The concept of supersymmetry was conceived in 1973 by Wess and Zumino [17] and earlier in a nonlinear realisation by Volkov and Akulov [18]. A theory is supersymmetric if its equations do not change if fermions are replaced by bosons and vice versa. Extension to the SM can be found following this property without touching established results[1]. The replacement of fermions or bosons by their counterparts mathematically happens through a SUSY generator Q, an anticommuting spinor, that allows transformation like

$$Q|\text{fermion}\rangle = |\text{boson}\rangle; \qquad Q|\text{boson}\rangle = |\text{fermion}\rangle. \tag{1.5}$$

The generator Q is a complex object, that is to say that besides Q, its hermitian conjugate, $Q^\dagger$, is also a symmetry operator. Together with the momentum generators, P^μ, they form a minimal non-trivial supersymmetry algebra with the following transformations

$$\begin{aligned} \{Q, Q^\dagger\} &= P^\mu, \\ \{Q, Q\} = \{Q^\dagger, Q^\dagger\} &= 0, \\ [P^\mu, Q] = [P^\mu, Q^\dagger] &= 0, \end{aligned} \tag{1.6}$$

where the spinor indices of Q and $Q^\dagger$ are suppressed to simplify matters. Within a supersymmetric theory the particles have to be arranged in supermultiplets, irreducible representations of the supersymmetry algebra. Since Q commutes with the $(\text{mass})^2$ operator, $-P^2$, and all operators of space-time transformations and rotations as well as all generators of gauge transformations, the particles within one supermultiplet have to have equal masses and the same electric charge, weak isospin and colour degrees of freedom. Supersymmetric theories allow more than one pair of supersymmetry generators, $(Q, Q^\dagger)$. The present discussion will concentrate on the so-called $N = 1$ supersymmetry model, where N indicates the number of distinct copies of $(Q, Q^\dagger)$. In a $N = 1$ supersymmetry model two different kinds of supermultiplets can be distinguished:

[1] As a matter of fact at the time supersymmetry was introduced technical problems were solved rather quickly. It took longer to discover the benefit of supersymmetry and supersymmetry was often regarded as 'solution in search of a problem' [5].

- Matter or chiral supermultiplets consist of a single Weyl fermion[2] and two real scalars.
- Gauge or vector supermultiplets contain one spin-1 vector boson and a spin-1/2 Weyl fermion.

All particles of a supersymmetric model, including those already known from the SM, have to be a member of one of these supermultiplets.

1.2.2 Ordering the Supersymmetric Particle Content

The ordering of the supersymmetric particle content is based on the prescription that the number of fermionic degrees of freedom has to be identical to the number of bosonic degrees of freedom. In a first step all quarks and leptons fall into chiral supermultiplets. Only those can contain fermions whose left-handed parts transform differently under the gauge group then their right-handed parts. The corresponding spin-0 partners (see above) are the so-called squarks and sleptons, where 's' denotes 'scalar'. The left- and right-handed fermions get separate partners called left- and right-handed squarks and sleptons[3].

The Higgs boson as a scalar resides in a chiral supermultiplet. However, it turns out that the existence of one Higgs chiral supermultiplet is not enough. An anomaly free supersymmetric theory requires a vanishing hypercharge trace

$$\mathrm{Tr}[Y^3] = \mathrm{Tr}[T_3^2 Y] = 0, \tag{1.7}$$

where T_3 and Y are the third component of weak isospin and the weak hypercharge, respectively, in a normalisation where the ordinary electric charge is $Q_{\mathrm{em}} = T_3 + Y$. A fermionic partner of a Higgs chiral supermultiplet with hypercharge either $Y = \frac{1}{2}$ or $Y = -\frac{1}{2}$ makes a non-vanishing contribution to the trace. Having two Higgs supermultiplets, each with different sign of the hypercharge, let the contributions cancel. Two complex Higgs doublets are also required in order to generate both up- and down-type masses. In the SM one Higgs doublet is sufficient to give mass to the up- and down-type quarks by simply using the complex conjugate of the Higgs doublet. However, terms involving the charge conjugates of superfields are not allowed in supersymmetric models. In the following the two Higgs doublets are called H_u and H_d. The weak isospin components of H_u have electric charge $1, 0$. According to this the weak isospin components of H_d have electric charge $-1, 0$. The spin-1/2 superpartners of the Higgs scalars are called higgsinos.

Finally the SM gauge bosons fall into vector supermultiplets. Similar to the Higgs sector the superpartners are called gauginos which is the collective term for the gluinos, winos, zinos and photinos.

The particles of the introduced matter and vector supermultiplets are summarised in Table 1.2. They are the content of the Minimal Supersymmetric Standard Model (MSSM), the simplest potentially realistic supersymmetric field theory [19, 20].

[2] Weyl particles are fermions described by only a left-handed spinor.

[3] The handedness does not refer to the helicity of the squarks and sleptons but to the helicity of their superpartners.

names	boson	fermion
vector supermultiplets		
W bosons (wino)	$W^{\pm}$	$\tilde{W}^{\pm}$
Z boson (zino)	Z^0	$\tilde{Z}^0$
photon (photino)	γ	$\tilde{\gamma}$
gluon (gluino)	g	$\tilde{g}$
chiral supermultiplets		
quarks (squarks)	$(\tilde{u}_L\ \tilde{d}_L)$	$(u_L\ d_L)$
(three families)	$\tilde{u}_R$	u_R
	$\tilde{d}_R$	d_R
leptons (sleptons)	$(\tilde{\nu}\ \tilde{e}_L)$	$(\nu\ e_L)$
(three families)	$\tilde{e}_R$	e_R
Higgs (higgsinos)	(H_u^+, H_u^0)	$(\tilde{H}_u^+, \tilde{H}_u^0)$
	(H_d^0, H_d^-)	$(\tilde{H}_d^0, \tilde{H}_d^-)$

Table 1.2: Vector and chiral supermultiplets in the Minimal Supersymmetric Standard Model (MSSM).

1.2.3 Local Supersymmetry

So far only global supersymmetry, in which SUSY transformations are constant throughout space, was considered. Adding space-time coordinates to Equation (1.6) and thus promoting supersymmetry to a local symmetry shows that invariance under local supersymmetry implies invariance under local coordinate change. This is the same principle underlying the theory of general relativity. Local supersymmetry therefore almost naturally includes gravity. Local symmetries must contain a further fermionic gauge field. In case of supersymmetry this is identified as the field of a gravitino (spin-3/2) the superpartner of a spin-2 particle, the graviton. That is to say that the particle content of theories obeying local supersymmetry is extended by the graviton and the gravitino. Theories with local supersymmetry belong to the class of super-gravity theories (SUGRA) [21].

1.2.4 Supersymmetry and the SM Problems

The introduction of supersymmetric partner particles to all SM particles is not only a theoretical gimmick. Many of the conceptual problems of the SM do not arise in supersymmetric models and they offer a series of explanations for observed phenomena not covered within the SM:

- Within supersymmetric theories the unification of gauge couplings is possible. Based on current measurements for α_s and $\sin^2\theta_W$ it emerges almost naturally from the RG. As indicated in Figure 1.4, within the MSSM the agreement of the gauge couplings at high energies is impressive compared to the SM predictions.

- Assuming that all superpartners are unstable particles, decaying into lighter superpartners, except for the lightest supersymmetric particle (LSP), the LSP, if stable, is a good dark matter candidate [22].

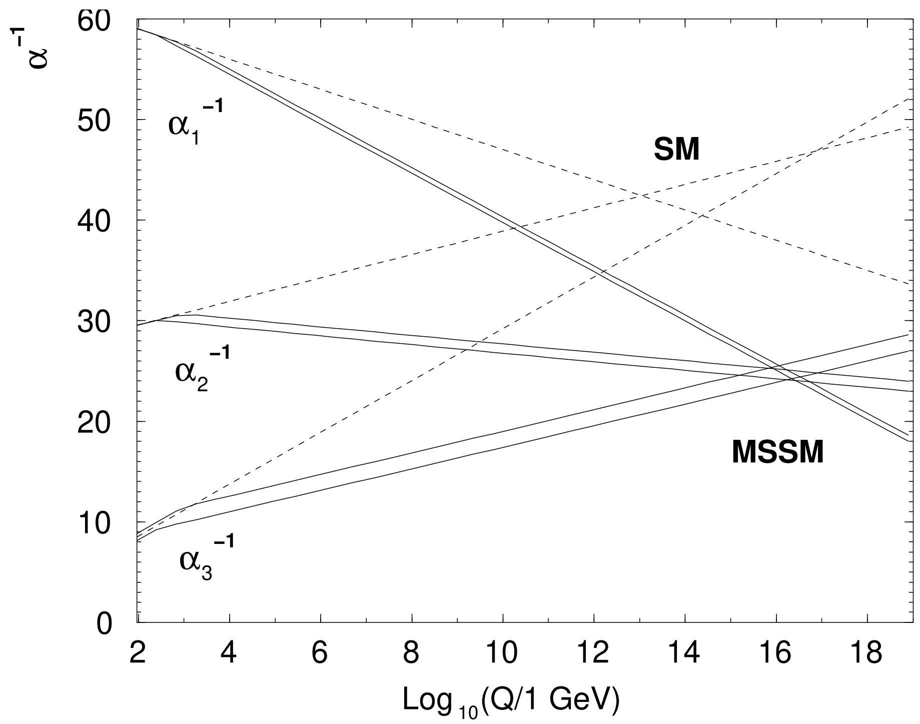

Figure 1.4: RG evolution of the inverse gauge couplings $\alpha_a^{-1}(Q)$ of the $U(1)$, $SU(2)$, $SU(3)$ gauge groups in the SM (dashed line) and the MSSM [6, 7]. In the MSSM case, $\alpha_3(M_Z)$ is varied between 0.113 and 0.123, and the sparticle mass thresholds between 250 GeV and 1 TeV. Two-loop effects are included.

- Supersymmetric models like the MSSM have the appealing feature that they are able to explain the mechanism of electroweak symmetry breaking [13].

- Supersymmetry, as a symmetry throughout space-time, necessarily has a connection to the theoretical description of gravity. Although this connection is not yet fully understood, the fact alone is very encouraging [5].

- SUSY models also solve the problem of quadratic divergencies in Higgs mass calculations and thus remove the naturalness problem. This is due to the relative minus sign in the fermion and boson loop contributions (Equation (1.2) and Equation (1.3)). Since in SUSY models each fermion is accompanied by two complex scalars the Λ_{UV}^2 contribution neatly cancel. Moreover, SUSY assures that this cancellations occur at all orders in perturbation theory, a consequence of the non-renormalisation theorems [23] of supersymmetry.

1.2.5 Supersymmetry Breaking

The exact cancellation of quadratic divergencies in the Higgs mass calculations is linked to the condition that SM particles and their partners have exactly the same mass. Obviously, this is not the case. Otherwise they would have been already discovered. Even if direct searches would have missed them, particles like the selectron should have revealed themselves indirectly. If there were an unbroken supersymmetry, there would be a super-hydrogen atom with a selectron bound to a proton. The chemistry of multi-selectron atoms, with bosons rather than fermions bound to the nucleus, would be very different. Also additional weak interactions, with $\tilde{\mathrm{W}}$ exchanged, are not observed.

To summarise, adherence to the concept of supersymmetry requires that supersymmetry is a broken symmetry in the vacuum state chosen by Nature. Nevertheless, it is still possible to avoid quadratically divergent radiative corrections to the Higgs mass if only 'soft' supersymmetry breaking is considered. In this case the effective Lagrangian of the MSSM can be written as

$$\mathcal{L} = \mathcal{L}_{\mathsf{SUSY}} + \mathcal{L}_{\mathrm{soft}}, \tag{1.8}$$

where $\mathcal{L}_{\mathsf{SUSY}}$ preserves supersymmetry invariance, and $\mathcal{L}_{\mathrm{soft}}$ contains only mass terms and couplings with positive mass dimensions [6]. The contributions to $\mathcal{L}_{\mathrm{soft}}$ are restricted. Assuming that m_{soft} describes the largest mass scale in $\mathcal{L}_{\mathrm{soft}}$, the non-supersymmetric corrections to the Higgs mass must vanish in the limit $\mathcal{L}_{\mathrm{soft}} \to 0$. With a dimensional analysis it can be demonstrated that these corrections can only show a logarithmic behaviour

$$\Delta m^2 \sim m_{\mathrm{soft}}^2 \ln\left(\frac{\Lambda_{\mathrm{UV}}}{m_{\mathrm{soft}}}\right) \tag{1.9}$$

A couple of special SUSY breaking models which exactly add only soft breaking terms to the effective Lagrangian will be introduced in the Section on phenomenological aspects of supersymmetry. The following Section addresses the origin ofSUSY breaking.

1.2.6 The Origin of Supersymmetry Breaking

Supersymmetry breaking explains why all the supersymmetric partner particles were not discovered so far. While all SM particles are massless in the absence of electroweak symmetry breaking all partner particles can have a Lagrangian mass term even in the absence of electroweak symmetry breaking [6].

Though it is expected that supersymmetry is spontaneously broken, it is often convenient to parametrise the SUSY breaking mechanism by introducing extra terms to the effective Lagrangian and thus break supersymmetry explicitly. These extra terms should be 'soft'. Dimensionless supersymmetry-breaking couplings are not allowed. Using the following notations

$$\begin{aligned}
Q &= (u\,d),\ (c\,s),\ (t\,b)\\
\bar{u} &= \bar{u},\ \bar{c},\ \bar{t}\\
L &= (\nu_e\,e),\ (\nu_\mu \mu),\ (\nu_\tau \tau)\\
\bar{e} &= \bar{e},\ \bar{\mu},\ \bar{\tau},
\end{aligned} \tag{1.10}$$

the MSSM Lagrangian can be written as

$$\begin{aligned}
\mathcal{L}_{\mathrm{soft}} = &-\frac{1}{2}(M_3\tilde{g}\tilde{g} + M_2\tilde{\mathrm{W}}\tilde{\mathrm{W}} + M_1\tilde{\mathrm{B}}\tilde{\mathrm{B}}) + c.c.\\
&-(\tilde{\bar{u}}\mathbf{a}_u\tilde{Q}H_u - \tilde{\bar{d}}\mathbf{a}_d\tilde{Q}H_d - \tilde{\bar{e}}\mathbf{a}_e\tilde{L}H_d) + c.c.\\
&-\tilde{Q}^\dagger\mathbf{m}_Q^2\tilde{Q} - \tilde{L}^\dagger\mathbf{m}_L^2\tilde{L} - \tilde{\bar{u}}\mathbf{m}_{\bar{u}}^2\tilde{\bar{u}}^\dagger - \tilde{\bar{d}}\mathbf{m}_{\bar{d}}^2\tilde{\bar{d}}^\dagger - \tilde{\bar{e}}\mathbf{m}_{\bar{e}}^2\tilde{\bar{e}}^\dagger\\
&-m_{H_u}^2 H_u^\star H_u - m_{H_d}^2 H_d^\star H_d - (bH_uH_d + c.c.),
\end{aligned} \tag{1.11}$$

where M_1, M_2 and M_3 are the bino, wino and gluino mass terms, $\mathbf{a}_u$, $\mathbf{a}_d$ and $\mathbf{a}_e$ are 3×3 matrices in family space representing (scalar)^3 couplings, $\mathbf{m}^2_Q$, $\mathbf{m}^2_L$, $\mathbf{m}^2_{\bar{u}}$, $\mathbf{m}^2_{\bar{d}}$ and $\mathbf{m}^2_{\bar{e}}$ are hermitian 3×3 matrices describing squark and slepton mass terms while the last line contains the supersymmetry-breaking contributions to the Higgs potential, $m^2_{H_u}$, $m^2_{H_d}$ and b. As demonstrated in [24] the MSSM $\mathcal{L}_{\text{soft}}$ adds 105 new fundamental parameters, including masses, phases and mixing angles, to the theory. This is the result of the general parametrisation and is not an indication of arbitrariness. It is rather the manifestation of an ignorance about the supersymmetry breaking mechanism. However, experimental results, especially on the field of flavour mixing and CP violation restrict the choice of soft terms.

The parametrisation of supersymmetry breaking does not explain the origin of supersymmetry breaking. An explanation requires a study of spontaneous supersymmetry breaking. If supersymmetry is spontaneously broken the vacuum state, $|0\rangle$, is not invariant under supersymmetry transformations, $Q|0\rangle \neq 0$, the groundstate of the SUSY potential is positive

$$\langle 0|\mathcal{H}|0\rangle > 0, \tag{1.12}$$

where $\mathcal{H}$ is the Hamiltonian, which is related to the supersymmetry generators using the supersymmetry algebra (Equation (1.6))

$$\mathcal{H} = P^0 = \frac{1}{4}\left(Q_1Q_1^\dagger + Q_1^\dagger Q_1 + Q_2Q_2^\dagger + Q_2^\dagger Q_2\right). \tag{1.13}$$

Equation (1.12) can then be rewritten as:

$$\langle 0|\mathcal{H}|0\rangle = \frac{1}{4}\left(||Q_1|0\rangle||^2 + ||Q_1^\dagger|0\rangle||^2 + ||Q_2|0\rangle||^2 + ||Q_2^\dagger|0\rangle||^2\right) > 0. \tag{1.14}$$

This can be extended to the scalar potential V:

$$\langle 0|\mathcal{H}|0\rangle = \langle 0|V|0\rangle > 0, \tag{1.15}$$

which, expressed in terms of auxiliary fields, F_i and D^a [6], is:

$$V = \sum_i |F^i|^2 + \frac{1}{2}\sum_a (D^a)^2 \quad \text{with } F_i^\star \equiv \frac{\partial W}{\partial \phi^i},\ D^a \equiv g_a \phi_i^\star (T^a)^i_j \phi^j, \tag{1.16}$$

where the sums run over all matter fields i and the $SU(3)$, $SU(2)$ and $U(1)$ gauge group factors a, W is the superpotential and T^a is the group representation matrix for the matter fields ϕ^i.

Obviously Equation (1.15) can be fulfilled, and supersymmetry is spontaneously broken, if F_i and/or D^a do/does not vanish. According to this, supersymmetry breaking mechanisms are classified as F-term and D-term breaking. Without further justification, both ways require an extension of the MSSM. Both F-term and D-term breaking need to introduce additional matter fields. But introducing an additional field which carries SM quantum numbers with non-vanishing vacuum expectation value as in electroweak symmetry breaking is not possible without breaking the $SU(3)$ or $U(1)$ gauge invariance [6]. Generally, it is believed that supersymmetry breaking occurs in a 'hidden sector' of particles which have no or only small direct couplings to the 'observable sector' with all MSSM particles. The MSSM soft terms arise indirectly or radiatively as a result of some interaction between the hidden and the observable sector. Depending on the choice of this interaction and phenomenological motivated constraints on the huge SUSY parameter space, a series of possible scenarios were proposed. Their introduction will be part of the next Section.

1.3 Supersymmetry Phenomenology

This short review on supersymmetry shall be completed with a description of some phenomenological aspects of supersymmetry, concentrating on the experimentally most important ones.

1.3.1 Particles, Mass and Gauge Eigenstates

The superpartners listed in Table 1.2 are not necessarily the mass eigenstates of the theory. This is simply due to the fact that after electroweak symmetry breaking and after including the supersymmetry breaking effects, the electroweak gauginos and the higgsinos, and the various squarks and sleptons can mix, provided they carry the same quantum numbers. The next paragraphs will describe the transitions from weak to mass eigenstates for various particles.

Goldstinos and Gravitinos

The effect of symmetry breaking always comes along with the production of a massless Goldstone boson. In an analogous manner supersymmetry breaking produces a massless fermion, the goldstino. In local supersymmetry models the gravitino absorbs the goldstino and gains mass. This mechanism is called super-Higgs mechanism in analogy to the Higgs mechanism.

Squarks and Sleptons

In the squark and slepton sector any scalars with the same electric charge and colour quantum numbers can mix. The mass eigenstates are then obtained by diagonalising three 6×6 $(\text{mass})^2$ matrices for up-type squarks, down-type squarks and charged sleptons, respectively. Mass eigenstates of the neutral sleptons can be calculated by diagonalising the 3×3 $(\text{mass})^2$ matrix. Without further justification, the flavour-blind soft mass terms do not allow large mixing angles and the mass eigenstates more or less correspond to the weak eigenstates, at least in the first two families of squarks and sleptons. The mixing angles for the third family, $\theta_{\tilde{t}}$, $\theta_{\tilde{b}}$, $\theta_{\tilde{\tau}}$, can be sizeable due to the large Yukawa and soft couplings. The mass eigenstates are then expressed via the mixing angles as follows:

$$\begin{pmatrix}\tilde{t}_1\\ \tilde{t}_2\end{pmatrix} = \begin{pmatrix}\cos\theta_{\tilde{t}} & \sin\theta_{\tilde{t}}\\ -\sin\theta_{\tilde{t}} & \cos\theta_{\tilde{t}}\end{pmatrix}\begin{pmatrix}\tilde{t}_L\\ \tilde{t}_R\end{pmatrix} \tag{1.17}$$

$$\begin{pmatrix}\tilde{b}_1\\ \tilde{b}_2\end{pmatrix} = \begin{pmatrix}\cos\theta_{\tilde{b}} & \sin\theta_{\tilde{b}}\\ -\sin\theta_{\tilde{b}} & \cos\theta_{\tilde{b}}\end{pmatrix}\begin{pmatrix}\tilde{b}_L\\ \tilde{b}_R\end{pmatrix} \tag{1.18}$$

$$\begin{pmatrix}\tilde{\tau}_1\\ \tilde{\tau}_2\end{pmatrix} = \begin{pmatrix}\cos\theta_{\tilde{\tau}} & \sin\theta_{\tilde{\tau}}\\ -\sin\theta_{\tilde{\tau}} & \cos\theta_{\tilde{\tau}}\end{pmatrix}\begin{pmatrix}\tilde{\tau}_L\\ \tilde{\tau}_R\end{pmatrix} \tag{1.19}$$

The mass eigenstates are labeled in ascending order according to the mass.

The Higgs Sector in Supersymmetry

Compared to the SM, the Higgs sector of the MSSM is slightly more complicated. The scalar potential depends on two complex Higgs doublets, $H_u = (H_u^+, H_u^0)$ and $H_d = (H_d^0, H_d^-)$:

$$\begin{aligned} V =&(|\mu|^2 + m_{H_u}^2)|H_u^0|^2 + (|\mu|^2 + m_{H_d}^2)|H_d^0|^2 - (bH_u^0 H_d^0 + c.c.) \\ &+ \frac{1}{8}(g^2 + g'^2)(|H_u^0|^2 - |H_d^0|^2)^2, \end{aligned} \tag{1.20}$$

where $SU(2)$ gauge transformations were used to rotate away possible vacuum expectation values for one of the weak isospin components of the scalar field ($H_u^+ = H_d^- = 0$), μ is the Higgs mixing parameter, describing the mixing of the two Higgs doublets, and g and g' are the $U(1)$ and $SU(2)$ gauge couplings.

The neutral components of the Higgs scalars still can get vacuum expectation values, $\langle H_u^0 \rangle = v_u$ and $\langle H_d^0 \rangle = v_d$, which can be connected to the Z^0 mass, M_Z:

$$v_u^2 + v_d^2 = v^2 = \frac{2M_\mathrm{Z}^2}{g^2 + g'^2} \approx (174\ \mathrm{GeV})^2. \tag{1.21}$$

The ratio of the two vacuum expectation values is normally written as:

$$\tan\beta = \frac{v_u}{v_d}. \tag{1.22}$$

The two complex $SU(2)$ doublets have eight scalar degrees of freedom. After electroweak symmetry breaking three of them are the would-be Goldstone bosons, G^0 and $G^\pm$, which become the longitudinal modes of the Z^0 and $\mathrm{W}^\pm$ massive vector bosons. The remaining five degrees of freedom manifest themselves in five Higgs scalar mass eigenstates, one CP-odd neutral scalar, A^0, two electrically charged scalars, $H^\pm$, and two CP-even neutral scalars h^0 and H^0. Besides β, a second mixing angle, α, is defined describing the rotation between the weak and mass eigenstates:

$$\begin{pmatrix} G^0 \\ A^0 \end{pmatrix} = \sqrt{2} \begin{pmatrix} \sin\beta & -\cos\beta \\ \cos\beta & \sin\beta \end{pmatrix} \begin{pmatrix} \Im(H_u^0) \\ \Im(H_d^0) \end{pmatrix} \tag{1.23}$$

$$\begin{pmatrix} G^+ \\ H^+ \end{pmatrix} = \begin{pmatrix} \sin\beta & -\cos\beta \\ \cos\beta & \sin\beta \end{pmatrix} \begin{pmatrix} H_u^+ \\ H_d^{-\star} \end{pmatrix} \tag{1.24}$$

$$\begin{pmatrix} h^0 \\ H^0 \end{pmatrix} = \sqrt{2} \begin{pmatrix} \cos\alpha & -\sin\alpha \\ \sin\alpha & \cos\alpha \end{pmatrix} \begin{pmatrix} \Re(H_u^0) - v_u \\ \Re(H_d^0) - v_d \end{pmatrix} \tag{1.25}$$

Taking quantum corrections into account and assuming that none of the MSSM particles has a mass exceeding 1 TeV the mass of h^0 is limited (in contrast to all other Higgs particle masses) [25]:

$$m_{h^0} \lesssim 134\ \mathrm{GeV}. \tag{1.26}$$

Gauginos and Higgsinos

Due to the effects of electroweak symmetry breaking the higgsinos and the electroweak gauginos mix. The charginos ($\tilde{\chi}^{\pm}_{i=1,2}$) are the mass eigenstates formed by the mixing of the fields of the charged gauginos and higgsinos. The neutralinos ($\tilde{\chi}^{0}_{j=1,\dots,4}$) are correspondingly formed by the mixing of the neutral gauginos and higgsinos.

In the gauge-eigenstate basis $\psi^0 = (\tilde{\mathrm{B}}^0, \tilde{\mathrm{W}}^0, \tilde{H}^0_d, \tilde{H}^0_u)$ the neutralino mass matrix, $\tilde{\mathbf{N}}$, can be written as:

$$\tilde{\mathbf{N}} = \begin{pmatrix} M_1 & 0 & -\cos\beta\sin\theta_W M_Z & \sin\beta\sin\theta_W M_Z \\ 0 & M_2 & \cos\beta\cos\theta_W M_Z & -\sin\beta\cos\theta_W M_Z \\ -\cos\beta\sin\theta_W M_Z & \cos\beta\cos\theta_W M_Z & 0 & -\mu \\ \sin\beta\sin\theta_W M_Z & -\sin\beta\cos\theta_W M_Z & -\mu & 0 \end{pmatrix}, \quad (1.27)$$

where θ_W is the Weinberg angle. The neutralino masses, $M_{\tilde{\chi}^0_{i=1\dots4}}$, are the eigenvalues of $\tilde{\mathbf{N}}$ and are the solution of the characteristic equation [26]

$$M^8_{\tilde{\chi}^0_i} - aM^6_{\tilde{\chi}^0_i} + bM^4_{\tilde{\chi}^0_i} - cM^2_{\tilde{\chi}^0_i} + d = 0 \quad (i = 1\dots4), \quad (1.28)$$

with a, b, c and d given by the fundamental parameters of the neutralino system: M_1, M_2, μ and $\tan\beta$ which represent the soft parameters (see Equation (1.11)) at the electroweak scale after RG evolution.

The chargino system can be described in a similar way. The chargino mass matrix, $\tilde{\mathbf{C}}$, is given as

$$\tilde{\mathbf{C}} = \begin{pmatrix} M_2 & \sqrt{2}\sin\beta M_{\mathrm{W}} \\ \sqrt{2}\cos\beta M_{\mathrm{W}} & \mu \end{pmatrix}, \quad (1.29)$$

where M_W is the $\mathrm{W}^{\pm}$ mass. The chargino masses can be computed with the expression

$$M^2_{\tilde{\chi}^{\pm}_{1,2}} = \frac{1}{2}\Bigg[\left(|M_2|^2 + |\mu|^2 + 2M^2_{\mathrm{W}}\right) \mp \sqrt{\left(|M_2|^2 + |\mu|^2 + 2M^2_{\mathrm{W}}\right)^2 - 4\,|\mu M_2 - M_{\mathrm{W}}\sin 2\beta|^2}\Bigg]. \quad (1.30)$$

1.3.2 *R*-Parity and its Implications

The superpotential of the MSSM in its general form is not protected against adding terms which are gauge-invariant and analytic in the chiral superfields but violate either baryon number (B) or total lepton number (L). In order to avoid these terms in the MSSM a new symmetry, *R*-parity, is normally introduced. It is defined as

$$R_{\mathrm{P}} = (-1)^{3(B-L)+2s}, \quad (1.31)$$

where s is the spin of the particle. It is a multiplicatively conserved quantum number and distinguishes between particles and their supersymmetric partners. The consequences of *R*-parity conservation are

- The lightest supersymmetric particle (LSP, $R_P = -1$) has to be absolutely stable and terminates the decay chain of every supersymmetric particle. Cosmological constraints suggest that the LSP is almost certainly electrically and colour neutral and only weakly interacting [27], that is to say it behaves like a heavy stable neutrino.

- Each supersymmetric particle other than the LSP has to decay into a state containing an odd number of LSPs.

- Collider experiments allow only the pair production of supersymmetric particles.

In the following it is assumed that the MSSM conserves R-parity, an assumption which leaves room for an LSP dark matter candidate and can be additionally motivated by proton decay constraints[4].

1.3.3 MSSM Interactions

A complete description of all supersymmetric interactions and a computation of the Feynman rules of the MSSM can be found in [20,28,29]. Only one rule for the construction of supersymmetric interactions shall be mentioned here. In addition to all SM interactions, all interactions resulting from the replacement of an even number of SM particles by their supersymmetric partners are allowed within the MSSM.

1.3.4 Chargino Production and Decays

This thesis deals with a search for almost mass degenerate charginos and neutralinos in e^+e^- collisions, hence this particle sector of the MSSM shall be discussed in little more detail.

The production of charginos in e^+e^- collisions proceeds via pair production either in the s-channel or the t-channel. Both Feynman diagrams are depicted in Figure 1.5. The higgsino

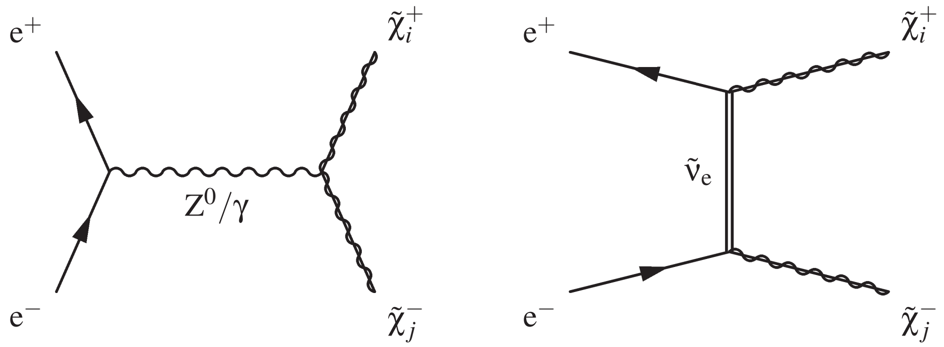

Figure 1.5: s- and t-channel production of charginos in e^+e^- collisions. As long as the sneutrino mass is large ($M_{\tilde{\nu}_e} > O(100\text{ GeV})$) the s-channel production is the dominant one. Both graphs interfere destructively. In this thesis only $i = j \equiv 1$ is considered.

component of the chargino does not couple to the sneutrino, exchanged in the t-channel, and

[4] However, a R_P violating MSSM does not suffer any internal inconsistency.

the s-channel is dominant as long as the higgsino component outweighs the gaugino component or the the sneutrino mass is large ($M_{\tilde{\nu}} > O(100\,\text{GeV})$). Both graphs interfere destructively. The effect on the cross-section is illustrated in Figure 1.6 for two extreme scenarios: the chargino is mainly a gaugino (the gaugino-like scenario) and the chargino is mainly a higgsino (the higgsino-like scenario). While the cross-sections in case of the gaugino-like scenario show the destructive interference of the t-channel, the cross-sections in case of the higgsino-like scenario do not depend on the sneutrino mass.

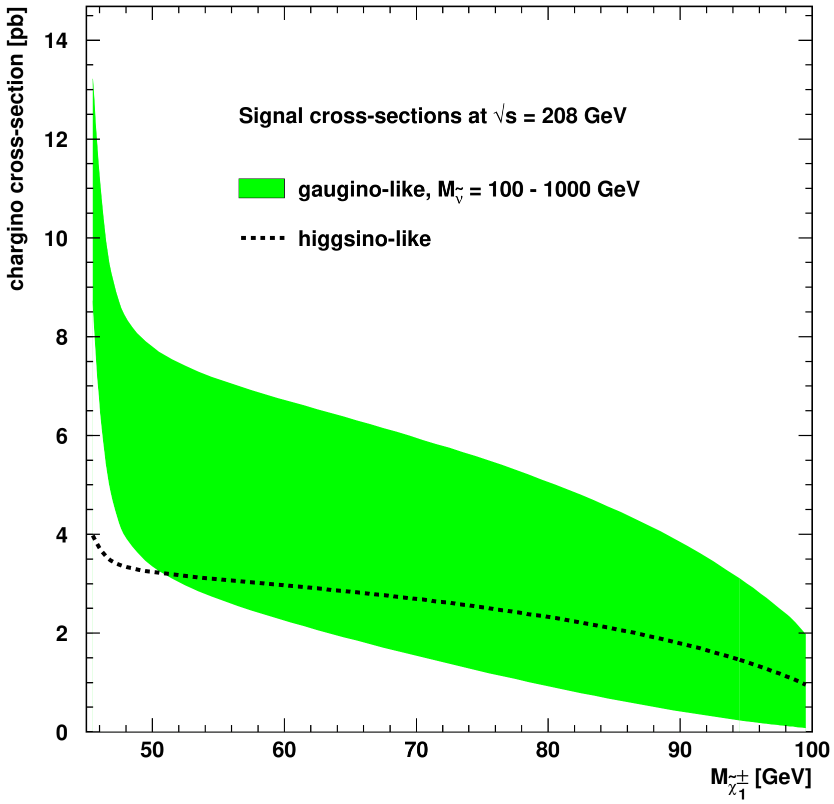

Figure 1.6: Chargino cross-sections as a function of the chargino mass at $\sqrt{s} = 208\,$GeV. The shaded band shows the cross-sections in case of a gaugino-like chargino for sneutrino masses ranging from 100 to 1000 GeV. The gaugino component of the chargino couples to the sneutrino and the cross-section strongly depends on the t-channel contribution. The dashed line corresponds to the higgsino-like scenario. Since the higgsino component of the chargino does not couple to the sneutrino, he production cross-section is basically independent from the sneutrino mass.

Besides the parameters describing the chargino mass, M_2, μ and $\tan\beta$ (see Section 1.3.1), obviously, the sneutrino mass, $M_{\tilde{\nu}_e}$, is needed as a fourth parameter to describe the chargino production cross-section.

As R-parity conservation is assumed charginos eventually decay into the LSP. Only models shall be considered where the LSP is the lightest neutralino. The possible chargino decays are illustrated in Figure 1.7.

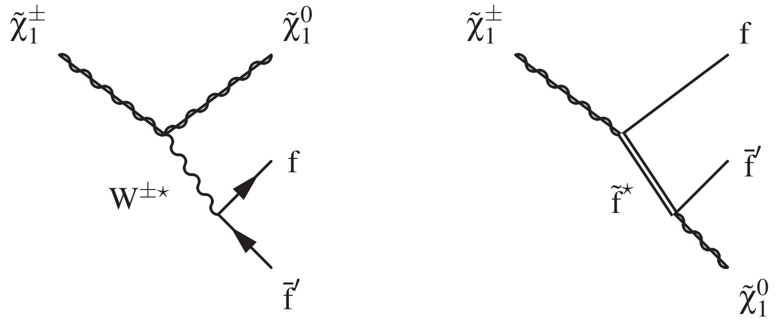

Figure 1.7: R_P conserving chargino decays into the lightest neutralino. The decay via a W boson is the dominant one as long as the slepton and squark masses are large ($\gg M_W$).

As long as the slepton and squark masses are large ($\gg M_W$) the dominant chargino decay proceeds via a virtual W boson. Therefore, the chargino decay is fully described by the parameters describing the chargino and neutralino mass (M_1, M_2, μ and $\tan\beta$, see Section 1.3.1) and the sfermion mass, $M_{\tilde{f}}$.

1.3.5 Special Supersymmetry Breaking Scenarios

The interpretation of experimental results is hopeless if it is to be done in a parameter space with more than 100 dimensions (see Section 1.2.6). The predictive power of such a theory is limited. The introduction of special SUSY breaking scenarios, describing explicitly the interaction between hidden and observable sector (see Section 1.2.6), comes along with constraints on the parameter space. The following paragraphs give an overview on a few selected supersymmetry breaking scenarios and their parameter spaces.

Gravity Mediated Supersymmetry Breaking

Gravity mediated supersymmetry breaking scenarios assume that the interaction between hidden and observable sector is purely gravitational. The minimal supergravity (mSUGRA) is one of the most constrained theoretical frameworks. It assumes the unification of the gaugino masses at the GUT scale, the unification of the fermion Yukawa couplings at the GUT scale as well as the unification of the sfermion masses at the GUT scale. In order to determine the running of couplings from the Planck scale down to the GUT scale, it requires additional assumptions for the GUT gauge group. Finally, mSUGRA models are fully described by:

m_0: a common scalar mass at the GUT scale

M_2: the $SU(2)$ gaugino mass parameter at the electroweak scale

$\tan\beta$: the ratio of the vacuum expectation values of the two Higgs doublets sign(μ): the sign of the mixing parameter of the Higgs doublet fields

A_0: a universal trilinear sfermion/Higgs coupling

LEP data is often discussed in the framework of mSUGRA$_{\mathrm{LEP}}$. The use of less strict assumptions leads to an extension of the mSUGRA parameter space. Additional parameters are the size of the Higgs mixing parameter, μ, and the mass of the pseudoscalar Higgs at the electroweak scale, M_A.

In mSUGRA and mSUGRA inspired scenarios the LSP is either the lightest neutralino, $\tilde{\chi}_1^0$, or the lightest stau, $\tilde{\tau}_1$.

Gauge Mediated Supersymmetry Breaking

In gauge mediated supersymmetry breaking scenarios (GMSB) the interaction between hidden and observable sector is described by gauge interactions [30]. The hidden sector communicates via, e.g. new gauge interactions with particles in a so-called messenger sector, which in turn, communicates via ordinary gauge interactions with the observable sector. That is to say, the messenger particles communicate between a supersymmetry breaking vacuum expectation value, $\langle F \rangle$, and the MSSM particles. The MSSM soft terms arise from loop diagrams involving the messenger particles. Six parameters determine the GMSB framework:

Λ: a universal mass scale of the SUSY particles

N: the number of messenger pairs

M_m: the messenger mass scale

$\tan\beta$: the ratio of the vacuum expectation values of the two Higgs doublets

sign(μ): the sign of the mixing parameter of the Higgs doublet fields

$\sqrt{F}$: the SUSY breaking scale (alternatively, the gravitino mass, $m_{3/2}$, can be used)

In contrast to the mSUGRA framework the LSP in GMSB scenarios is always the gravitino, $\tilde{G}$.

Anomaly Mediated Supersymmetry Breaking

The anomaly mediated supersymmetry breaking (AMSB) scenarios exploit the fact that rescaling anomalies in the super-gravity Lagrangian always give rise to soft mass parameters and thus anomalies always contribute to the SUSY breaking mechanism. This mechanism refers to a hidden sector of a multidimensional theory. In AMSB gaugino masses are generated at one loop and scalar masses at two loops as a consequence of the super-Weyl anomaly [31, 32]. Four parameters describe the AMSB framework:

m_0: a common scalar mass

$m_{3/2}$: the gravitino mass

$\tan\beta$: the ratio of the vacuum expectation values of the two Higgs doublets

sign(μ): the sign of the mixing parameter of the Higgs doublet fields

In AMSB frameworks one finds that either the lightest sneutrino or the lightest neutralino is the LSP.

Chapter 2

The Analysis Keystone

The present analysis describes a search for charginos in e^+e^- collisions. Because of the huge SUSY parameter space the chargino production and decay properties are manifold and hence the search strategies are manifold. This Chapter gives an overview on chargino search strategies and introduces the concept relevant for this analysis.

2.1 Chargino Searches

In the following only the direct pair-production of the lightest chargino, $\tilde{\chi}_1^{\pm}$, and its decay into the lightest neutralino, $\tilde{\chi}_1^0$, are considered (It is assumed that the $\tilde{\chi}_1^0$ is the LSP or its lifetime is sufficiently large to escape detection.). Hence the signal events are described by:

$$e^+e^- \rightarrow \tilde{\chi}_1^+\tilde{\chi}_1^- \rightarrow f\bar{f}'\tilde{\chi}_1^0\, f''\bar{f}'''\tilde{\chi}_1^0 \tag{2.1}$$

The corresponding Feynman-diagrams are illustrated in Figure 1.5 and Figure 1.7. The kinematic properties of the final state particles, and therefore the event signature, depend on the mass difference between chargino and neutralino, ΔM:

$$\Delta M = M_{\tilde{\chi}_1^{\pm}} - M_{\tilde{\chi}_1^0} \tag{2.2}$$

Chargino search strategies can be roughly categorised by the value of ΔM. For large mass differences ($\Delta M \gtrsim 5\,\mathrm{GeV}$) the final state fermions are quarks or energetic leptons and the signal events can be identified by missing energy (carried away by the neutralinos) plus jets or isolated leptons.

For very small mass differences ($\Delta M \lesssim M_\pi$) the chargino lifetime increases as depicted in Figure 2.1 and the chargino decay vertex should be well separated from the interaction point. High ionisation tracks from heavy stable charged particles and/or secondary vertices are the signatures for this scenario. This method is sensitive up to mass differences $\sim O(100\,\mathrm{MeV})$.

Results from the OPAL collaboration for both the large and the very small ΔM searches are shown in Figure 2.2. As indicated in Figure 2.2 a small ΔM band remains uncovered. It will be referred to as the ΔM gap. This is the regime of small mass differences which will be discussed in detail in the following Section.

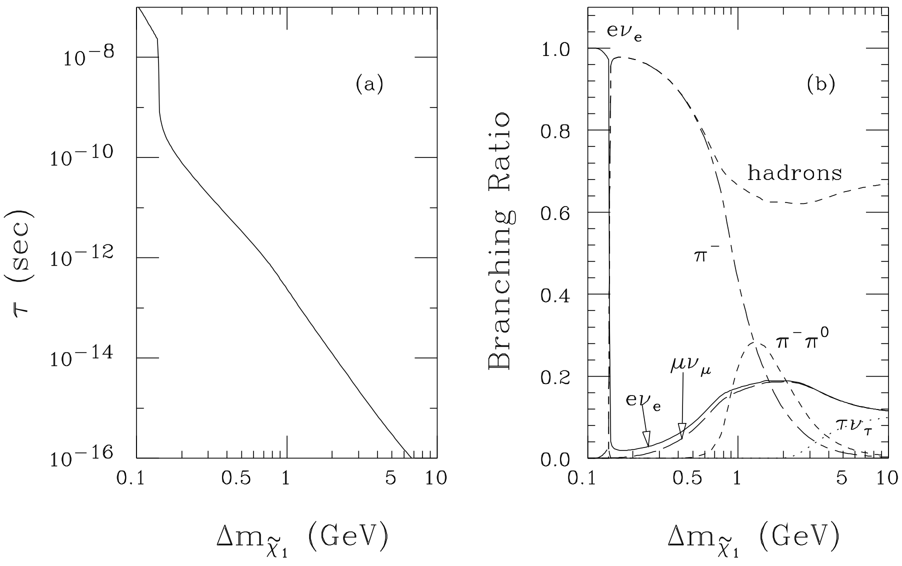

Figure 2.1: Left: Chargino lifetime τ as a function of the mass difference between the chargino and the lightest neutralino. For mass differences below the pion mass the lifetime increases significantly and the chargino vertex is well separated from the interaction point. Right: Chargino decay branching ratios as a function of the mass difference [33].

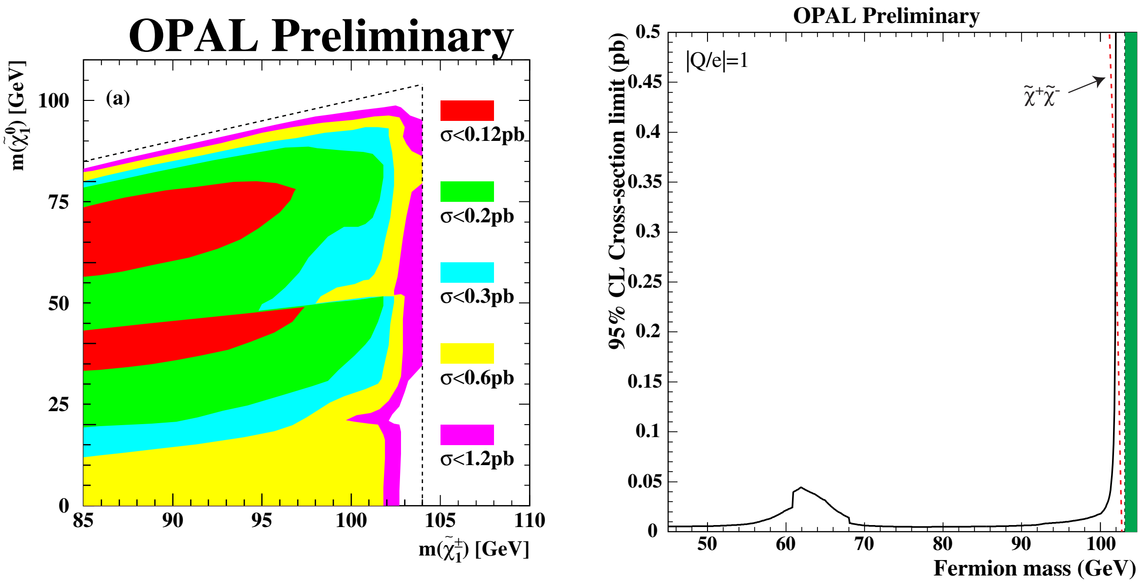

Figure 2.2: Left: chargino upper cross-section limits in case of large mass differences, ΔM. The dashed lines mark the kinematic limits. The small white band in the upper half indicates the region where the search is insensitive. Right: Upper cross-section limit in case of long lived charginos (very small mass differences, ΔM). The dashed line illustrates the predicted chargino cross-section.

2.2 The Case of Small Mass Differences

This analysis investigates scenarios with a mass difference in the intermediate ΔM range ($M_\pi \lesssim \Delta M \lesssim 5$ GeV), the so-called small ΔM scenarios. The described 'standard' searches are insensitive in this region due to the peculiar event signature.

2.2.1 The Signal Event Signature

Generally, prompt chargino decays are expected in the small ΔM regime. The signal final state is characterised by very little hadronic or leptonic activity accompanied by a large amount of missing energy. The size of the visible energy is in the order of the mass difference as long as the centre-of-mass energy is not significantly larger than twice the chargino mass. The consequences of this signature affect

- Trigger
  If the mass difference is too small the amount of energy deposited in the detector and the number of reconstructed tracks might be to small to trigger the data acquisition.
- Background
  One class of background events, the so-called two-photon events, depicted in Figure 2.3, have a very similar event signature. The beam electrons[1] carry away most of the energy when disappearing in the beam pipe. Only the low energy remnants from the two-photon interaction are visible in the detector. The cross-section of two-photon events is several orders of magnitude larger [2] than the expected signal cross-section. The above described search strategy for large ΔM would mainly select two-photon events. The sketch in Figure 2.4 illustrates the similarity of signal and two-photon background events.

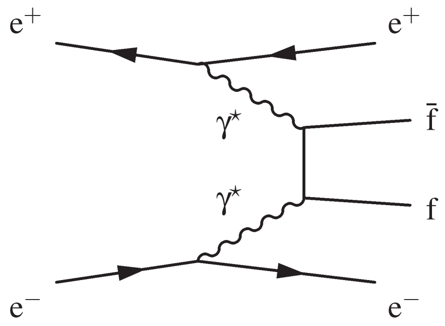

Figure 2.3: An illustrating example of a two-photon interaction. Shown is the reaction $e^+e^- \rightarrow e^+e^-f\bar{f}$, proceeding via the exchange of two (virtual) photons.

To recapitulate, due to the small chargino life-time and the large two-photon background neither the search for missing energy plus jets/leptons nor the search for heavy, stable, charged particles

[1]Both electrons and positrons are referred to as electrons.

[2]A more detailed description of two-photon interactions follows in Chapter 3.

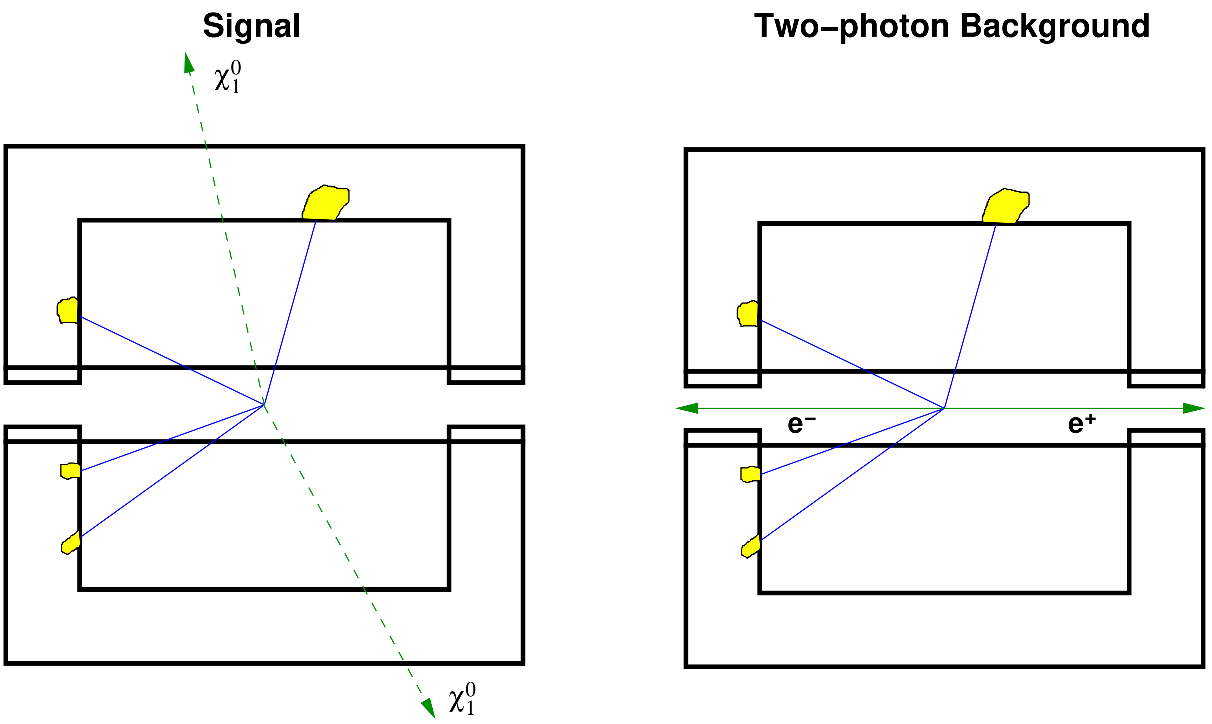

Figure 2.4: Detector sketch of the signal signature (left) and of a typical two-photon event signature (right). The signal signature is characterised by missing energy (carried away by the neutralinos) and only little detector activity from the remaining chargino decay products, whereas in case of two-photon events most of the energy disappears in the beam pipe with the beam electrons and only the remnants of the two-photon interaction are visible in the detector.

is applicable in the small ΔM regime. In order to fill the ΔM gap a third search strategy has to be found. A method was proposed which was already used in [34] for the search for heavy charged leptons which are nearly mass degenerate with their neutrino. If the chargino search is restricted to events which are accompanied by a detectable energetic photon from initial state radiation (ISR), the trigger algorithm should be fully efficient and signal events become distinguishable from two-photon background [33]. This method is described in the following.

2.2.2 The ISR Method

Initial State Radiation

In e^+e^- scattering real photons can be radiated from the incoming leptons as shown in Figure 2.5. The energy and the angular distributions of these initial state radiation (ISR) photons depend strongly on the e^+e^- process and the centre-of-mass energy.

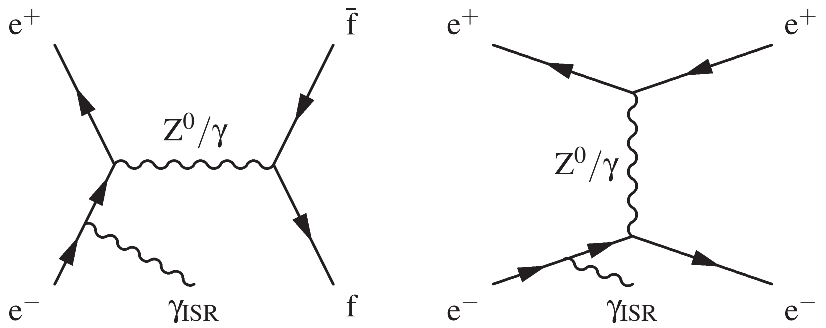

Figure 2.5: QED corrections in form of initial state radiation (ISR) in e^+e^- scattering.

Initial State Radiation and Signal Events

Providing that the ISR photon can be identified within the detector acceptance and the ISR photon energy is sufficiently large, signal events can easily tagged by these photons, even if the remaining detector activity is very small. The downside of this selection criterion is the fact that only a small fraction of signal events is accompanied by hard ISR photons. However, the large predicted cross-section for chargino pair-production legitimates this restriction.

Initial State Radiation and Two-Photon Events

As already mentioned above the most severe background for the small ΔM chargino searches comes from two-photon events where both beam electrons disappear in the beam-pipe. In case of radiative two-photon events a sufficiently large transverse momentum of an ISR photon, p_T^γ, forces at least one beam electron into the detector. The additional deposited energy from the electron discriminates two-photon background events from signal events. This effect is depicted in Figure 2.6.

The minimum required p_T^γ can be related to the minimum accessible angle, θ_D^{min}, in the detector where electrons still can be detected [35]:

- The interesting two-photon events are $e^+e^- \rightarrow e^+e^-\gamma_{ISR}\gamma^{(\star)}\gamma^{(\star)} \rightarrow e^+e^-\gamma_{ISR}X$ where X denotes the two-photon interaction remnants.

- The maximum transverse momentum carried away by the two beam electrons without being detected is given by

$$p_T^{max} = (E^+ + E^-)\sin\theta_D^{min} \tag{2.3}$$

where the electron (positron) energy is indicated by E^- (E^+). With E^γ (energy of the ISR photon) and E^X (energy of the X system) the equation can be re-written

$$p_T^{max} = (\sqrt{s} - E^X - E^\gamma)\sin\theta_D^{min} \tag{2.4}$$

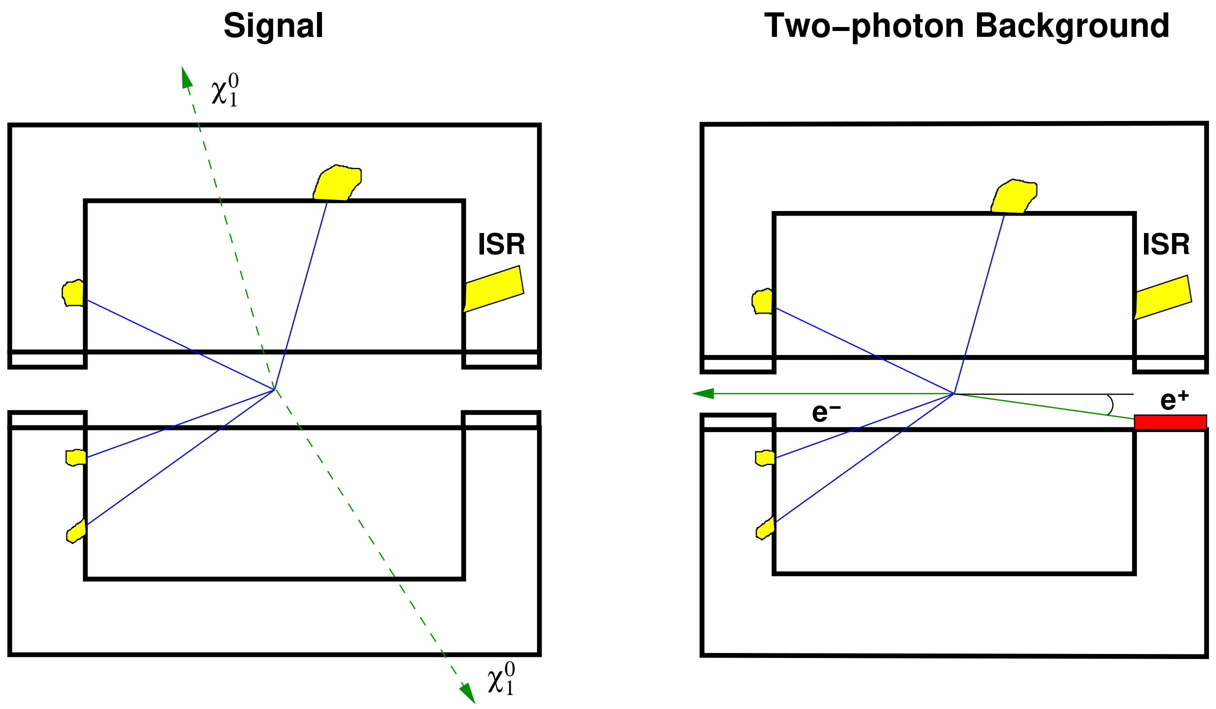

Figure 2.6: Selecting events with an additional photon from ISR leads to an additional neutral particle signature in the detector in case of signal events (left). If the transverse energy of the ISR photon is sufficiently large two-photon events (right) become distinguishable from signal events due to (at least) one beam electron forced into the detector.

- On the other side the $\gamma^{\mathrm{ISR}} + X$ system carries at least the transverse momentum $p_{\mathrm{T}}^{\mathrm{min}}$

$$p_{\mathrm{T}}^{\mathrm{min}} = p_{\mathrm{T}}^{\gamma} - p_{\mathrm{T}}^{X} \tag{2.5}$$

  with $p_{\mathrm{T}}^{\gamma} = E_{\mathrm{T}}^{\gamma}$ and p_{T}^{X} the transverse momentum of the X system.

- The transverse momentum $p_{\mathrm{T}}^{\mathrm{min}}$ has to be balanced by the transverse momentum of the beam electrons, $p_{\mathrm{T}}^{\mathrm{e}}$. As soon as $p_{\mathrm{T}}^{\mathrm{e}}$ $(= p_{\mathrm{T}}^{\mathrm{min}})$ becomes larger than $p_{\mathrm{T}}^{\mathrm{max}}$ at least one beam electron will be scattered into the detector. This requirement can be written as

$$p_{\mathrm{T}}^{\gamma} - p_{\mathrm{T}}^{X} > (\sqrt{s} - E^{X} - E^{\gamma}) \sin\theta_{\mathrm{D}}^{\mathrm{min}} \tag{2.6}$$

$$\Leftrightarrow \qquad p_{\mathrm{T}}^{\gamma} > \frac{(\sqrt{s} - E^{X}) \sin\theta_{\mathrm{D}}^{\mathrm{min}} + p_{\mathrm{T}}^{X}}{1 + \frac{E^{\gamma}}{p_{\mathrm{T}}^{\gamma}} \sin\theta_{\mathrm{D}}^{\mathrm{min}}} \tag{2.7}$$

- Using $\frac{E^{\gamma}}{p_{\mathrm{T}}^{\gamma}} \geqslant 1$ Equation (2.7) becomes

$$p_{\mathrm{T}}^{\gamma} > \frac{(\sqrt{s} - E^{X}) \sin\theta_{\mathrm{D}}^{\mathrm{min}} + p_{\mathrm{T}}^{X}}{1 + \sin\theta_{\mathrm{D}}^{\mathrm{min}}} \tag{2.8}$$

- E^X and p_T^X are of order ΔM times a modest boost factor, and are negligible in the scenarios:

$$E_\mathrm{T}^\gamma = p_\mathrm{T}^\gamma \gtrsim p_\mathrm{T}^{\gamma\,\mathrm{min}} = \sqrt{s}\frac{\sin\theta_\mathrm{D}^\mathrm{min}}{1+\sin\theta_\mathrm{D}^\mathrm{min}} \tag{2.9}$$

Therefore, requiring a photon with $E_\mathrm{T}^\gamma > p_\mathrm{T}^{\gamma\,\mathrm{min}}$ in the final state allows an efficient reduction of two-photon processes by vetoing events with a scattered beam electron in the detector. From Equation (2.9) can be the importance of the detector hermeticity deduced. The better the angular coverage in the detector (the smaller θ_D^min), the smaller is the required transverse energy, which in turn increases of course the signal detection efficiency.

2.2.3 The Search Strategy

The search strategy for nearly mass degenerate charginos and neutralinos can be summarised in two steps:

1 Consider only a sub-sample of events, namely events accompanied by a high energy ISR photon.

2 Require that the transverse momentum (transverse energy) of the ISR photon satisfies the relation (2.9). Two-photon events which beforehand had the same signature as signal events are then tagged by additional energy deposited in the detector by the beam electrons.

2.3 SUSY Scenarios with Small Mass Differences

As explained in Section 1.3.1 within the MSSM the chargino and neutralino masses depend on four parameters: the ratio of the two Higgs vacuum expectation values, $\tan\beta$; the Higgs mixing parameter, μ and the $U(1)$ and $SU(2)$ gaugino mass parameters, M_1 and M_2, respectively. The chargino and neutralino masses can be expresses as:

$$\begin{aligned} M_{\tilde{\chi}^\pm_{i=1,2}} &= M_{\tilde{\chi}^\pm_{i=1,2}}(M_2,\mu,\tan\beta), \\ M_{\tilde{\chi}^0_{i=1\ldots4}} &= M_{\tilde{\chi}^0_{i=1\ldots4}}(M_1,M_2,\mu,\tan\beta). \end{aligned}$$

Small mass differences, ΔM, occur in the following two scenarios:

- In the higgsino-like scenario is $|\mu| \ll M_2$, the lightest chargino $\tilde{\chi}_1^\pm$ is almost a higgsino. In this scenario the lightest chargino and neutralino are mass-degenerate ($M_{\tilde{\chi}_1^\pm} \simeq M_{\tilde{\chi}_1^0} \simeq |\mu|$) for very large values of M_2.

- If $M_2 \ll |\mu|$, the lightest chargino $\tilde{\chi}_1^\pm$ is almost a gaugino with $M_{\tilde{\chi}_1^\pm} \sim M_2$. The mass of the lightest neutralino $\tilde{\chi}_1^0$ is given by $M_{\tilde{\chi}_1^0} \sim \min(M_1, M_2)$. Therefore small mass splittings only occur if $M_2 < M_1$. If the gaugino mass parameters, M_1, M_2 and M_3 are assumed to be identical at the GUT scale, as assumed in the mSUGRA framework, then the relation between M_1 and M_2 at the electroweak scale can be obtained from RG:

$$M_1 \quad = \quad \tan^2\theta_W M_2 \simeq \frac{1}{2} M_2. \qquad (2.10)$$

In this case the model does not predict a small ΔM gaugino-like scenario. In more general scenarios, Equation (2.10) does not hold and can be generalised introducing an arbitrary factor, R_S:

$$M_1 \quad = \quad R_\mathrm{S} M_2. \qquad (2.11)$$

Some string theory motivated SUSY scenarios [36] explicitly predict the non-unification of the gauginos masses at the GUT scale and thus $R_\mathrm{S} \neq \tan^2\theta_W$. For $R_\mathrm{S} \gtrsim 1$ the lightest chargino and neutralino are degenerate in mass with $M_{\tilde{\chi}_1^\pm} \simeq M_{\tilde{\chi}_1^0} \simeq M_2$.

The distinction between higgsino-like and gaugino-like scenarios is important not only due to the different expected signal cross-sections (see Section 1.3.4). As discussed before the chargino pair production mechanism depends on the chargino content. Since the ISR characteristic (mainly the angular distribution) in the s-channel differs from the one in the t-channel, different signal selection efficiencies are expected. For the described analysis method it is crucial to treat both scenarios separately.

From this discussion it can deduced in which of the introduced special supersymmetry breaking scenarios (see Section 1.3.5) small mass differences occur. Definitely, only those frameworks with the lightest neutralino as LSP come into consideration and thus GMSB models drop out. In mSUGRA models only the higgsino-like scenario can be realised due to the assumed gaugino mass unification at the GUT scale. The situation is different in AMSB frameworks. Here the ratio of the gaugino masses is $R_\mathrm{S} = M_1/M_2 \approx 2.8$ and thus gaugino-like scenarios emerge almost naturally. The results of this analysis will be interpreted in the unconstrained MSSM, mSUGRA as well as in the AMSB framework.

Chapter 3

Experimental Apparatus

The interplay between theoretical predictions and experimental discoveries has proven to be the most crucial point in the development of elementary particle physics. While particle accelerators and colliders have helped to provide the experimental evidence for the basis of the SM, the theoretical frameworks challenged the experimental side of physics.

The previous Chapter described the relevant theoretical background for this thesis. This Chapter introduces the utilised experimental instruments, namely the LEP storage ring, the OPAL detector, the future TESLA Linear Collider and the future TESLA detector as well as a set of computer tools needed to analyse and interpret experimental data.

3.1 Accelerators and Colliders

The development of accelerator techniques is driven by two points. First, the provided beam energy which has to be increased in order to gain deeper insights into the structure of matter due to the resolution of smaller distances. Second, the luminosity $\mathcal{L}$, defined as the event rate $\mathrm{d}N/\mathrm{d}t$ of a process divided by the corresponding cross-section, should be large enough in order obtain a decent event rate:

$$\mathcal{L} = \frac{1}{\sigma(\sqrt{s})}\frac{\mathrm{d}N}{\mathrm{d}t}. \tag{3.1}$$

The luminosity of e^+e^- colliders can be described in terms of machine parameters: the number of particles per bunch, N_e, the transverse beam dimensions at the interaction point in x and y, $\sigma_{x,y}$ and the number of bunch crossings (BX) per second, f_b:

$$\mathcal{L} = \frac{N_\mathrm{e}^2 f_b}{4\pi\sigma_x\sigma_y}. \tag{3.2}$$

Due to the asymptotic $\frac{1}{s}$-behaviour of annihilation cross-sections (see Figure 3.1) at centre-of-mass energies beyond the Z peak the luminosity has to be significantly higher than at the Z peak.

In order to obtain a decent event rates the luminosity has to be increased with increasing centre-of-mass energy which requires almost always a change in the basic accelerator concept. A nice example for this is the next generation of e^+e^- Colliders. In order to reach energies

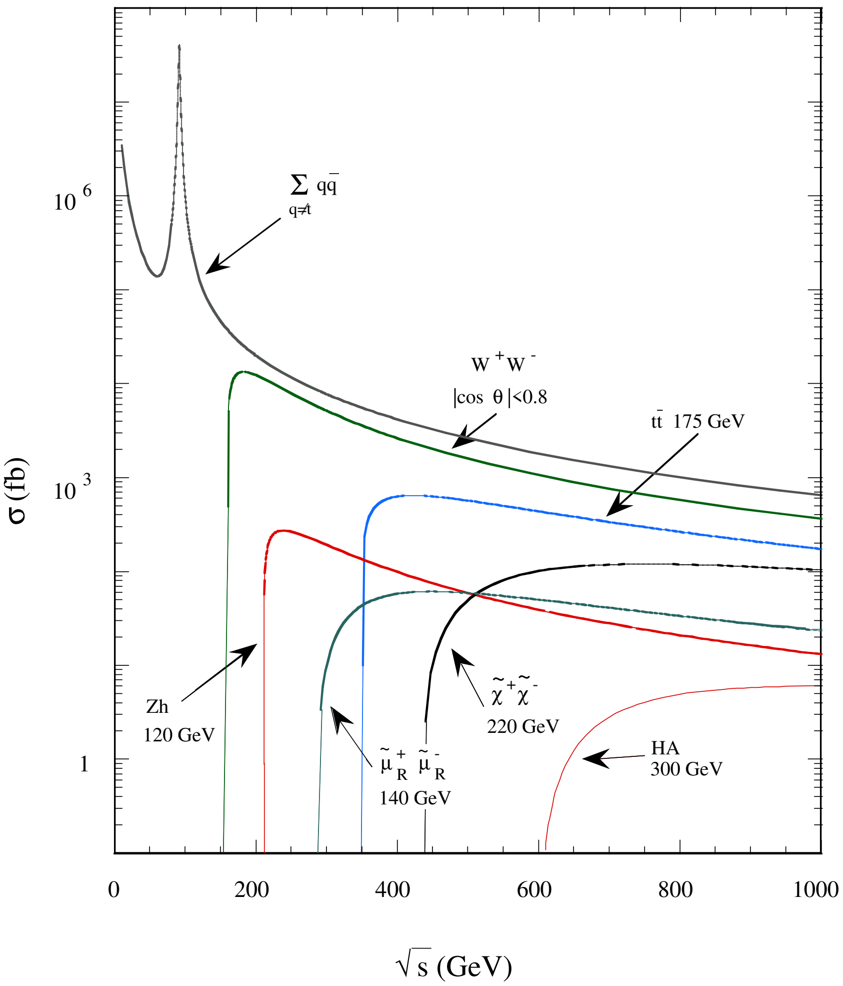

Figure 3.1: Cross-sections in e^+e^- collisions of a list of selected processes as a function of the centre-of-mass energy. Colliders have to regard for the significantly smaller cross-sections when operated at centre-of-mass energies beyond the Z peak.

well above a couple of 100 GeV it was proposed that a linear collider shall replace the present circular colliders. The ideas of circular and linear colliders are completely different and the main concepts of those machines shall be briefly compared.

3.1.1 The LEP Storage Ring

The Large Electron Positron collider (LEP) has been built at CERN[1] close to Geneva, Switzerland, during the 1980s to study the electroweak interaction at energies up to 200 GeV. It was operated until 2000. As shown in Figure 3.2, it was a circular accelerator with a circumference of 27 km, located some 100 m below the surface. The first stage of LEP running (LEP I) started in 1989 and provided colliding beams with a centre-of-mass energy around 90 GeV. During

[1] CERN: formerly Centre Européen de Recherche Nucléaire, now European Organisation for Nuclear Research

the LEP II phase from 1996 to 2000 the centre-of-mass energy was continuously increased to a maximum of 208 GeV. While the LEP I physics program was dominated by the the study of the Z-resonance, LEP II aimed mainly for investigation of the properties of the W boson and the search for new phenomena.

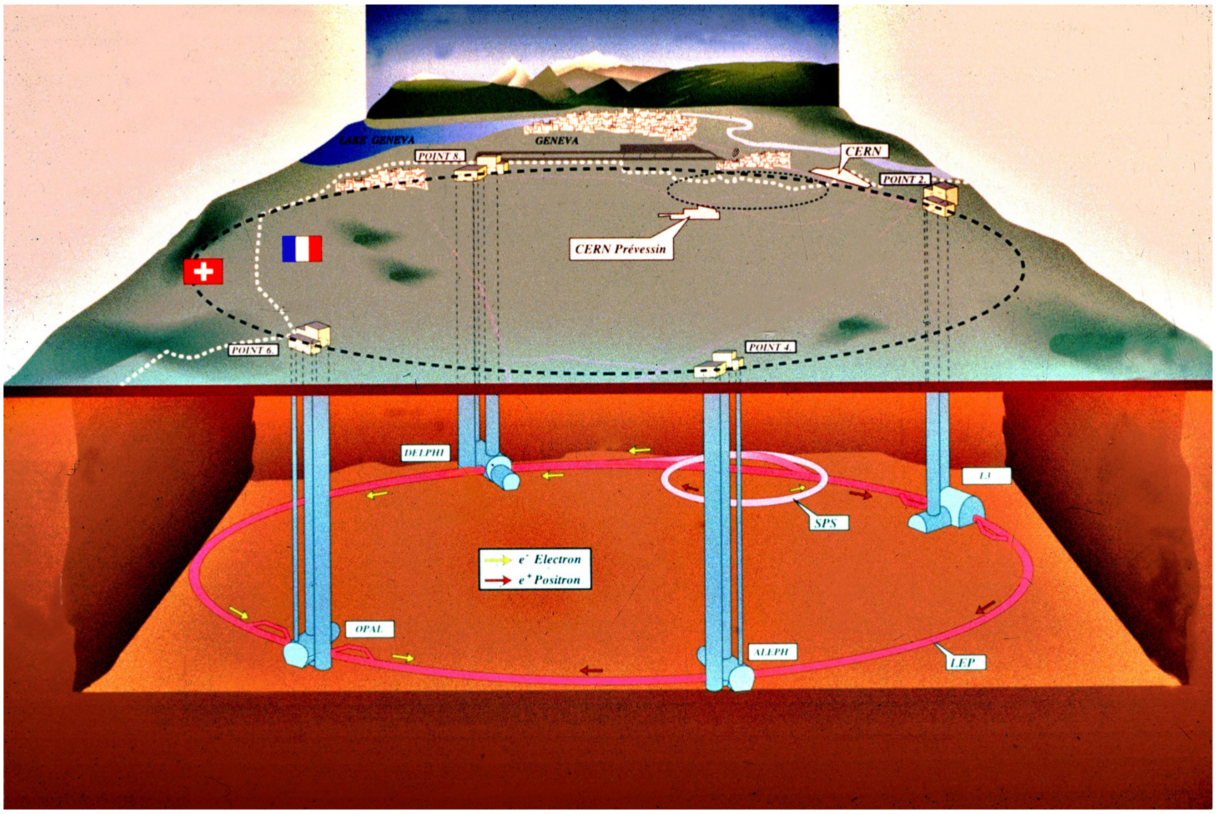

Figure 3.2: The LEP collider layout and the four LEP experiments ALEPH, DELPHI, L3 and OPAL at CERN.

The increase in beam energy was reached with the installation of new super-conducting accelerating cavities complementing the normal-conducting radio frequency (RF) cavities. The integration of super-conducting quadrupoles on either side of each of the four experiments and the replacement of one particle bunch by four closely spaced bunchlets resulted in a peak luminosity of about $10^{32}\mathrm{cm}^{-2}\mathrm{s}^{-1}$ (which corresponds to three times the peak luminosity reached at LEP I) at a BX rate of 44 kHz [37].

During its final year LEP reached its technical limits. A further energy increase would not have been possible without a major redesign of the accelerator. The reason for this can be found in the main disadvantage of $\mathrm{e}^+\mathrm{e}^-$ circular accelerators. Charged particles lose energy in form of synchrotron radiation when forced on a circular path. The energy loss ΔE is proportional to $1/m^4$ (where m is the accelerated particle mass) and therefore negligible for heavy particles like protons. This is not the case for electrons and positrons. The energy loss of a highly relativistic electron (or positron) of energy E on a circular trajectory of radius R is given by:

$$\Delta E[\text{GeV}] \quad = \quad 8.85 \cdot 10^{-8} \frac{E^4[\text{GeV}^4]}{R[\text{km}]}. \tag{3.3}$$

This means that the electrons and positrons of a 100 GeV LEP beam lost ~ 2 GeV per revolution. An amount of energy which had to be restored to the beam by the high frequency resonator cavities. An increase in the beam energy by a factor of two would have increased the energy loss by a factor 16! From Equation (3.3) can be deduced that the size of the radius of the ring can counteract this energy loss. It is obvious that the optimal storage ring with almost no energy loss due to synchrotron radiation would have an infinite radius, that is to say it has a linear construction. The Linear Collider concept will be discussed in the following Section. Table 3.1 summarises the most important LEP machine parameters.

3.1.2 The TESLA Linear Collider

The TESLA[2] Linear Collider is project for a new large-scale facility planned and developed by an international collaboration at DESY in Hamburg, Germany. A detailed description of the TESLA project can be found in [38–44]. TESLA aims for a centre-of-mass energy of up to ~ 800 GeV. Besides TESLA, there are the NLC[3] [45] and the JLC [4] [46] which follow a similar goal with different accelerator technologies.

One of the main challenges for these projects is to provide a sufficiently high luminosity while operating at centre-of-mass energies ranging from the Z peak to well above the Z peak. Moreover, the accelerated particles are not stored in a linear collider like in a storage ring, which makes it difficult to accumulate the luminosity.

A sketch of the planned TESLA Linear Collider layout is shown in Figure 3.3. The overall length is 33 km. Besides the e^+e^--interaction region a second detector (e.g. for $\gamma\gamma$-interactions) might be commissioned. The TESLA machine can be completed with an integrated X-ray laser laboratory.

The major difference between the TESLA Linear Collider and the other two Linear Collider concepts is the choice of a superconducting material for the accelerator structures. This has the advantage of an extremely small power loss within the cavities and in turn, allows to operate the accelerator with a rather moderate operating frequency $f = 1.3$ GHz [5]. Higher frequencies lead in general to smaller accelerating structures with larger accelerating gradients. On the other side this demands tighter structure and alignment tolerances. In addition, beam-induced electro-magnetic fields (wake-fields), which create a large energy spread within one particle bunch, scale quadratically with the accelerating frequency and are clearly an argument in favour of smaller frequencies.

The cavity material and thus the operating frequency governs the time structure of the beam. TESLA's superconducting accelerator structures allow for rather long RF pulses (1 ms) and a

[2] TESLA: Tera Electron Volt Energy Superconducting Linear Accelerator
[3] NLC: Next Linear Collider
[4] JLC: Japan Linear Collider
[5] For comparison, the normal conducting accelerator structures foreseen for NLC and JLC are operated at around 11 GHz.

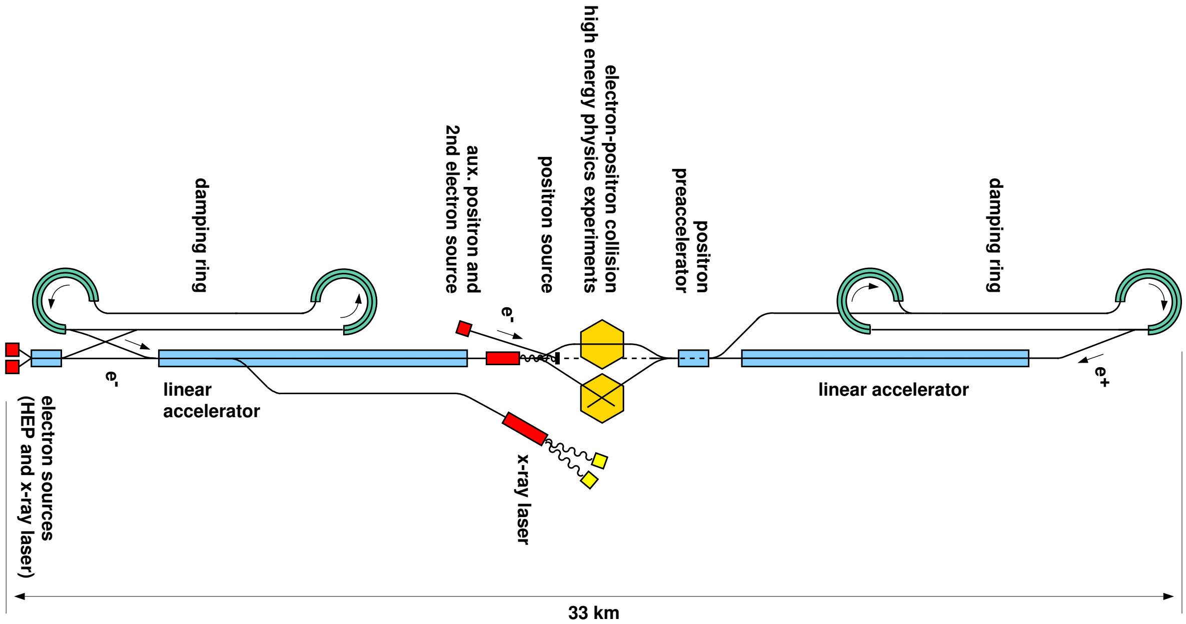

Figure 3.3: Sketch of the overall layout of the TESLA Linear Collider.

relatively large bunch spacing of 337 ns. A total of 2820 bunches will be combined in one so-called TESLA train. The train repetition rate is 5 Hz. An adequate luminosity will be gained by reducing the beam dimensions at the interaction point (see Equation (3.2)) to $500 \times 5\text{nm}^2$.

It is planned that in the first TESLA stage ($\sqrt{s} = 350 - 500$ GeV) a total of 21 024 superconducting cavities powered by some 600 klystrons will provide beam-energies up to 250 GeV. A possibilty to run with polarised electrons is foreseen. One upgrade option opens the room for polarised positrons. In the second phase TESLA will be operated at a centre-of-mass energy of 800 GeV or more, depending on the maximum achievable accelerating gradient. The essential TESLA machine parameters can be found in Table 3.1.

	LEP	TESLA	
$\sqrt{s}$	208	500	GeV
$\mathcal{L}$	$1 \cdot 10^{31}$	$3 \cdot 10^{34}$	cm^{-2}s^{-1}
IP beam sizes (x,y)	200 000, 2 500	553, 5	nm
bunch spacing	22 000	337	ns
bunch charge	$3.0 \cdot 10^{11}$	$2.0 \cdot 10^{10}$	$1/e$

Table 3.1: Comparison of the LEP and TESLA machine parameters.

The Linear Collider and other Accelerators

Before any of the Linear Collider projects will be realized, hadron collider machines like the TEVATRON and LHC will have collected a huge amount of high energy physics data at centre-of-mass energies between 2 TeV and 14 TeV. The LHC experiments will be the first experiments whose energy is clearly in the regime of new physics. They will improve todays understanding of Nature by far. An e^+e^- Linear Collider will operate in parallel to the hadron machines. Only the additional complementary information provided by a Linear Collider will make high precision results possible on various fields like Higgs physics, supersymmetry, electroweak physics or QCD.

3.2 Particle Detectors

The major goal of every collider particle detector can be summarized as follows: reconstruction (direct or indirect) of all particles produced in the primary particle interaction or subsequently. In order to accomplish this task the detector has to fulfil the following requirements and provide some important information:

- The detector should cover as much as possible of the complete solid angle (hermeticity).
- Charged particles can be identified via their momentum, charge and specific energy loss. Therefore a precise track reconstruction is essential.
- Electro-magnetic and hadronic energy measurements should provide additional information supporting the identification of electrons, photons and hadrons.
- Exploiting the minimal ionising character of muons dedicated muon detection devices outside of the detector permit the identification of muons.
- Finally, the detector should be able to measure the delivered absolute luminosity via a well known reference process as well as the beam energy and the beam polarisation.

This Section describes the OPAL detector, the proposed TESLA detector, their main detector components and how they tackle the listed demands.

3.2.1 The OPAL Detector

The OPAL[6] detector is described in detail in [47–62]. It was a multipurpose apparatus with almost full solid angle coverage. A three-dimensional cut-away view of the OPAL detector is shown in Figure 3.4. In the OPAL right-handed coordinate system the x-axis points towards the centre of the LEP ring, the y-axis points upwards and the z-axis points in direction of the electron beam. The polar angle θ and the azimuthal angle ϕ are defined with respect to the z-axis and x-axis, respectively.

Beginning from the interaction point the layered structure of the OPAL detector started with the silicon micro-vertex detector (SI) followed by the central tracking system which contained the central vertex chamber (CV), the central jet chamber (CJ) and the central z-chambers (CZ). The central tracking system was surrounded by the time-of-flight system (TOF). The detector

[6] OPAL: Omni Purpose Apparatus at LEP.

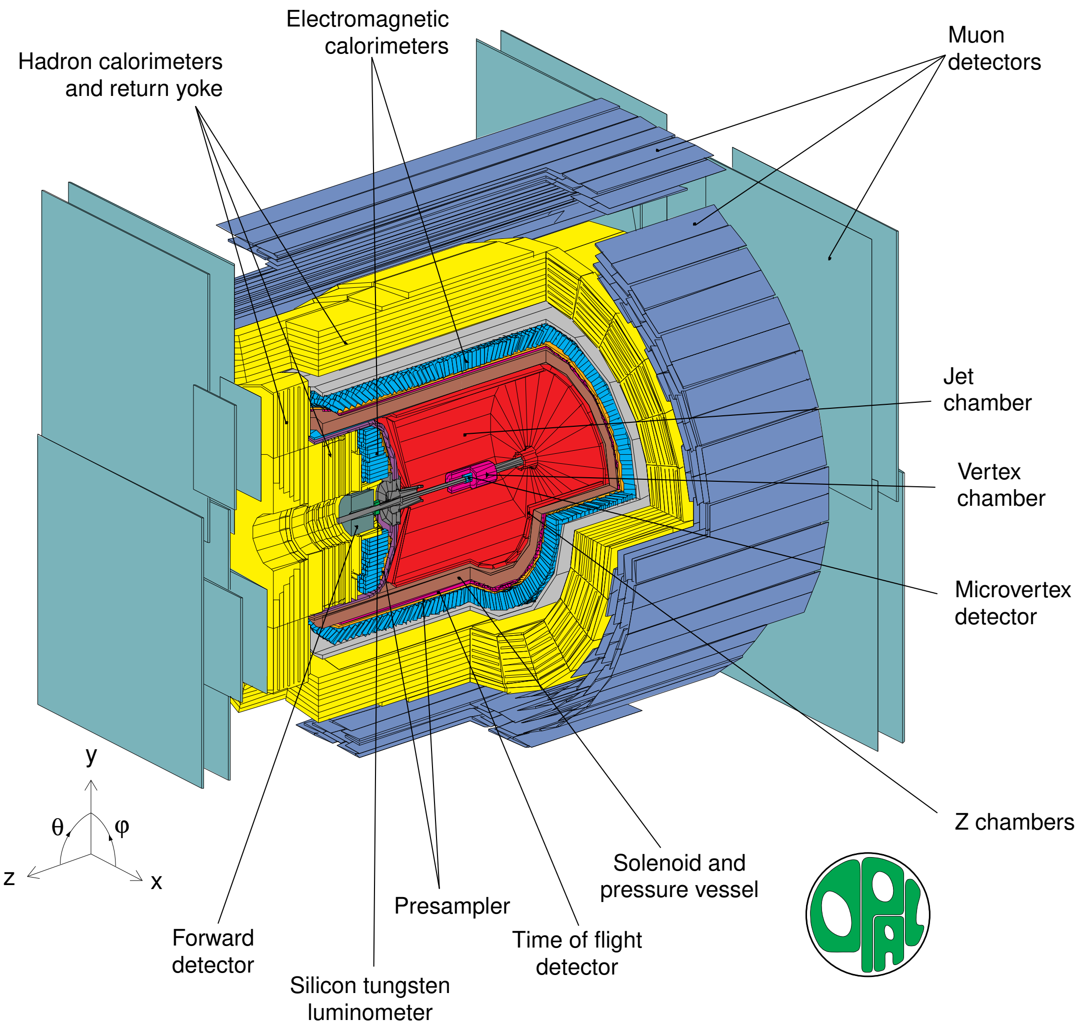

Figure 3.4: The OPAL detector.

was completed with the pre-sampler, the calorimeter system an the muon chambers. The forward region, the region close to the beam pipe at both ends of the OPAL detector, was covered with a system of forward detectors. The design and operation of each sub-detector is outlined below.

The Tracking System

The silicon micro-vertex detector was mounted between the LEP beam pipe and the inner cylindrical wall of the pressure vessel which contained the central tracking system. Its main purpose was the reconstruction of primary and secondary vertices. In its final assembly stage it consisted of two concentric layers of silicon strip detectors with radii 6.1 and 7.5 cm, respectively. The inner (outer) layer had 12 (15) so-called ladders, two single sided devices glued back-to-back allowing for spatial information in r, ϕ and z. The length of the layers was 18.3 cm providing an angular acceptance of $|\cos\theta| < 0.93$ and $|\cos\theta| < 0.89$, respectively. The point resolution was measured to $\sigma_\phi = 18\,\mu$m and $\sigma_z = 24\,\mu$m.

The three tracking detectors in the central tracking system worked by observing the ionisation of atoms by charged particles passing through: when the atoms are ionised, electrons are knocked out of their atomic orbitals, and are then able to move freely in the detector. These ionisation electrons are detected in the different parts of the tracking system. The central tracking system was installed inside a pressure vessel and operated with a gas mixture of argon (88.2%), methane (9.8%) and isobutan (2.0%) at a pressure of 4 bar. The aim of the central vertex chamber was to improve the measurement of secondary vertices of short lived particles and to provide a precise measurement of the z-coordinate near the interaction region. CV had a length of 1 m, an inner radius of 8.8 cm and outer radius of 23.5 cm. It was divided into 36 sectors. The inner part (up to a radius of 17.5 cm) of each sector was called the axial cell. Each axial cell contained 12 staggered signal wires parallel to the beam. A spatial resolution of 55 μm in r-ϕ and of 4 cm in z was reached. The so-called stereo cell was the outer part of each sector. Here six signal wires were oriented such that the angle between them and the axial wires was 4°, improving the z resolution to 700 μm.

CJ was the main OPAL tracking device. It was a drift chamber with a cylindrical shape with a length of 4 m and an inner (outer) radius of 25 cm (185 cm). It was used to measure the flight direction, momentum and charge of charged particles. Moreover, CJ was designed such that charged particles could be identified via their specific energy loss $\mathrm{d}E/\mathrm{d}x$ in the chamber gas. The chamber was divided into 24 sectors. Two neighbouring sectors were separated by a plane of cathode wires. Parallel to the beam axis, in the ϕ-centre of each sector, 160 potential wires alternating with 159 signal wires were mounted. With this geometry the maximal drift distance was 25.5 cm. Furthermore, this design allowed a homogeneous electric field and thus constant drift velocities for the electrons from gas ionisation. The cylinder was terminated on each side with a conical end plate. The coordinates of a charged particle track were then extracted via a drift-time measurement (r-ϕ) and via a comparison of the collected charge at both wire ends (z). The sum of the collected charge was used to determine the specific energy loss $\mathrm{d}E/\mathrm{d}x$. The central tracking system was embedded in a solenoid providing a magnetic field of 0.435 T which bent the tracks of charged particles and thus permited a measurement of their transverse momentum. The CJ performance can be summarised as follows: The average spatial resolution was 135 μm (r-ϕ) and 6 cm (z). With 159 track points the relative uncertainty on the measurement of the specific energy loss was 3.8%. The average transverse momentum resolution was found to be:

$$\left.\frac{\sigma_{p_t}}{p_t}\right|^{\mathrm{OPAL}} = \sqrt{0.0004 + \left(\frac{0.0015 \cdot p_t}{1\ \mathrm{GeV}}\right)^2}. \tag{3.4}$$

For tracks in the detector's barrel region ($|\cos\theta| < 0.72$) the CZ system enhanced the z resolution and the precision of the measurement of the track's polar angle θ. It consisted of 24 drift chambers with a thickness of 5.9 cm. Each chamber was divided into eight sectors which in turn contained six signal wires perpendicular to the beam direction. Again, a drift-time measurement was used to gain a point resolution of 1.5 cm in r-ϕ and 100–300 μm in z (depending on the drift distance).

The Time-of-Flight Counter

The TOF was used to measure the time-of-flight for particles coming from the interaction point. Its signals were used as trigger inputs and helped to reject cosmic rays. It consisted of a total of 160 scintillation counters forming a barrel of a radius of 2.36 m. With a length of 6.48 m the scintillators covered a angular region of $|\cos\theta| < 0.82$. The timing resolution which was determined at LEP I has been measured with $e^+e^- \to \mu^+\mu^-$ events to be 460 ps.

Analogous to the barrel region the end-cap region was equipped with scintillating tiles read out via a fibre link providing time-of-flight information for the region $0.82 < |\cos\theta| < 0.95$.

The Calorimeter System

The OPAL calorimeter system was divided into two main parts: the electro-magnetic calorimeter, ECAL and the hadron calorimeter, HCAL.

The ECAL was used to measure the energy and the position of electro-magnetically interacting particles like electrons, positrons and photons. It consisted of a barrel and two end-cap parts. A total of 11704 lead glass blocks were located outside the magnet coil and at the front of each end-cap. They provided an acceptance within $|\cos\theta| < 0.984$. Each lead-glass block had a cross-section of $10 \times 10\ \mathrm{cm}^2$ and a depth of roughly 37 cm, corresponding to an angular coverage of 40 mrad^2 and a radiation length of 24.6. The lead-glass blocks were instrumented with magnetic field tolerant phototubes detecting the Čerenkov light produced by the charged particles in an electro-magnetic shower emerging in the calorimeter block. The intrinsic spatial resolution of the ECAL was 11 mm. The intrinsic energy resolution in the barrel region was determined to

$$\left.\frac{\sigma_E}{E}\right|_{\text{ECAL barrel}}^{\text{OPAL}} \simeq 0.002 + \frac{0.063}{\sqrt{E/1\ \mathrm{GeV}}}, \tag{3.5}$$

whereas in the end-cap region the resolution was found to be

$$\left.\frac{\sigma_E}{E}\right|_{\text{ECAL end-cap}}^{\text{OPAL}} \simeq \frac{0.05}{\sqrt{E/1\ \mathrm{GeV}}}. \tag{3.6}$$

The energy measurement of hadrons is based on inelastic nuclear reactions between the incoming high energetic hadron and the nuclei of the detector material. The OPAL HCAL surrounded the ECAL. The return yoke of the magnetic coil equipped with thin streamer tubes was used as sampling calorimeter formed by alternating active layers of streamer tubes and passive layers of iron. The HCAL spanned radii from 3.39 meters to 4.39 meters, corresponding to more than four interaction lengths. The angular coverage was about 99%, of the solid angle and the energy resolution has been determined to be

$$\left.\frac{\sigma_E}{E}\right|_{\text{HCAL}}^{\text{OPAL}} \simeq \frac{1.2}{\sqrt{E/1\ \mathrm{GeV}}}. \tag{3.7}$$

The Muon Detector

The muon detector consisted of a barrel part and two end-cap parts and covered the iron yoke almost completely. While muons penetrated to the muon detector and left a single clean track, most hadrons were absorbed by the yoke. The location and direction of incident muons could be measured with four layers of 110 planar drift chambers in the barrel region and two layers of streamer tubes in the end-cap region. The spatial resolution in the barrel region was 1.5 mm in azimuthal and 2 mm in z direction. In the end-caps, a spatial resolution of 1 mm to 3 mm in the xy-plane was achieved.

The Forward Detector System

The importance of the detector forward region was already stressed in Section 2.2.2. A very good angular coverage is crucial for this analysis. The OPAL forward region was covered by electro-magnetic calorimeters, namely the silicon-tungsten calorimeter, SiW, the forward detector, FD and the gamma catcher, GC. Their main purpose was the determination of luminosity, by measuring the rate of low angle electron-positron pairs coming from Bhabha scattering ($e^+e^- \rightarrow e^+e^-$), a theoretically very well understood process. The exact location of the forward detector system is illustrated in Figure 3.5. The angular coverage was 25 mrad$< \theta <$59 mrad for SiW, 47 mrad$< \theta \lesssim$160 mrad for FD and 143 mrad$< \theta <$193 mrad for GC. The installation of additional shields in 1996 in order to protect the central detector against an increase of synchrotron radiation background which accompanied the increase of the centre-of-mass energy reduced the sensitive angular coverage of SiW to 33 mrad $< \theta <$ 59 mrad. Using these components the systematic error on the luminosity measurement was as small as 0.034%.

For this analysis a minimum accessible angle of θ_D^{min} =33 mrad can be related to a minimum required p_T^γ of $\approx 0.032\sqrt{s}$ (see Equation (2.9)).

3.2.2 The TESLA Detector

The requirements listed above apply of course also on a next generation detector like the TESLA detector. Nevertheless, the anticipated particle physics program of a Linear Collider demands a much higher performance:

- The vertex detector should be able to efficiently separate $c\bar{c}$ and $b\bar{b}$ final states.
- An excellent transverse momentum resolution of at least $\delta(1/p_t) = 5 \times 10^{-5}/1$ GeV should be achieved.
- The track recognition capabilities should work even on events with high track densities.
- The tracking and calorimetry devices should provide an optimum hermeticity.
- The energy and spatial resolution of the calorimeters should allow for the identification of non-standard physics events like non-pointing photons.
- Multi-parton final states demand an excellent jet energy resolution.

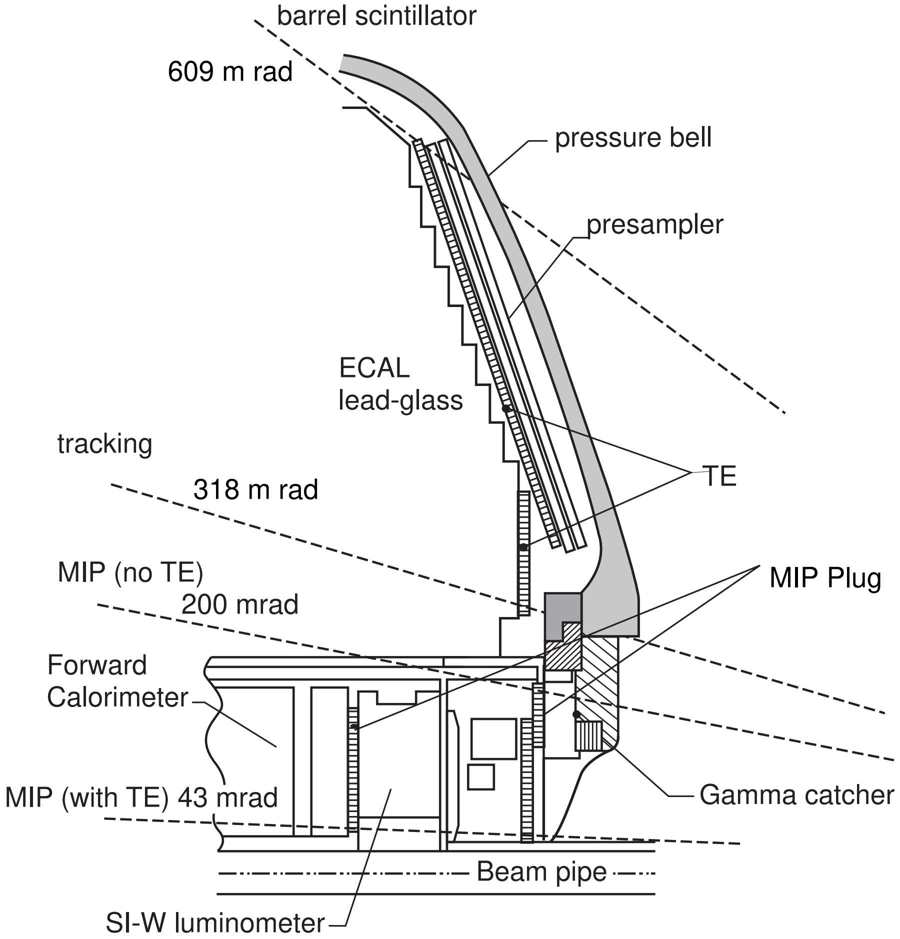

Figure 3.5: The OPAL end-cap region. The forward detectors SiW, FD and GC are located between the beam pipe and the electro-magnetic calorimeter (ECAL) .

The keyphrase in this context is ‘energy flow measurement’, a concept which combines the information from tracking and calorimetry in order to obtain an optimal estimate of the flow of particles and of the original parton four-momenta. The expected complexity of signal final states at TESLA and the presence of missing energy in fusion processes or SUSY reactions reduce the applicability of kinematic constraints and require highly efficient energy flow algorithms based on information provided by the detector components.

A three-dimensional cut-away illustrates the TESLA detector concept in Figure 3.6. A detailed description of the TESLA detector can be found in [41]. The detector proposal is still not final. For various detector components exist a number of alternative implementations. Not all of them can be covered here. This section outlines the main detector design.

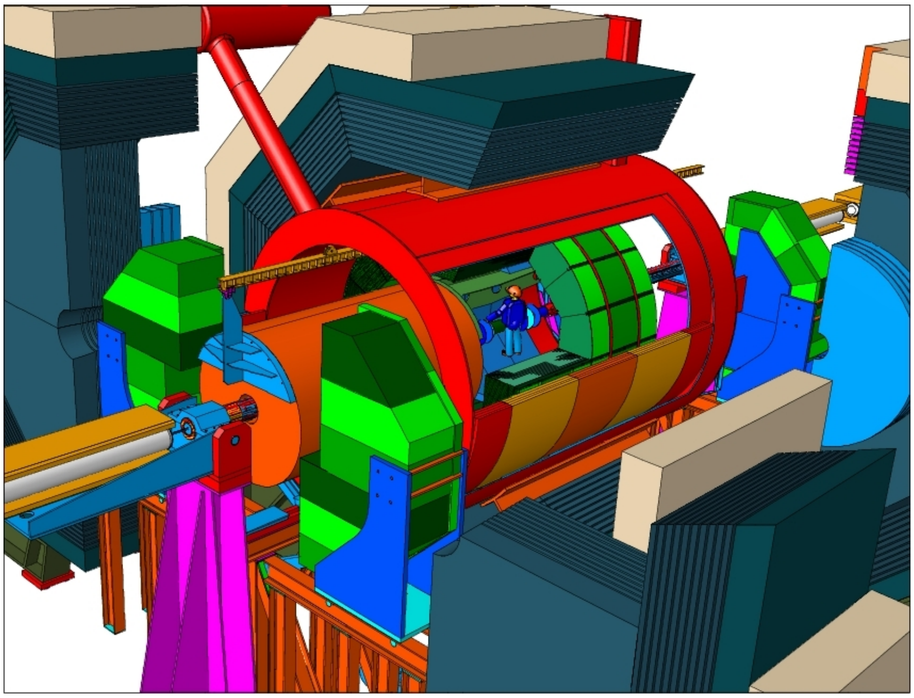

Figure 3.6: The TESLA Detector as proposed in [41].

The Tracking System

The TESLA tracking system consists of a series of single tracking devices. An overview of all components is shown in Figure 3.7. Close to the beam pipe the vertex detector (VTX) is located. It is surrounded by the silicon intermediate tracker (SIT). A time projection chamber (TPC) forms the main tracking device. A part of the forward region ($0.906 < |\cos\theta| < 0.993$) is covered by the forward tracking disks (FTD).

It is foreseen to build a multi-layered pixel micro vertex detector as VTX with an inner radius of 1.5 cm and an outer radius of 6 cm. Four different pixel options are discussed: a CCD-based detector, a CMOS option, DEPFET option and a hybrid pixel detector. Details are described in [63–66]. As an example Figure 3.8 shows a close-up view of the proposed CCD VTX design. The general performance goal is to reach a point-measurement resolution of $\sim 1\ \mu$m.

In order to improve the momentum resolution the SIT shall be mounted between the VTX and the TPC. The SIT is planned as a silicon detector and consists of two concentric cylinders with radii 36 cm and 64 cm, respectively. Extensive studies [67] showed that for its purpose a spatial resolution of 10 μm in r-ϕ and of 50 μm in z is sufficient.

In terms of momentum resolution the seven forward tracking discs will play the same role as the SIT. The first three discs (seen from the interaction point) are designed to be pixel detectors, while the last four devices are strip detectors. The resolution requirement is 25 μm.

It is intended to use a time projection chamber as the central tracking device, since its advantages of large number of measurements along a track, a minimum amount of material and the simple and efficient track reconstruction are clearly arguments in favour of a TPC.

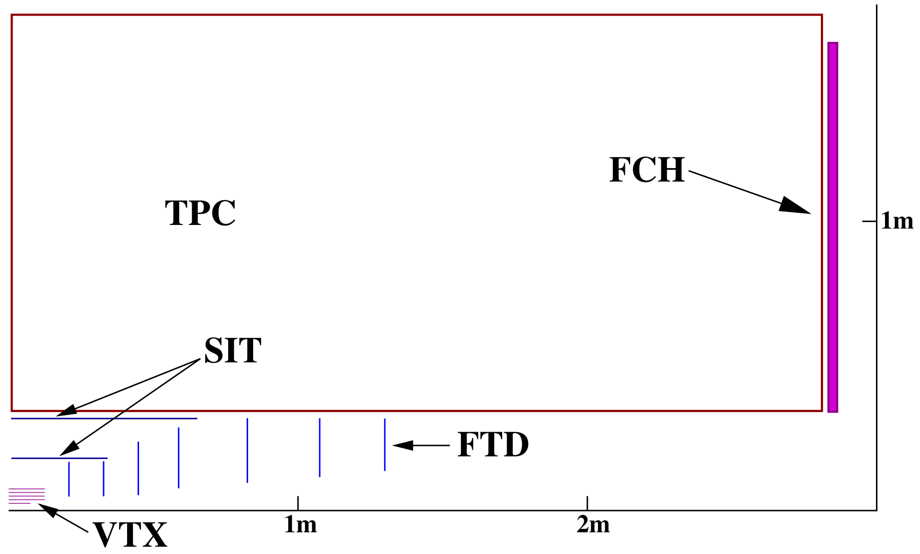

Figure 3.7: General layout of the TESLA tracking system. The labeled tracking devices are explained in the text.

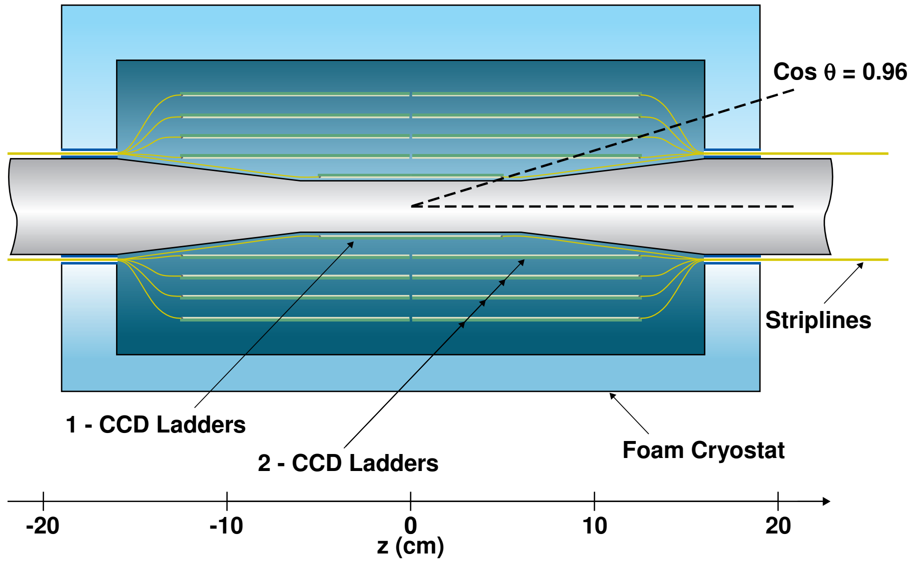

Figure 3.8: Cross-section of the proposed CCD-based vertex detector.

The mandatory performance goals of $\delta(1/p_t) < 2 \times 10^{-4}/1$ GeV (TPC only) and $\sigma(\mathrm{d}E/\mathrm{d}x) \leq 5\%$. The sensitive cylindric volume will have a length of $l = 2 \times 250$ cm, an inner radius of $r_\mathrm{i} = 36.2$ cm and an outer radius of $r_\mathrm{o} = 161.8$ cm. It is designed for a continuous operation during one TESLA train (1 ms). Systematic effects on the TPC track reconstruction have to be kept below 10 μm. Computer simulations showed that already the TPC alone will reach a momentum resolution as good as $1.5 \times 10^{-4}/1$ GeV.

Straw tubes located at both ends of the the TPC are the active volume of the forward chambers, FCH. With an additional precise track measurement at this position the FCH allow for a compensation of the degrading track reconstruction performance in forward direction.

The interplay of all tracking devices, their performance and efficiency was extensively studied. More information on this can be found in [68].

The Calorimeter System

As shown in Figure 3.6 the TESLA tracking devices are surrounded by the electro-magnetic calorimeter, ECAL, and the hadron calorimeter, HCAL. The fact that both systems are located inside the magnet coil is a big advantage compared with older detector concepts. This guarantees that the calorimeter performance will not be distorted by dead material in front of the detector components. The system will be completed by forward calorimeters (see below).

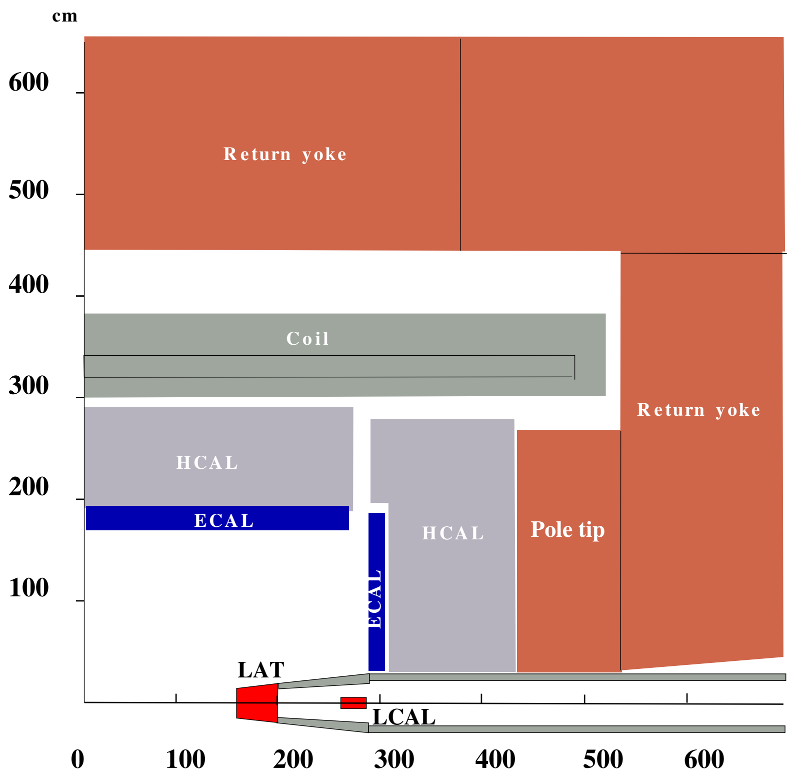

Figure 3.9: General layout of the TESLA calorimeter system.

Two options are discussed for the ECAL: One scenario is based on tungsten absorbers and silicon diode pads (the so-called SiW option). The high granularity of 32 million calorimeter channels would provide an excellent energy and spatial resolution. The alternative option is the ‘shashlik’ electro-magnetic calorimeter. The scintillation light from plastic scintillator is read out via wavelength shifting fibres. This kind of calorimeter has the advantages of easy assembly and operation and low cost. Both ways should be capable to meet the TESLA ECAL energy resolution requirement of:

$$\left.\frac{\sigma_E}{E}\right|_{\mathsf{ECAL}}^{\mathsf{TESLA}} \leq 0.01 + \frac{0.1}{\sqrt{E/1\ \mathrm{GeV}}}. \tag{3.8}$$

Also for the HCAL two options are followed. The tile hadron calorimeter option is constructed as a sampling calorimeter. It consists of alternating layers of stainless steel and scintillator as active medium. With a slightly worse energy resolution but with the advantage of lower costs compared to a sampling calorimeter a digital hadron calorimeter concept is followed as alternative approach. It is based on the fact that if the readout cells in the active layer are small enough, simply counting the fired cells would provide enough information to reconstruct the hadronic shower energy. As in the sampling calorimeter case stainless steel would be the preferred absorber material. For the detecting medium resistive plate chambers, wire chambers operated in limited Geiger mode or thin wire chambers are considered. The proposed cell size is 1 cm ^{2}. Independent from the final choice for the HCAL concept a large granularity is needed for the compensation by software weighting, for the identification and separation of neutral hadrons in jets and for muon tracking inside of the calorimeter. The energy resolution for single hadrons was found in simulation studies to be:

$$\left.\frac{\sigma_E}{E}\right|_{\mathsf{HCAL}}^{\mathsf{TESLA}} = 0.03 + \frac{0.35}{\sqrt{E/1\ \mathrm{GeV}}}. \tag{3.9}$$

The TESLA Magnet and the Muon System

The TESLA magnet has to provide a magnetic field of a least 3 T and its current design allows a magnetic field of 4 T. It is based on the design for the CMS experiment [69]. The tracking detectors as well as the electromagnetic and hadronic calorimeter are located inside the magnet while the iron yoke is used to house the muon detector. The main purposes of the muon system are the identification of muons and thus providing a trigger signal, and tail catching of hadronic showers leaking out of the HCAL. The first choice of detector technology for the TESLA muon system is based on resistive plate chambers (RPC) [70].

The Forward Region

As pointed out above the hermeticity is vitally important for the described signal selection strategy and is a crucial feature of a next generation detector. This means in terms of calorimetry an instrumentation down to the beam pipe as far as possible. For the TESLA detector this issue shall be addressed with the low angle tagger, LAT and the luminosity calorimeter, LCAL. Their position in the TESLA detector is shown in Figure 3.10. While they are designed on one hand for particle detection they serve at the same time as particle shields. The LAT and LCAL design was driven by the special beam-induced background environment at TESLA, a subject which will be discussed in more detail in Chapter 5.

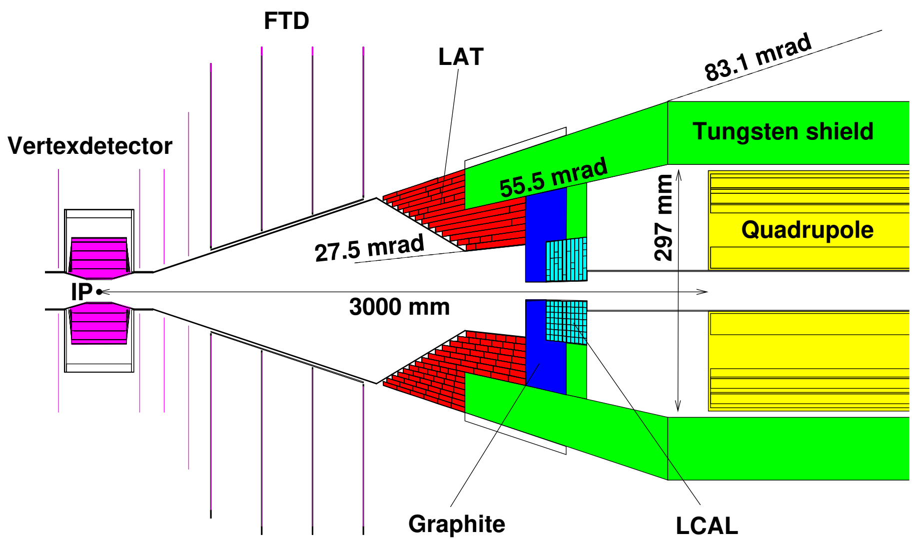

Figure 3.10: TESLA forward region. The LAT and LCAL are discussed in the text.

The LAT extends the electro-magnetic calorimeter down to a polar angle of 27.5 mrad. It is foreseen that it is build as a sampling calorimeter with tungsten as absorber (2.6 mm thickness) and silicon (0.5 mm thickness) as active material. In simulations an energy resolution of

$$\left.\frac{\sigma_E}{E}\right|_{\mathrm{LAT}}^{\mathrm{TESLA}} = \frac{0.25}{\sqrt{E/1\,\mathrm{GeV}}}. \tag{3.10}$$

was found.

At very small polar angles (4.6 - 28 mrad) the LCAL is located. It will mainly serve as a fast luminosity monitor and will measure the amount of beam-induced background (see chapter 5). The measured signal is very sensitive to luminosity variations within one bunch train and will be fed back to the beam delivery system to tune the beam. To accomplish this task, a statistical error on the energy measurement of less than 1% and a response time of 30-50 ns will be needed [71]. The LCAL will be a sampling calorimeter with a layer structure similar to the LAT. Both silicon and diamond sensors are considered for the active layers.

3.3 The Event and Detector Simulation

Accelerators and detectors provide the physicists with experimental data. The interpretation of this data requires a comparison with theoretical predictions. The theoretical input is represented by computer simulations which first mimic the production of physics events in e^+e^- collisions followed by simulations of the detector components and their response to the generated events.

This Section gives a short overview on the physics processes which are important for this analysis, the event generation and detector simulation.

3.3.1 Physics Processes at LEP and TESLA

At centre-of-mass energies well above the Z-resonance the following processes are the most important SM processes in e^+e^- collisions.

Two-Photon Processes

The term two-photon process is used for reactions of type $e^+e^- \to e^+e^-f\bar{f}$ which proceed via the exchange of two photons. The graph in Figure 3.11 illustrates this kind of events.

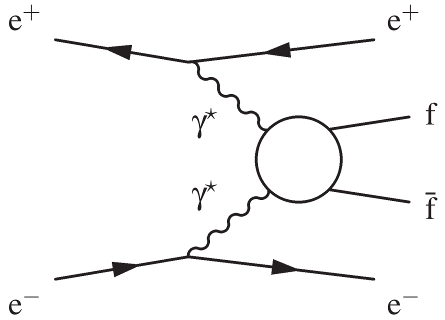

Figure 3.11: A diagram of the reaction $e^+e^- \to e^+e^-f\bar{f}$, proceeding via the exchange of two photons.

As discussed in Chapter 2 two-photon processes play a very crucial role in terms of background for this analysis. The spectrum of two-photon processes is manifold. A first rough categorisation is based on the photons' virtuality, Q^2, which is defined as the negative squared four-momentum: $Q^2 = -q^2 = -(E^2 - \vec{p}^2)$. The photons are called quasi-real if the Q^2 is small. In this case the corresponding electron transfers only a small transverse momentum to the photon and the electron disappears in the beam pipe. With increasing virtuality the beam electrons carry a larger transverse momentum and eventually will be deflected into the detector. Depending on the number of beam electrons visible in the detector the two-photon events are called un-tagged, single-tagged or double-tagged.

Due to the Heisenberg Uncertainty Principle a photon is allowed to fluctuate into a charged fermion anti-fermion system. Table 3.2 summarises the different appearances of a photon. The two-photon vertex in Figure 3.11 indicates that a more detailed event classification according to the photon structure can be chosen.

The direct or bare photon takes part in the interaction as a whole. The photon is called resolved if it fluctuates into a hadronic state which interacts subsequently. A distinction is drawn between the perturbatively calculable splitting into a pair of quarks (point-like) and the fluctuation into a hadronic state with the same quantum numbers (hadron-like).

The two-photon cross-section is as large as $O(10\,\text{nb})$ at $\sqrt{s} = 200$ GeV in case of un-tagged hadron-like processes. The cross-section rises logarithmically with the centre-of-mass energy. An elaborate review on the nature of the photon can be found in [72].

direct	**resolved**	
γ	$\gamma \rightarrow \mathrm{f\bar{f}}$	$\gamma \rightarrow V(J^{CP} = 1^{--})$
bare	point-like	hadron-like

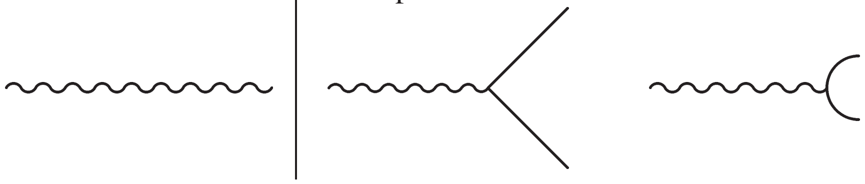

Table 3.2: The different appearances of the photon.

Four-Fermion Processes

Four-fermion process pool all kind of electro-weak processes (excluding the two-photon processes) with four fermions in the final state. The Feynman-diagrams of the most important four fermion processes are shown in Figure 3.12. Four-fermion final states are produced by W and Z pair-production, single W and single Z production in Compton scattering of quasi-real photons. The cross-sections are are of order 50 pb at centre-of-mass energies of $\sqrt{s} = 200$ GeV.

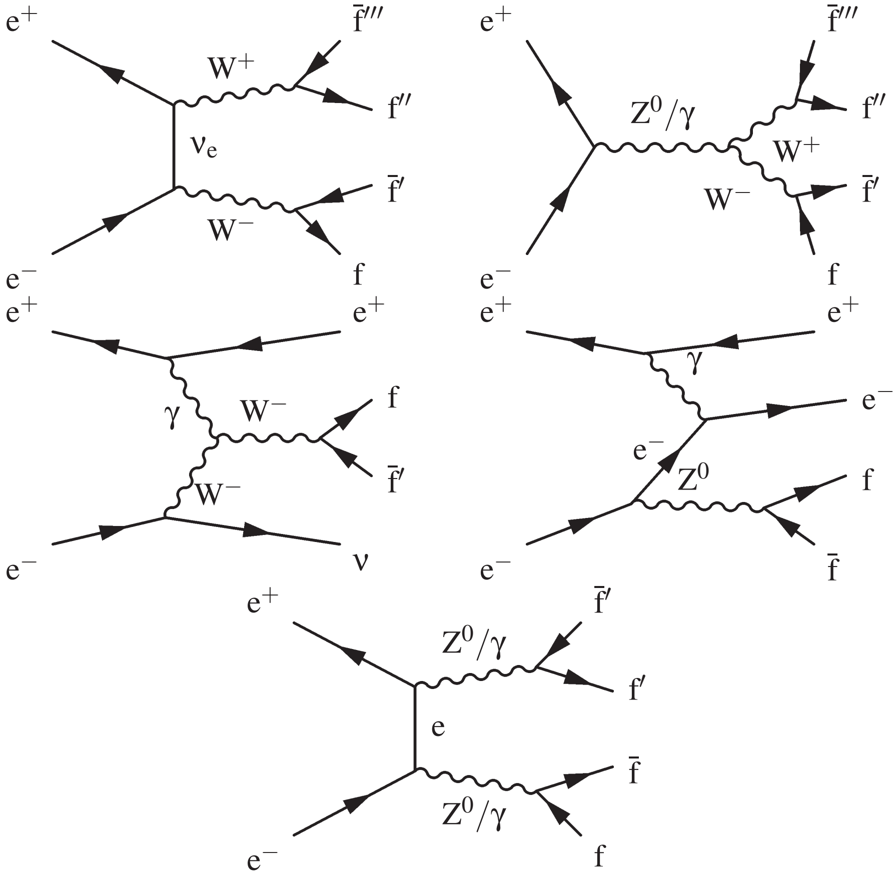

Figure 3.12: Feynman-diagrams of the most important four fermion processes: W pair production, single gauge boson production, pair production of neutral gauge bosons.

Two-Fermion Processes

The annihilation of an e^+e^- pair into a neutral gauge boson (γ or Z) and the subsequent decay of the boson into a fermion-anti-fermion pair is the so-called two-fermion process (see Figure 3.13). The production cross-section for these events reaches a maximum at the Z-pole and drops with increasing centre-of-mass energy as $1/s$ for $\sqrt{s} \gg M_Z$.

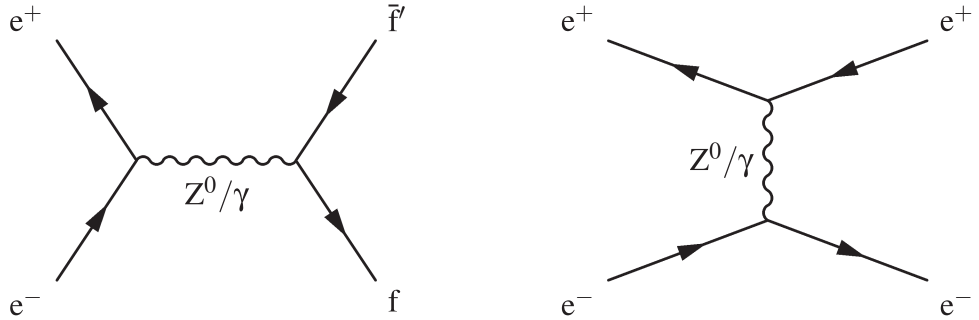

Figure 3.13: Feynman-diagrams of the s- and t-channel two fermion processes.

Two-photon Production

The process $e^+e^- \rightarrow \gamma\gamma(\gamma)$, the production of two photons via an e^+e^- annihilation, shall only be mentioned for sake of completeness. The Feynman diagram is depicted in Figure 3.14.

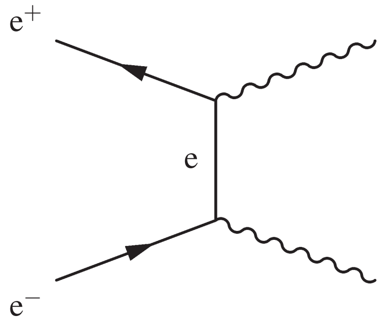

Figure 3.14: Production of two photons via e^+e^- annihilation.

3.3.2 The Event Simulation

The simulation of the signal process and all possible SM processes (background) is needed for the specification of signal selection criteria. Signal properties are used as filter criteria aiming for both a high signal purity and large signal detection efficiency. The signal detection or a possible discovery is then based on the comparison of the number of expected (simulated) background events and the number of candidates selected in the data sample. The complete event simulation contains two steps, namely the event generation and the detector simulation.

The Event Generation

Event generators are computer programs which produce the four-vectors of all participating particles of a selected physics process. The event topology is reproduced according to the differential event cross-section. Typically, specialised generators are used for a class of background and signal process. In case of quarks in the final state these have to be passed through an additional program simulating the fragmentation process. The event generation finishes with a list of four-vectors of all final state particles. The following list of event generators was used for this analysis.

- Chargino Production
  The SUSYGEN [73] generator was used to simulate the signal events. It is a Monte Carlo event generator for supersymmetric particle production within the MSSM, the minimal supergravity framework, and the gauge mediated supersymmetry breaking framework, with or without assuming R_{P} conservation.
  The chargino decay width implemented in SUSYGEN was modified for $\Delta M \lesssim 1.5$ GeV. The $\tilde{\chi}_1^{\pm} \to q\bar{q}'\tilde{\chi}_1^0$ decay mode was partly replaced by new hadronic chargino decay channels ($\tilde{\chi}_1^- \to \pi^-\tilde{\chi}_1^0$, $\tilde{\chi}_1^- \to \pi^-\pi^0\tilde{\chi}_1^0$ and $\tilde{\chi}_1^- \to \pi^-\pi^-\pi^+\tilde{\chi}_1^0$) reflecting analytical calculations described in [33, 74]. The hadronic $\tilde{\chi}_1^{\pm}$ decays are modelled using these channels as long as the sum of their partial widths is larger than the width of the tree level $\tilde{\chi}_1^{\pm} \to q\bar{q}'\tilde{\chi}_1^0$ decay. The $\tilde{\chi}_1^{\pm} \to q\bar{q}'\tilde{\chi}_1^0$ decay mode dominates for $\Delta M \gtrsim 1.5$ GeV. The chargino branching ratios are depicted in Figure 3.15. In SUSYGEN initial state corrections are incorporated using a factorised "radiator formula" (REMT by Kleiss [75]) where exponentiation of higher orders and the transverse momentum distribution of the photon have been implemented.
  While SUSYGEN is able to handle the most common SUSY breaking scenarios, a package for calculating AMSB spectra is not implemented. For this purpose the ISAJET generator [76] was used.

- Two-Photon Processes
  PHOJET [77], HERWIG [78] and VERMASEREN [79] were used to simulate two-photon collisions resulting in electron pair or hadronic final states. None of these Monte Carlo generators include QED radiative corrections. The generator of Berends, Darverveldt and Kleiss (BDK) [80] is able to handle these corrections to order $O(\alpha)$. The program was written to simulate $e^+e^- \to e^+e^-\gamma^*\gamma^*(\gamma) \to e^+e^-\mu^+\mu^-(\gamma)$ events. For this analysis BDK was modified to allow the generation of τ final states.

- Four-Fermion Processes
  KORALW [81] and grc4f [82] were used to generate four-fermion events. The latter was used for all four-fermion final states involving e^+e^- pairs. Both KORALW and grc4f simulate ISR, but only the KORALW samples include ISR photons with transverse momentum.

- Two-Fermion Processes
  KK2F [83] was used to simulate $\tau^+\tau^-(\gamma)$, $\mu^+\mu^-(\gamma)$ and the multi-hadronic final states $q\bar{q}(g\gamma)$. NUNUGPV [84] was used to generate $\nu\bar{\nu}(\gamma)$ events. TEEGG [85] and BHWIDE [86] were used to simulate $e^+e^-(\gamma)$ events.

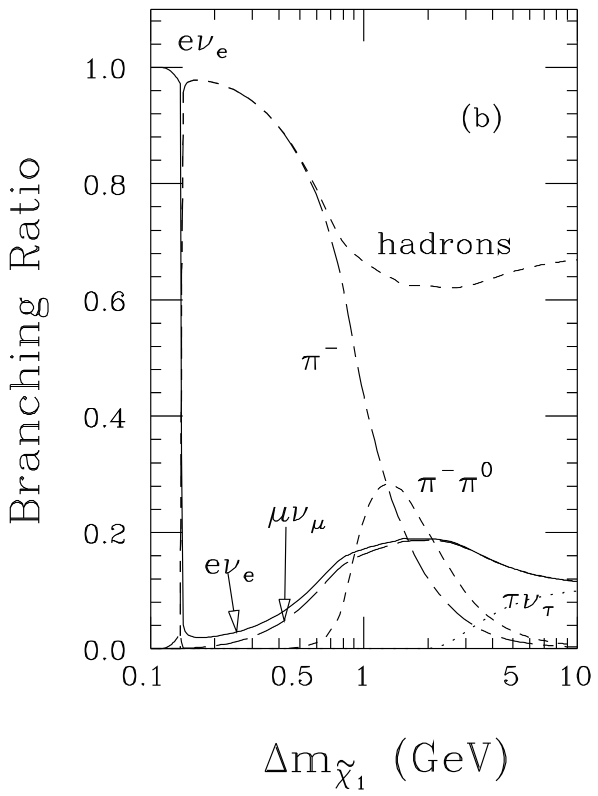

Figure 3.15: Chargino branching ratios as a function of the mass difference as calculated in [33]. In the modified SUSYGEN version the hadronic $\tilde{\chi}_1^{\pm}$ decays are modelled using the decay channels via pions as long as the sum of their partial widths is larger than the width of the tree level $\tilde{\chi}_1^{\pm} \rightarrow q\overline{q}'\tilde{\chi}_1^0$ decay.

- Others
  RADCOR [87] was used to simulate photon pair final states.

A summary of all considered physics processes, their generators and the size of the generated data samples used for the OPAL analysis is given in Table 3.3.

Simulation of Beam-Beam Interactions

The special beam conditions at a Linear Collider require a particular attention. As it will be described in detail in Chapter 5 beam-induced background at Linear Colliders has a severe impact on the detector design. The simulation of beam-induced background was done with the Guinea-Pig package [88], a program which simulates the process of two colliding bunches. For this purpose the bunch particles are represented by typically 20000 – 50000 so-called macro particles. The bunches themselves are cut into a three-dimensional grid and the macro particles are distributed over this grid according to the charge distribution within one bunch. Then the program performs all calculations needed to simulate the dynamics of a bunch collision.

final state	generator	σ ($\sqrt{s}$=208 GeV) [pb]	$\int \mathcal{L}\,dt$ [pb^{-1}]	ISR	comment
two-photon processes					
$e^+e^-q\bar{q}$	PHOJET	11 170	909	only collinear	un-tagged
$e^+e^-q\bar{q}$	HERWIG	328	3 994	only collinear	single-tagged
$e^+e^-q\bar{q}$	PHOJET	3.3	2 262	only collinear	double-tagged
$e^+e^-e^+e^-$	VERMASEREN	876	3 964	only collinear	
$e^+e^-\mu^+\mu^-$	BDK	619	10 713	$\surd$	
$e^+e^-\tau^+\tau^-$	BDK	469	24 111	$\surd$	
four-fermion processes					
$\ell\bar{\ell}\ell'\bar{\ell}'$	KORALW	3.4	106 003	$\surd$	$\ell = \mu, \tau$
$\ell\bar{\ell}q\bar{q}$	KORALW	9.4	106 001	$\surd$	$\ell = \mu, \tau$
$q\bar{q}q'\bar{q}'$	KORALW	9.1	101 001	$\surd$	
$e^+e^-e^+e^-$	grc4f	17	40 000	only collinear	
$e^+e^-\mu^+\mu^-$	grc4f	12	40 000	only collinear	
$e^+e^-\tau^+\tau^-$	grc4f	1.7	40 000	only collinear	
$e^+e^-q\bar{q}$	grc4f	38	35 000	only collinear	
two-fermion processes					
$q\bar{q}(\gamma)$	KK2f	78	34 459	$\surd$	
$e^+e^-(\gamma)$	TEEGG	638	3 368	$\surd$	t-channel
$e^+e^-(\gamma)$	BHWIDE	493	5 976	$\surd$	s-channel
$\mu^+\mu^-(\gamma)$	KK2f	6.8	88 206	$\surd$	
$\tau^+\tau^-(\gamma)$	KK2f	6.6	90 716	$\surd$	
$\nu\bar{\nu}(\gamma)$	NUNUGPV	7.9	69 077	$\surd$	
others					
$\gamma\gamma(\gamma)$	RADCOR	20	17 739	$\surd$	

Table 3.3: Summary of all SM background Monte Carlo samples used for the OPAL analysis.

The Detector Simulation

The detector response to the generated events is modelled with detector simulations. In these programs are the detector geometry and the properties of all active and passive detector components implemented. Based on the four-momenta produced with the event generators detector simulations calculate the reactions of these particles with the material of the detector components like ionisation loss of charged particles, shower evolution in the detector material and multiple scattering of particles.

The OPAL detector was simulated with GOPAL [89], a program based on the GEANT3 [90] package. Both data and Monte Carlo events were reconstructed with the ROPE [91] program. The GEANT3 package was also used for the TESLA detector simulation BRAHMS [92], a program which also handles the event reconstruction. In addition, a parameterised[7] fast Monte Carlo detector simulation, SIMDET [93] was used.

[7] The parametrisation is based on BRAHMS simulations.

Chapter 4

The OPAL Analysis

The OPAL analysis is structured in four parts which are described in the following sections. The first part describes the event selection while the second part deals with the identification and treatment of systematic uncertainties. The results and the interpretation of the results will be presented in the third part. A discussion of the results follows in the last part.

4.1 The Event Selection

4.1.1 The Analysed Data Sample

The data analysed in this note were taken in 1998, 1999 and 2000 at centre-of-mass energies, $\sqrt{s}$, between 188 and 209 GeV. The growth of the integrated luminosity during the periods of data taking is illustrated in Figure 4.1. The search is based on a total of 569.9 pb^{-1} of data for which all relevant detector components were fully operational. The luminosity weighted mean centre-of-mass energy and the integrated luminosity of each energy bin is listed in Table 4.1.

year	$\sqrt{s}$ bin range [GeV]	$\langle\sqrt{s}\rangle$ [GeV]	$\int \mathcal{L}dt$ [pb^{-1}]
1998	188.0 – 190.5	188.6	167.6
1999	190.5 – 194.0	191.6	27.7
1999	194.0 – 199.0	195.5	71.2
1999	199.0 – 201.0	199.5	72.1
1999	201.0 – 202.5	201.6	33.9
2000	203.5 – 204.5	204.0	7.7
2000	204.5 – 205.5	205.2	64.9
2000	205.5 – 206.5	206.3	58.6
2000	206.5 – 207.5	206.7	58.9
2000	>207.5	208.1	7.3
			569.9

Table 4.1: The luminosity weighted mean centre-of-mass energy and integrated luminosity of each energy bin.

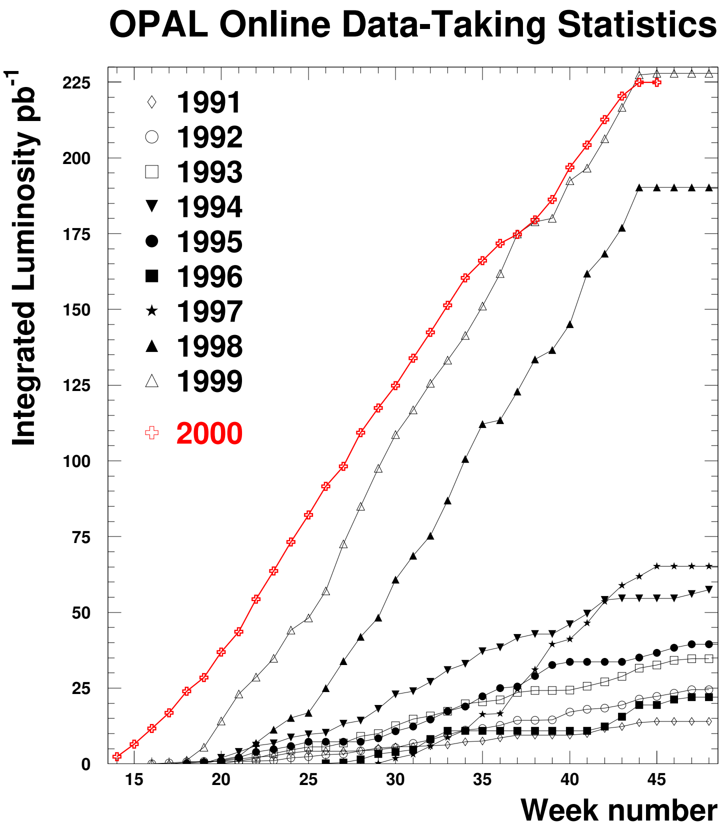

Figure 4.1: Integrated luminosity collected in the course of the data taking period for all years of OPAL running.

4.1.2 The Generated Signal Samples

The generated chargino masses $M_{\tilde{\chi}_1^\pm}$ ranged from 45 GeV to 97.5 GeV. The step size was 5 GeV for $M_{\tilde{\chi}_1^\pm} \leq 80\,\text{GeV}$. Above this mass and therefore closer to the kinematic limit, the step size was reduced to 2.5 GeV. The simulated mass differences were ΔM =0.17, 0.2, 0.3, 0.4, 0.5, 1.0, 1.5, 2.0, 3.0, 4.0 and 5.0 GeV. The points were chosen to give a $(M_{\tilde{\chi}_1^\pm}, \Delta M)$ grid covering all points at which a reasonable signal efficiency was expected[1], also taking into account existing chargino mass limits from LEP I. A total of 500 signal events were generated for each grid point at $\sqrt{s}$ =189, 192, 196, 200, 202, 204, 205, 206, 207 and 208 GeV, and for both the higgsino-like and gaugino-like scenarios, in view of their different ISR spectra. The signal events were required to be accompanied by one ISR photon within the ECAL acceptance $|\cos\theta| < 0.984$. The transverse momentum of the ISR photon was required to be larger than $0.025\sqrt{s}$.

[1]Chargino lifetime effects, which play a significant role in most SUSY scenarios in the very small ΔM region ($\Delta M < 0.5\,\text{GeV}$), were not taken into account. This region is included in the experimental results but is not used for the theoretical interpretation due to the theoretical uncertainties.

4.1.3 The Event Reconstruction

In order to choose the optimal event selection criteria which are based on event properties the events have to be reconstructed from the information provided by the detector components. In a first step tracks are reconstructed from the output of the tracking devices and calorimeter clusters are build from the ECAL and HCAL responses. The second step puts tracks and clusters together to form the event. In order to avoid energy double counting an energy flow algorithm [94] is applied. The algorithm tries to match reconstructed tracks and calorimeter clusters, the energy objects. Clusters without matching tracks (unassociated clusters) are treated as originating from neutral massless particles. In case of associated clusters the expected deposited energy is calculated from the track momenta and the tracks' polar angles. If the expected energy exceeds the measured energy the cluster is discarded and the track is treated as originating from a charged particle with the pion mass assigned to it. Should the measured energy exceed the expected energy the energy difference is assumed to deposited by an additional photon. The energy flow algorithm is part of the ROPE [91] package. This procedure results in a set of reconstructed objects which are called particles in the following. All Monte Carlo samples were, after being processed through the OPAL detector simulation, reconstructed in the same way as the data.

4.1.4 Photon Identification

As described in Chapter 2 the analysis is based on the selection of events accompanied by ISR photons. The assignment of unassociated clusters to photons is not sufficient for this analysis. A dedicated identification algorithm is needed which efficiently separates photons coming directly from the interaction region from photons coming from subsequent decays (like $\pi^0 \to \gamma\gamma$) or electromagnetic showers originating from electrons. Photon candidates have to fulfil the following criteria:

A photon candidate was defined by an ECAL cluster including at least two lead-glass blocks. It was required that the ECAL cluster was unassociated, that is to say no reconstructed track from a charged particle lies within the angular resolution of the cluster when extrapolated to the calorimeter. Furthermore, the energy of additional tracks and clusters in a 15° half-angle cone defined by the photon direction had to be less than 2 GeV. The photon candidate was accepted only in an angular region of $|\cos\theta| < 0.976$. If several photon candidates were found they were ordered according to their energy beginning with the highest energy.

Photons undergoing a photon conversion were not considered.

4.1.5 The Selection Criteria

The selection is a sequence of requirements which the events have to fulfil. The sequence is divided in four parts: the pre-selection, the two-photon veto, the cleaning cuts and the final selection.

The Pre-selection

Events were selected if a photon candidate as defined in Section 4.1.4 was found in the ECAL. The photon transverse energy had to be larger than 5 GeV. In order to reduce the background, the reduced visible energy, E_{vis}, defined as the difference between total visible energy and the photon candidate energy, E^{γ}, was required to be less than $0.35\sqrt{s}$. High-multiplicity events were rejected by requiring that the number of tracks passing the track quality cuts [95], excluding tracks which had been assigned to a photon conversion, had to be at least two and at most ten. In addition beam-gas and beam-wall interactions and cosmic background were rejected by a veto described in [96] using ECAL cluster shapes, information from the time-of-flight system, the tile end-cap scintillators, the muon chambers and the hadronic calorimeter. After this rather loose pre-selection all events had to pass the veto on two-photon events (V), a more refined cleaning selection (C), and a final selection (F). If more than one photon candidate was found in one event the chain of cuts was repeated for each photon separately. For at least one photon candidate the event had to pass all cuts in order to get selected.

The Two-photon Veto

Events were vetoed if there was additional energy deposited in the detector from a final state electron ("two-photon veto").

V1 The photon candidate had to pass the E_{T}^{γ} requirement Equation (2.9). With a minimal accessible electron polar angle of $\theta_{\mathrm{D}}^{\mathrm{min}} = 33\,\mathrm{mrad}$ (see Section 3.2.1) the transverse photon energy was required to satisfy $E_{\mathrm{T}}^{\gamma} \geqslant 0.0319\sqrt{s}$.

V2 The sum of energies, E_{fwd}, detected in the forward detectors SiW, FD, GC on either side had to be smaller than 5 GeV.

Figure 4.2 (a) and Figure 4.2 (b) show the distributions of E_{T}^{γ} and E_{fwd}. Apparently the agreement between data and Monte Carlo is rather poor. But this is not unexpected since some of the Monte Carlo samples do not include a proper ISR description, if any (see Table 3.3). As indicated in Figure 4.2 (c) the worst disagreement occurs in the region of low visible masses M_{vis} which suggests that mainly the two-photon and some of four-fermion samples are responsible for the incompatibility.

Among the used two-photon event generators (see Section 3.3.2) only BDK calculates the emission of ISR. Since BDK includes only the QED coupling of photons, it cannot be used to describe all features of two-photon processes, e.g. the hadron-like structure of photons. Therefore no attempt was made to fully model the background from radiative hadronic two-photon events. However, BDK was used to verify that the veto on these events operates efficiently. The veto cuts (see Section 4.1.5) depend predominantly on the characteristics of the ISR photon and the beam electrons and not on the properties of the two-photon system. While for the τ samples no cuts were applied at generator level, in the case of the μ samples an event was accepted if it satisfied one of the following three requirements: it contained at least one particle with $|\cos\theta| < 0.975$ and a transverse momentum (with respect to the beam axis) larger than 4.0 GeV or it contained two particles with $|\cos\theta| < 0.975$ and the total missing transverse momentum (with respect to the beam axis) of the event was larger than 1.0 GeV or it contained more than two particles with $|\cos\theta| < 0.975$.

Less than 0.1% of all generated BDK events pass the two-photon veto.

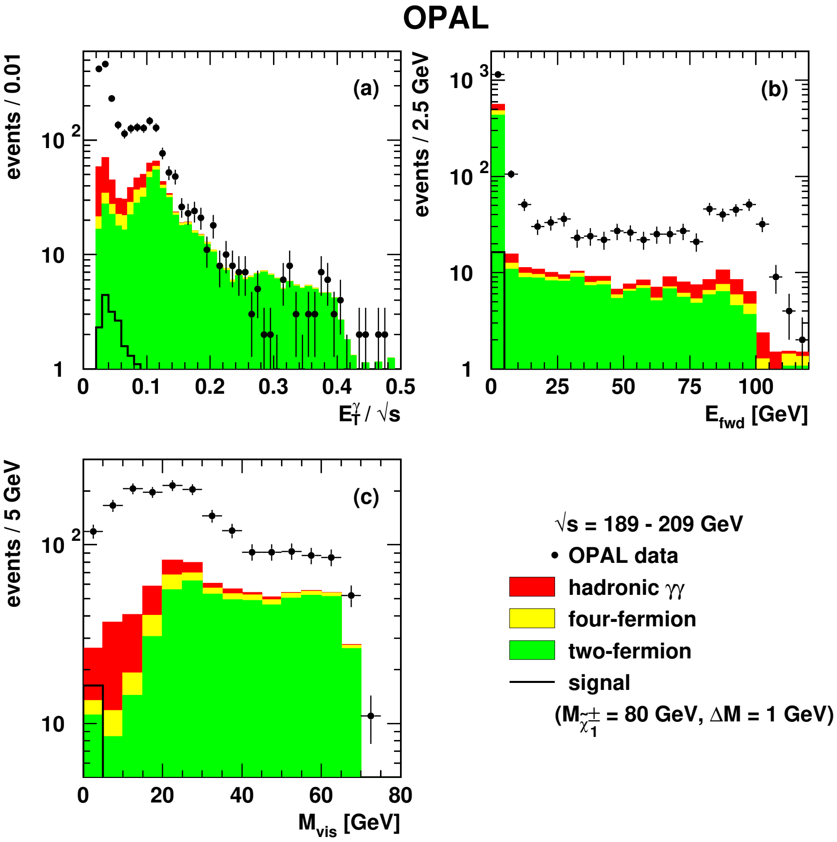

Figure 4.2: Two-photon veto variables ((a) and (b)) and distribution of the visible mass, M_{vis} (c). The OPAL data are indicated by points with error bars (statistical error) and the background distributions by the histograms. Signal distributions are plotted as black lines and correspond to a gaugino-like chargino with $M_{\tilde{\chi}^\pm_1}$= 80 GeV and ΔM =1 GeV. The accumulated events for $\sqrt{s}$ =189 – 209 GeV are shown. Each plot shows the distribution after the pre-selection.

Cleaning Cuts

After the pre-selection and the two-photon veto, the remaining events in the background sample are mainly hadronic two-photon events with a faked or misinterpreted ISR photon, or from two-fermion events. Figure 4.3 shows the distributions of the variables used for the cleaning cuts against this background. Besides others, the cut variables use the following event properties: The total transverse momentum, P_{T}, is the component of the total momentum, P, (including the ISR candidate) transverse to the beam axis. The transverse visible energy, E_{T}, was calculated by summing up the absolute transverse momenta (with respect to the beam axis) of all reconstructed particles.

The cleaning cuts were defined as:

C1 The total transverse momentum, P_{T}, should large in case of signal events due to the escaping neutralinos, whereas two-photon events are balanced and $P_{\text{T}} \approx 0$ GeV. Most of the events from hadronic two-photon processes and two-fermion events were removed by demanding that the ratio of the total transverse momentum to the transverse energy $P_{\mathrm{T}}/E_{\mathrm{T}}$ is larger than 0.4.

C2 A further reduction of the hadronic two-photon background was achieved by requiring that the ratio of the total transverse momentum to the total momentum P_{T}/P is larger than 0.2.

C3 The definition of a photon candidate was further restricted with the following cuts. The relative error on the energy of the photon had to be less than 30%. The error on the ECAL cluster energy was derived by the assumption that the cluster originates from a pure electromagnetic shower [94]. In addition the angle between the photon candidate and any track or ECAL cluster was required to be larger then 25°.

As shown in Figure 4.3 the agreement between data and Monte Carlo is still poor, but improves from cut to cut. The disagreement is expected due to the unmodelled ISR spectrum in most of the Monte Carlo samples and the uncertainty on the two-photon cross-sections. However, the largest disagreement lies outside the accepted regions.

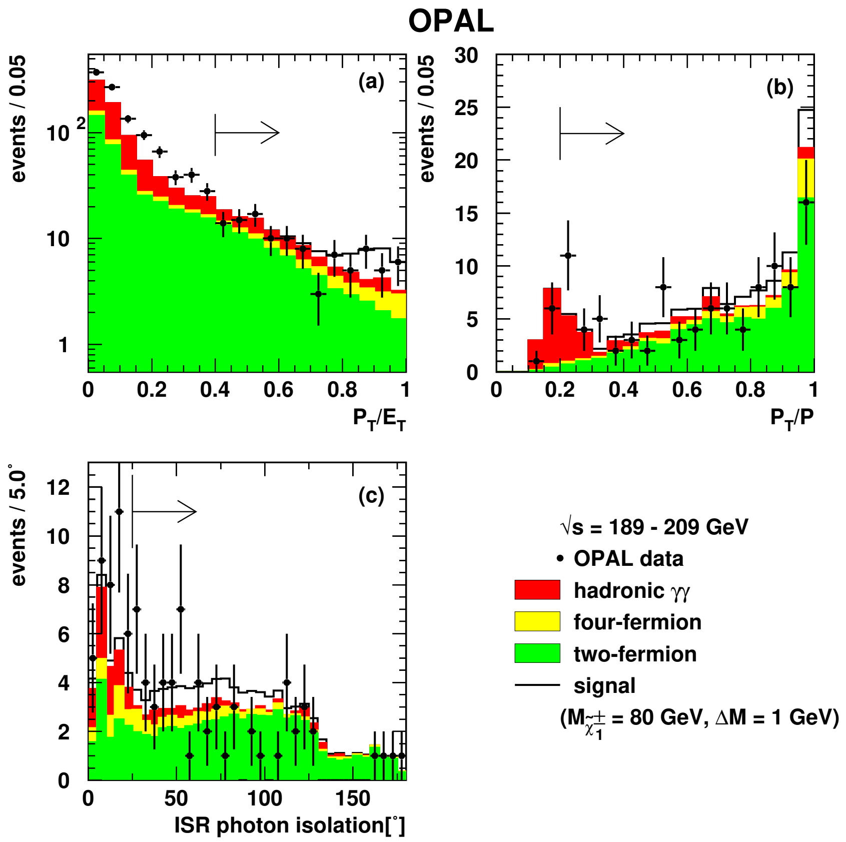

Figure 4.3: Cleaning cut variables. The OPAL data are indicated by points with error bars (statistical error) and the background distributions by the histograms. Signal distributions are plotted as black lines (added to the expected background) and correspond to a gaugino-like chargino with $M_{\tilde{\chi}_1^\pm}$ = 80 GeV and ΔM =1 GeV. The accumulated events for $\sqrt{s}$ =189 – 209 GeV are shown. Each plot shows the distribution after the cuts on the preceding variables. The arrows indicate the accepted regions.

The Final Selection

To optimise the signal to background ratio, the final two cuts are a function of the point in the $(M_{\tilde{\chi}_1^\pm}, \Delta M)$ space which is being tested.

F1 The ISR photon candidate recoil mass is defined as

$$M^2_{\mathrm{rec}} = s - 2\sqrt{s}E^{\gamma}. \tag{4.1}$$

The recoil mass should be at least twice the tested chargino mass $M_{\tilde{\chi}_1^\pm}$. Taking resolution effects into account the cut on the recoil mass was set to $2 \times M_{\tilde{\chi}_1^\pm} - 2.5\,\mathrm{GeV}$.

F2 The visible energy E_{vis} depends to first order on the tested mass difference ΔM. In order to retain the maximum signal efficiency, E_{vis} was required to be smaller than $4 \times \Delta M$.

The recoil mass distribution after cut C3 and the visible energy distribution after cut F1 are shown in Figure 4.4. The agreement between data and Monte Carlo distributions is reasonable.

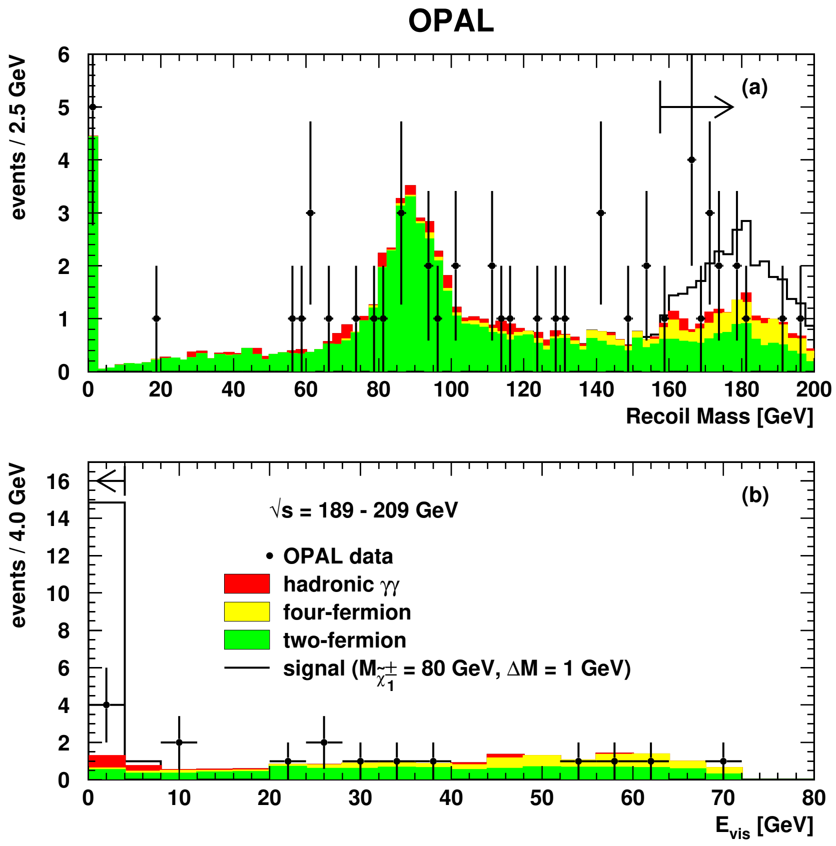

Figure 4.4: Final selection cut variables. The OPAL data are indicated by points with error bars (statistical error) and the background distributions by the histograms. Signal distributions are plotted as black lines (added to the expected background) and correspond to a gaugino-like chargino with $M_{\tilde{\chi}_1^\pm} = 80\,\mathrm{GeV}$ and $\Delta M = 1\,\mathrm{GeV}$. The accumulated events for $\sqrt{s} = 189 - 209$ GeV are shown. Each plot shows the distribution after the cuts on the preceding variables. The arrows indicate the accepted regions.

4.1.6 Selection Results

Background and Candidates

The numbers of observed events and expected background events after each cut for the full available data set ($\sqrt{s}$ =189 – 209 GeV) are summarised in Table 4.2. The disagreement between data and Monte Carlo during the pre-selection vanishes after the cut on $P_{\mathrm{T}}/E_{\mathrm{T}}$, C1. After the final cut, F2, no excess over the SM background is observed.

	two-fermion	four-fermion	two-photon	total bkg.	data	ε [%] ($M_{\tilde{\chi}_1^\pm}=80$ GeV, $\Delta M = 1$ GeV)	ε′ [%]
P	584.7 ± 8.4	69.2 ± 1.1	923.0 ± 13.5	1580 ± 16	2432	2.11 ± 0.12	59.4 ± 2.2
V1	561.0 ± 8.2	63.1 ± 1.1	607.9 ± 9.9	1235 ± 13	1881	1.73 ± 0.11	48.8 ± 2.2
V2	427.8 ± 7.3	47.4 ± 0.9	393.2 ± 8.0	870.7 ± 10.9	1150	1.73 ± 0.11	48.8 ± 2.2
C1	71.0 ± 0.9	12.9 ± 0.4	24.4 ± 1.3	108.3 ± 1.6	108	1.73 ± 0.11	48.8 ± 2.2
C2	70.6 ± 0.9	12.4 ± 0.4	14.4 ± 1.0	97.4 ± 1.4	101	1.72 ± 0.11	48.4 ± 2.2
C3	58.4 ± 0.8	8.1 ± 0.3	5.4 ± 0.6	72.0 ± 1.0	52	1.48 ± 0.10	41.6 ± 2.2
F1	9.7 ± 0.3	5.5 ± 0.3	1.5 ± 0.3	16.7 ± 0.5	16	1.45 ± 0.10	41.0 ± 2.2
F2	0.5 ± 0.1	0.09 ± 0.02	0.7 ± 0.2	1.3 ± 0.2	4	1.39 ± 0.10	39.2 ± 2.2

Table 4.2: Number of expected background events and number of candidates after each cut. The first three rows list the contributions to the expected background from fermion-pair, four-fermion and two-photon events. The hadronic two-photon events passing the two-photon veto are those produced with generators without QED radiative corrections. The last two columns show as an example the absolute signal efficiency (number of selected signal events normalised to the number of generated events), ε, and relative efficiency (number of selected signal events normalised to a subset of generated events with $E_{\mathrm{T}}^{\gamma} > 0.025\sqrt{s}$ and $|\cos\theta^{\gamma}| < 0.985$), ε′, at $\sqrt{s} = 208$ GeV for $M_{\tilde{\chi}_1^\pm} = 80$ GeV and $\Delta M = 1$ GeV in case of the chargino-like scenario. The errors are statistical. All numbers correspond to the full analysed data set (569.9 pb^{-1}). For the final cuts F1 and F2 a chargino mass of $M_{\tilde{\chi}_1^\pm} = 80$ GeV and a mass difference of $\Delta M = 1$ GeV were assumed.

A breakdown of numbers of candidates and expected background events according to the centre-of-mass energy can be found in Table 4.3.

The numbers of candidates and expected events after the final cut F2 for a selection of ($M_{\tilde{\chi}_1^\pm}$, ΔM) grid points are listed in Table 4.4. The distribution of candidates and expected events in the ($M_{\tilde{\chi}_1^\pm}$, ΔM) plane is illustrated in Figure 4.5. The most candidates, 11, were observed at ($M_{\tilde{\chi}_1^\pm}$, ΔM) = (45.0 GeV, 5.0 GeV) whereas 12.0 ± 0.6 background events were expected. The number of candidates as well as the number of expected background events decreases with both increasing chargino mass and decreasing mass difference. At ($M_{\tilde{\chi}_1^\pm}$, ΔM) = (80.0 GeV, 1.0 GeV) 1.3 ± 0.2 background events were expected while 4 candidate events were observed.

	189 GeV		192 GeV		196 GeV		200 GeV		202 GeV	
P	446.8 ± 10.7	707	77.9 ± 2.4	128	234.0 ± 6.3	319	217.4 ± 4.8	306	100.5 ± 2.8	146
V1	371.4 ± 8.9	584	66.3 ± 2.2	107	177.6 ± 4.6	236	168.7 ± 4.0	231	77.2 ± 2.3	111
V2	262.5 ± 7.6	358	46.5 ± 1.9	58	123.5 ± 3.9	157	116.2 ± 3.3	149	52.6 ± 1.9	65
C1	32.5 ± 1.2	38	6.1 ± 0.2	5	13.7 ± 0.5	22	14.8 ± 0.5	8	6.8 ± 0.3	8
C2	29.2 ± 1.0	33	5.4 ± 0.2	5	12.9 ± 0.5	21	13.2 ± 0.4	8	5.9 ± 0.2	7
C3	20.3 ± 0.7	22	4.1 ± 0.2	3	9.6 ± 0.3	8	10.2 ± 0.3	3	4.5 ± 0.2	4
F1	4.2 ± 0.3	8	0.8 ± 0.1	0	2.0 ± 0.1	4	2.1 ± 0.1	1	1.0 ± 0.1	1
F2	0.5 ± 0.2	2	0.09 ± 0.04	0	0.07 ± 0.02	1	0.07 ± 0.02	1	0.03 ± 0.01	0

	204 GeV		205 GeV		206 GeV		207 GeV		208 GeV	
P	20.5 ± 0.6	33	158.4 ± 4.7	275	164.6 ± 4.4	237	140.2 ± 4.5	252	19.8 ± 0.6	29
V1	15.4 ± 0.4	24	117.9 ± 3.7	207	125.4 ± 3.5	176	101.1 ± 3.6	186	14.7 ± 0.5	19
V2	10.8 ± 0.4	18	86.4 ± 3.1	117	88.8 ± 3.0	101	73.2 ± 3.0	115	10.3 ± 0.4	12
C1	1.2 ± 0.06	1	11.5 ± 0.5	9	11.5 ± 0.4	5	9.0 ± 0.4	11	1.2 ± 0.06	1
C2	1.1 ± 0.05	1	10.5 ± 0.5	9	10.1 ± 0.3	5	8.1 ± 0.3	11	1.1 ± 0.05	1
C3	0.8 ± 0.04	1	7.5 ± 0.4	6	8.0 ± 0.3	1	6.3 ± 0.3	4	0.7 ± 0.03	0
F1	0.16 ± 0.02	0	2.5 ± 0.3	2	2.0 ± 0.2	0	1.6 ± 0.1	0	0.19 ± 0.02	0
F2	<0.01	0	0.11 ± 0.05	0	0.12 ± 0.06	0	0.18 ± 0.08	0	0.02 ± 0.01	0

Table 4.3: Number of expected background events and number of candidates after each cut. The ten rows correspond to the data samples at the studied centre-of-mass energies. For the final cuts F1 and F2 a chargino mass of $M_{\tilde{\chi}_1^\pm} = 80$ GeV and a mass difference of $\Delta M = 1$ GeV were assumed.

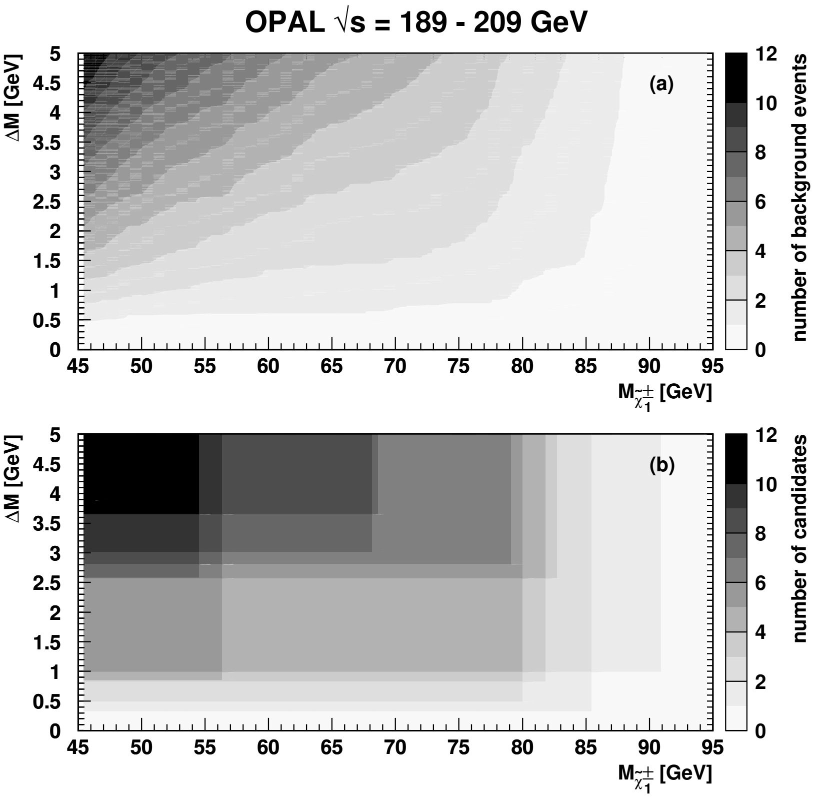

Figure 4.5: Number of expected background events (a) and number of candidates (b) passing the final selection cuts. The accumulated events for $\sqrt{s}=189-209$ GeV are shown.

$M_{\tilde{\chi}_1^\pm}$ [GeV]	ΔM [GeV]	total bkg.	data
45	5	12.0 ± 0.6	11
50	4	7.3 ± 0.5	10
60	3	4.1 ± 0.4	6
70	2	2.4 ± 0.3	4
80	1	1.3 ± 0.2	4
90	0.5	0.2 ± 0.1	1

Table 4.4: Number of expected background events and number of candidates after the final cut F2 for a selection of ($M_{\tilde{\chi}_1^\pm}$, ΔM) points. The errors are statistical. All numbers correspond to the full analysed data set (569.9 pb^{-1}).

Signal Efficiencies

To obtain the efficiencies for arbitrary masses and mass differences the derived efficiencies at the ($M_{\tilde{\chi}_1^\pm}$, ΔM) grid points were interpolated by a spline fit. The resulting signal efficiencies for the gaugino-like and the higgsino-like scenario at two different centre-of-mass energies are shown in Figure 4.6.

As an example, Figures 4.7 (a) and (b) show the signal efficiencies ε at $\sqrt{s} = 208$ GeV for a constant mass difference ΔM and a constant chargino mass $M_{\tilde{\chi}_1^\pm}$, respectively. The signal efficiencies vary from $O(2\%)$ at small chargino masses to $O(0.1\%)$ close to the kinematic limit. The rather low signal efficiencies are due to the requirement of having a high energy ISR photon within the detector fiducial region.

As indicated in Figure 4.7 (a) the gaugino-like and higgsino-like signal efficiencies differ at small chargino masses ($M_{\tilde{\chi}_1^\pm} \leqslant 65$ GeV). This effect is simply due to the suppressed coupling of the higgsino component to Z. Radiative returns to the Z and the subsequent pair-production of charginos is more likely in the gaugino-like scenario and thus the signal efficiencies are higher.

While for most of the tested ΔM range the efficiency is constant it significantly drops for very small mass differences ($\Delta M < 0.5$ GeV, see Figure 4.7 (b)). This effect is due to reduced phase space: In this case all of the chargino decay products are particles with low momentum and most of these events do not pass the track quality cuts during the pre-selection.

In order to demonstrate the sensitivity of the analysis, the "relative efficiency", ε', i.e. the efficiency for a subset of generated events with $E_T^\gamma > 0.025\sqrt{s}$ and $|\cos\theta^\gamma| < 0.985$, is illustrated in Figure 4.7 (c) and (d). The evolution of the absolute and relative signal efficiency for one ($M_{\tilde{\chi}_1^\pm}$, ΔM) grid point for the gaugino-like scenario at a centre-of-mass energy of $\sqrt{s} = 208$ GeV is summarised in Table 4.2.

The number of accumulated expected signal events as a function of the tested chargino mass and the tested mass difference for both the gaugino-like scenario and the higgsino-scenario is shown in Figure 4.8.

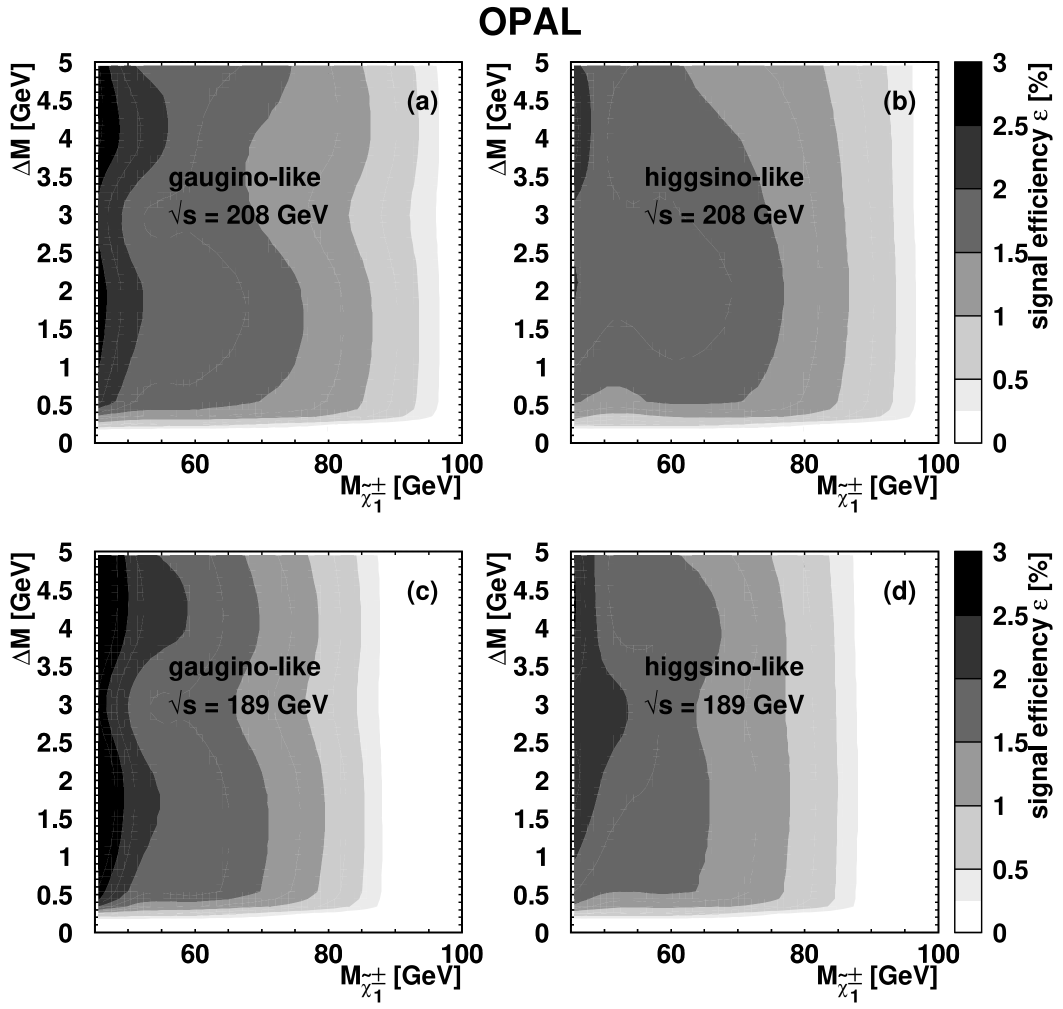

Figure 4.6: Absolute signal efficiency (number of selected signal events normalised to the number of generated events) as a function of the tested chargino mass and mass difference. Shown are the efficiencies for the gaugino-like scenario ((a)+(c)) and for the higgsino-like scenario ((b)+(d)) at two different centre-of-mass energies.

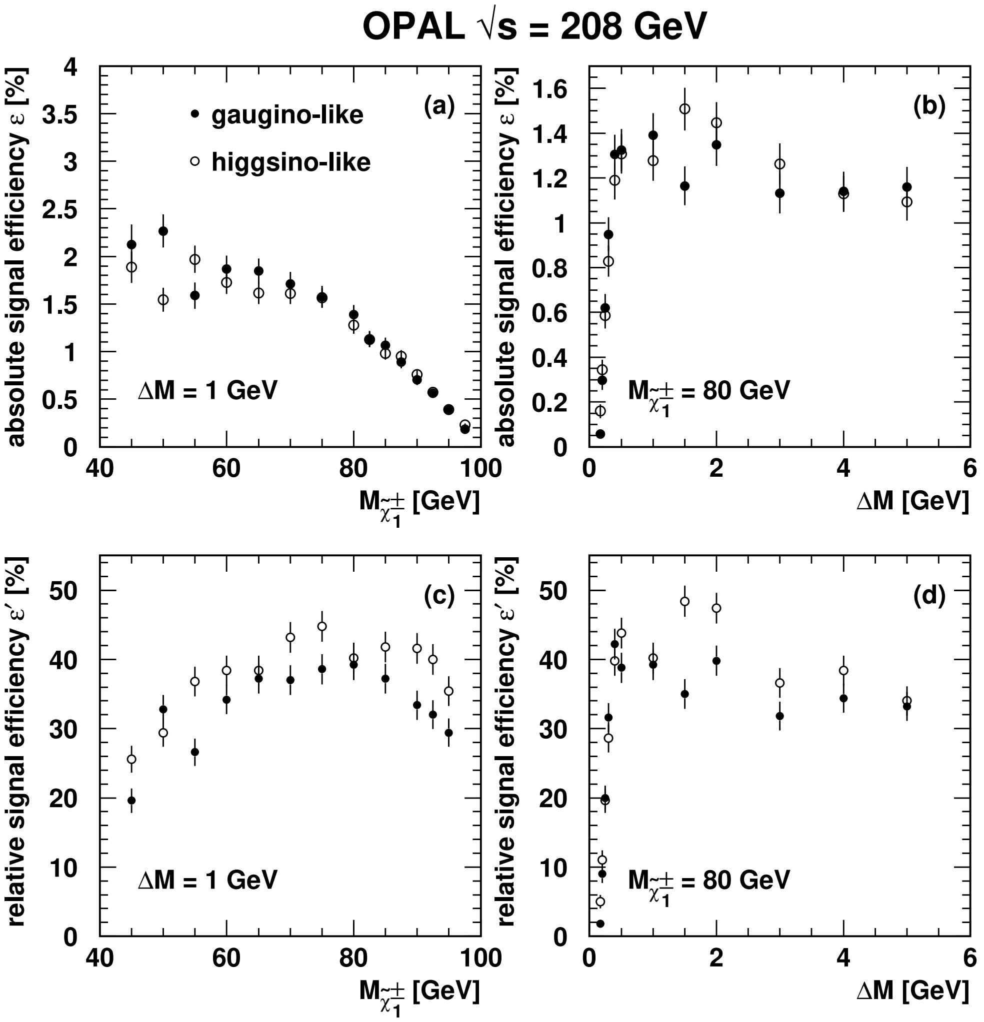

Figure 4.7: Absolute signal efficiency (number of selected signal events normalised to the number of generated events), ε, and relative efficiency (number of selected signal events normalised to a subset of generated events with $E_{\mathrm{T}}^{\gamma} > 0.025\sqrt{s}$ and $|\cos\theta^{\gamma}| < 0.985$), ε', at $\sqrt{s} = 208$ GeV for a constant mass difference $\Delta M = 1$ GeV ((a)+(c)) and for a constant chargino mass $M_{\tilde{\chi}_1^{\pm}} = 80$ GeV ((b)+(d)). The efficiencies for the gaugino-like scenario are indicated by the points. The circles correspond to the efficiencies in the case of a higgsino-like chargino.

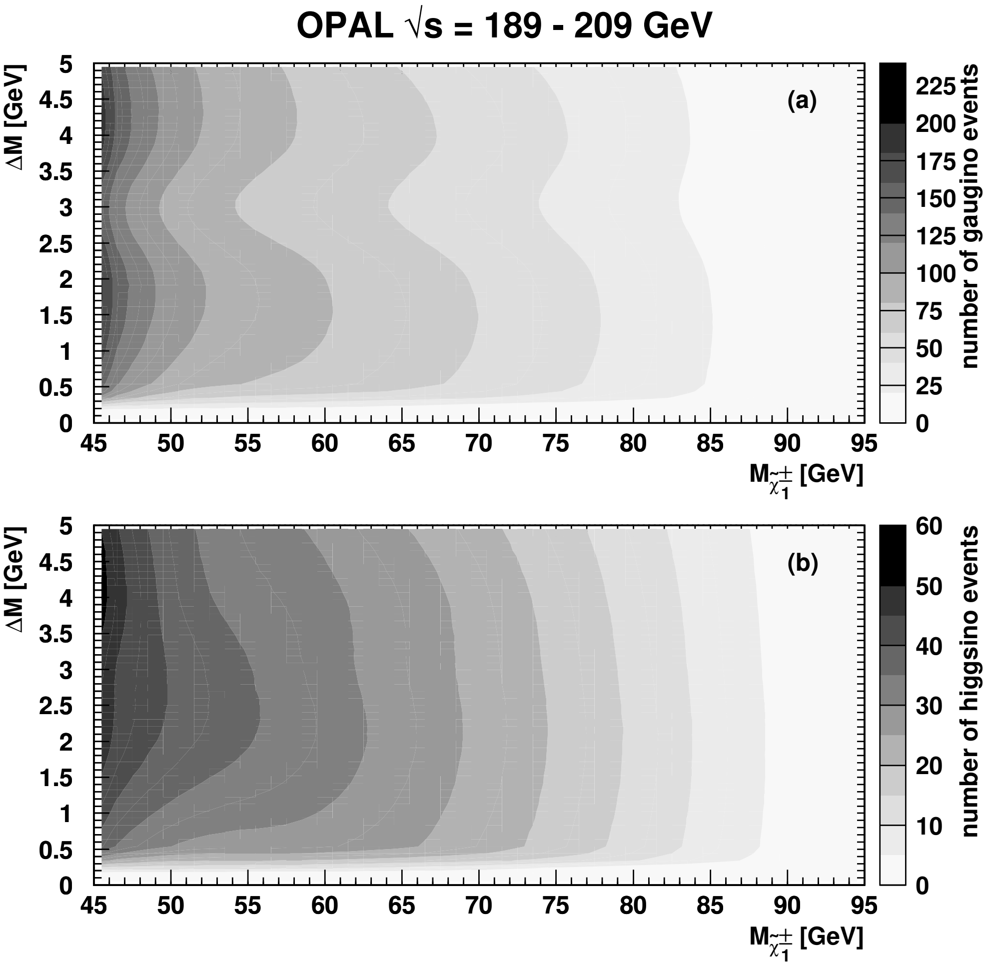

Figure 4.8: Number of expected gaugino-like events (a) and number of higgsino-like events (b) passing the final selection cuts. The accumulated events for $\sqrt{s}$ =189 – 209 GeV are shown. The sneutrino mass was set to $M_{\tilde{\nu}}$ = 1000 GeV.

4.2 Study of Systematic Uncertainties

4.2.1 Uncertainties on the Signal Efficiency

The systematic errors on the signal efficiency arise from several sources. They are described in the following. The size of the uncertainties strongly depends on the tested $(M_{\tilde{\chi}_1^\pm}, \Delta M)$ point.

Statistical Uncertainties and Uncertainties due to the Efficiency Interpolation

To take into account the uncertainty due to the limited Monte Carlo statistics and the uncertainty introduced due to the efficiency interpolation, the signal efficiencies the signal efficiencies were randomly smeared within their statistical errors and the resulting distribution was interpolated. This process was repeated 100 times and the absolute values of the differences between the original and the smeared fits were averaged. The mean difference in each tested ($M_{\tilde{\chi}_1^\pm}$, ΔM) point was taken as a measure of the systematic error. The size of the systematic uncertainty depends on the tested chargino mass and is maximal for $M_{\tilde{\chi}_1^\pm} \lesssim 65$ GeV, where the relative error reaches $O(5\%)$.

Uncertainties due to the Modelling of ISR

One important source of a systematic uncertainty arises from the ISR photon simulation in the signal Monte Carlo samples. At the time of this writing there exist no complete calculations for ISR in the chargino sector. However, a very similar situation occurs in case of W pair production. Like in the chargino pair production it has contributions from both, s- and t-channel. For the W pair production higher order calculations exist as opposed to chargino pair production.

The size of the uncertainty arising from the ISR photon simulation was estimated by re-weighting the transverse momentum spectrum of ISR photons in SUSYGEN. Event weights were extracted from a comparison of the ISR transverse momentum spectra of $W^+ W^-$ events produced with the KORALW generator with and without QED corrections up to order α^3. The maximum difference between the interpolated signal efficiencies calculated with un-weighted events and the interpolated signal efficiencies calculated with re-weighted events was used as the systematic uncertainty for all grid points and centre-of-mass energies. The derived relative systematic uncertainty amounts to 20% in case of the higgsino-like scenario and 22.3% in case of the gaugino-like scenario.

Uncertainties due to the Modelling of the ECAL

Another systematic uncertainty arises from the modelling of the ECAL energy scale and the ECAL energy resolution which directly affect the reconstructed ISR photon candidate. The size of the data-Monte Carlo discrepancy for the energy scale and the energy resolution was studied using $e^+e^- \to e^+e^-$ events from high energy data as well as Z^0 calibration data [97].

To account for the energy scale uncertainty, the ISR photon energy was shifted by $\pm 1\%$. The resulting interpolated efficiencies were compared with the original efficiency spline. The maximum deviation in each tested ($M_{\tilde{\chi}_1^\pm}$, ΔM) point from the original spline was used as a measure of the systematic error. The largest relative uncertainties appear at small chargino masses ($M_{\tilde{\chi}_1^\pm} \lesssim 55$ GeV) and amount to $O(2\%)$.

To study the ECAL resolution effects the difference between true and measured photon energy divided by the measured energy error was calculated. This pull distribution was broadened by $\pm 20\%$. Event weights were extracted from the ratios of the original and broadened pull distributions. The resulting signal efficiencies were interpolated and the fits were compared with the original efficiency spline. Again, the maximum deviation in each tested ($M_{\tilde{\chi}_1^\pm}$, ΔM) point was taken as the systematic uncertainty. The systematic uncertainties are maximal in the intermediate tested chargino mass range (60 GeV $\lesssim M_{\tilde{\chi}_1^\pm} \lesssim$ 80 GeV). In this region the relative systematic uncertainty due to ECAL resolution effects is of order $O(5-10\%)$.

Uncertainties due to the Modelling of the Cut Variables

Finally, the systematic uncertainties on modelling the final cut variables were studied. Since the cut on the recoil mass, F1, is indirectly a cut on the energy of the ISR photon (see Equation (4.1)) the systematic uncertainty due to the modelling of F1 are already treated by the described study of the ECAL behaviour.

Systematic effects due to the modelling of the cut on the visible energy, F2, was investigated by shifting the cut value by $\pm 5\%$. The resulting efficiencies were compared with the original ones. The maximum deviation in each tested ($M_{\tilde{\chi}_1^\pm}$, ΔM) point from the original spline was assumed as systematic error. It was found that the largest effects occur for $M_{\tilde{\chi}_1^\pm} \lesssim 60$ GeV. In this region the relative systematic error amount to $O(5\%)$.

The Size of Systematic Effects

In Figure 4.9 and Figure 4.10 examples for the size of the considered systematic uncertainties on the signal efficiencies is illustrated. The systematic uncertainties are rather small ($O(20\%)$ at the most) and their effect is moderate. Especially close to the kinematic limit the systematic error bands are small and the derived signal efficiencies are stable. Exact values for the systematic uncertainties for one exemplary signal sample can be found in Table 4.5.

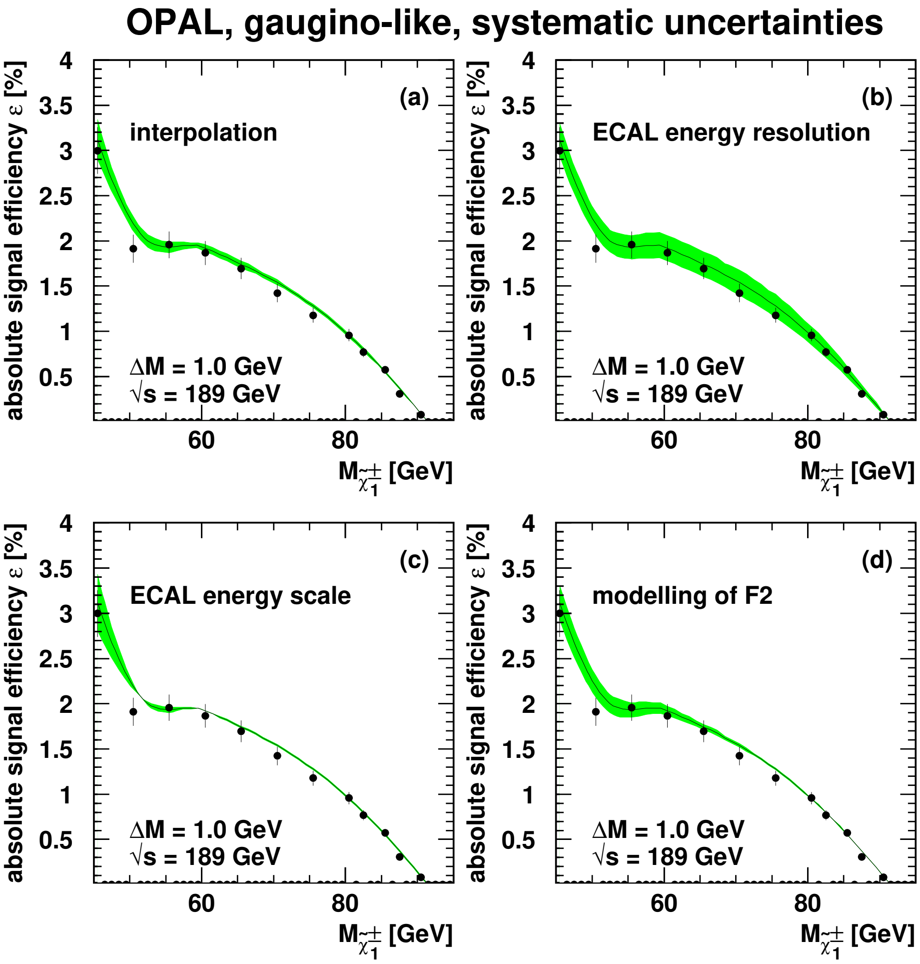

Figure 4.9: Illustration of the size of the systematic uncertainties for $\sqrt{s}$ =189 GeV and ΔM =1.0 GeV in case of the gaugino scenario. The derived signal efficiencies are indicated by points with error bars (statistical error) and the result of the spline fit by the black line. The shaded band shows the size of the systematic uncertainties due to the efficiency interpolation (a), the ECAL energy resolution (b), the ECAL energy scale (c) and the modelling of the cut on the visible energy (d).

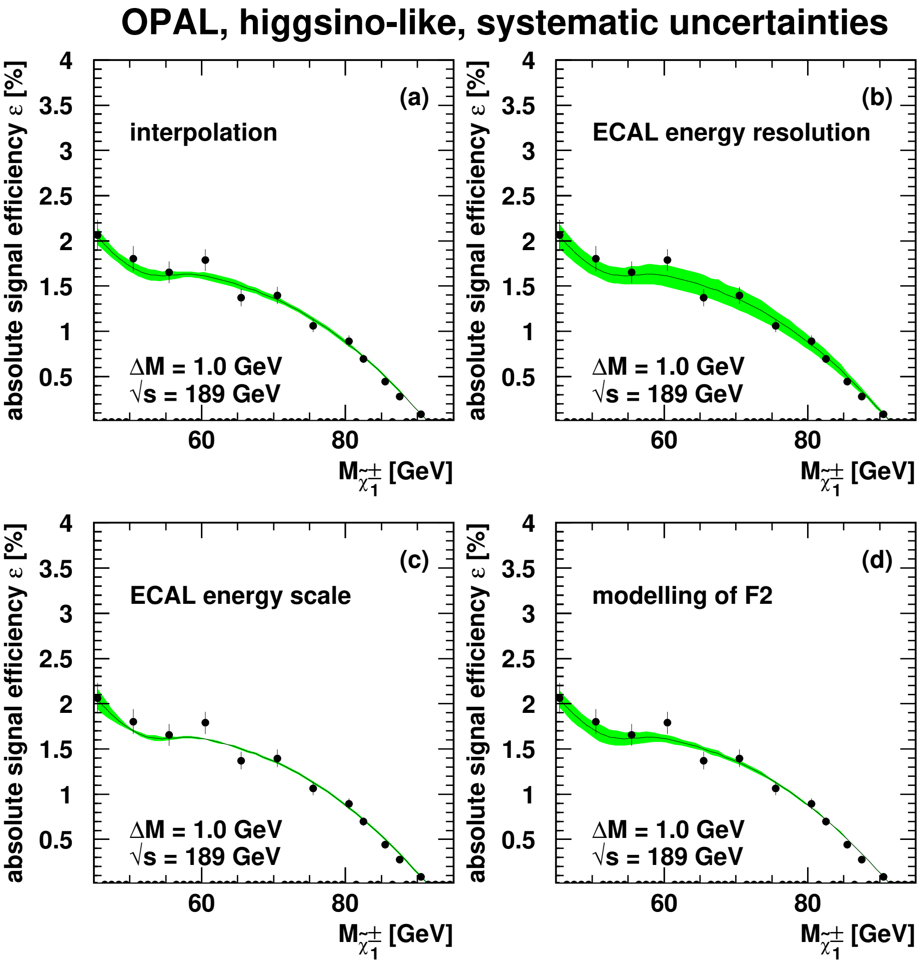

Figure 4.10: Illustration of the size of the systematic uncertainties for $\sqrt{s}$ =189 GeV and ΔM =1.0 GeV in case of the higgsino scenario. The derived signal efficiencies are indicated by points with error bars (statistical error) and the result of the spline fit by the black line. The shaded band shows the size of the systematic uncertainties due to the efficiency interpolation (a), the ECAL energy resolution (b), the ECAL energy scale (c) and the modelling of the cut on the visible energy (d).

4.2.2 Uncertainties on the Background Estimation

The following sources of systematic uncertainties on the number of expected background events were investigated. The limited Monte Carlo statistics was taken into account. The systematic uncertainties due to the Monte Carlo modelling of the ECAL energy and the ECAL energy resolution as well as the modelling of the cut variables were estimated as described above. As an example Table 4.5 gives an overview on the size of systematic uncertainties for the signal efficiency and the number of expected background events at $M_{\tilde{\chi}_1^\pm} = 80\,\mathrm{GeV}$ and $\Delta M = 1\,\mathrm{GeV}$.

	signal efficiency ($\sqrt{s} = 208\,\mathrm{GeV}$)	**background ($\sqrt{s} = 189 - 208\,\mathrm{GeV}$)**
central value	1.3%	1.3 events
statistical error/ interpolation	$\pm$1.5%	$\pm$0.2 events
ISR modelling	$\pm$22.3%	–
ECAL resolution	$\pm$7.6%	$\pm$0.6 events
energy scale	$\pm$0.8%	$\pm$0.1 events
cut modelling	$\pm$1.5%	$\pm$0.1 events
total	$\pm$23.7%	$\pm$0.6 events

Table 4.5: The left column lists the signal efficiency and relative statistical and systematic uncertainties at $\sqrt{s} = 208$ GeV in case of the gaugino-like scenario for $M_{\tilde{\chi}_1^\pm} = 80$ GeV and $\Delta M = 1$ GeV after the final cut F2. The right column shows the total number of expected background events and the absolute statistical and systematic uncertainties for $M_{\tilde{\chi}_1^\pm} = 80$ GeV and $\Delta M = 1$ GeV after the final cut F2.

For the two-photon veto a cut on the amount of energy deposited in the forward detectors was applied (see Section 4.1.5). This energy could also have been deposited by accelerator related activity, e.g. synchrotron radiation, which was not included in the Monte Carlo simulation. Therefore more data events were vetoed than predicted by the Monte Carlo simulations and the effective luminosity was smaller than the measured one. To account for this effect the frequency of the occurrence of such accelerator related background was estimated from a sample of so-called random beam crossing events, events for which the data acquisition was triggered randomly rather than by a real physics event. From this study it was found that the effective luminosity was $\sim 3\%$ smaller than the measured luminosity.

4.3 Result Interpretation

4.3.1 Calculating Limits

The analysis results can be summarised in few numbers: the number of expected background events b, the number of expected signal events s for given set of model parameters and the number of candidates n. The interpretation of these numbers has to distinguish between two hypotheses: the production and detection of charginos along with SM background (S + B), or the presence only of SM background (B). The confidence level (C.L.) is defined as the probability that the search would have missed the signal by as much or more than the search outcome actually observed. An estimator X is needed to separate signal-like outcomes from background-like outcomes. In general this is a function of b, s and n which monotonically increases with n. An optimal choice for the estimator is the likelihood ratio [98]:

$$X = \frac{e^{-(s+b)}(s+b)^n}{n!} \bigg/ \frac{e^{-b}b^n}{n!} \tag{4.2}$$

For the case of N counting search experiments which are supposed to be combined the estimator definition can be extended as follows:

$$X = \prod_{i=1}^{N} X_i = \prod_{i=1}^{N} \frac{e^{-(s_i+b_i)}(s_i+b_i)^{n_i}}{n_i!} \bigg/ \frac{e^{-b_i}b_i^{n_i}}{n_i!} \tag{4.3}$$

It is now possible to define the probability that an experiment would look less signal-like than the data, assuming a signal exists:

$$\mathrm{CL_{s+b}} = P_{\mathrm{s+b}}(X \leqslant X_{\mathrm{obs}}) \tag{4.4}$$

where X_{obs} is the value of the estimator computed from the observed b, s and c, and the probability is the fraction of possible experimental outcomes, weighted by their probability of happening, assuming the presence of both signal and background. Similarly defined is the probability that an experiment would look less background-like than the data, assuming that no signal exists:

$$\mathrm{CL_b} = P_{\mathrm{b}}(X \leqslant X_{\mathrm{obs}}) \tag{4.5}$$

The drawback of these definitions is that in case of an overestimated background (or a statistical upward fluctuation of the expected background) or a statistical downward fluctuation of the candidates the observed outcome is incompatible with both hypotheses and even the SM background may be ruled out. Therefore the $\mathrm{CL_s}$ value is often used to define the C.L.:

$$\mathrm{CL_s} = \frac{\mathrm{CL_{s+b}}}{\mathrm{CL_b}} = 1 - \mathrm{C.L.} \tag{4.6}$$

The signal hypothesis is then excluded at a confidence level C.L. when

$$1 - \mathrm{CL_s} \leqslant \mathrm{C.L.} \tag{4.7}$$

In order to demonstrate the sensitivity of a search experiment the expected confidence level, $\mathrm{C.L.}_{\mathrm{exp}}$, is typically introduced. It can be derived in the above described way using the Poisson probability distribution of expected candidates from the background-only estimate.

The present analysis shows no evidence for $\tilde{\chi}_1^+\tilde{\chi}_1^-$ production in case of small ΔM. Exclusion regions and limits were determined for various scenarios using the described likelihood ratio method. The program package used for the calculations is described in [98]. The package takes care of systematic uncertainties[2] following a generalisation of the method of Cousins and Highland [99] using a Monte Carlo technique allowing for a correct treatment of correlated errors.

[2]The systematic uncertainties are assumed to be symmetric. In addition, true signal and background distributions are presumed.

4.3.2 Cross-section Limits

An upper limit for the $\tilde{\chi}_1^+\tilde{\chi}_1^-$ production cross-section σ was derived from the number of expected background events, the number of observed candidates and the higgsino-like scenario signal efficiencies. The signal efficiencies for the higgsino-like scenario are slightly smaller than those of the gaugino-like scenario and therefore result in more conservative limits. Figure 4.11 (a) shows the observed upper cross-section limits in the $(M_{\tilde{\chi}_1^\pm}, \Delta M)$ plane. Production cross-sections above $\sim 0.4 - 3.7$ pb were excluded for chargino masses between 45 GeV and ~ 95 GeV and for $0.5\,\text{GeV} \leq \Delta M \leq 5.0\,\text{GeV}$ at the 95% confidence level (C.L.) rescaled to $\sqrt{s} = 208\,\text{GeV}$ assuming the signal cross-section evolution with $\sqrt{s}$ calculated by SUSYGEN. The expected and observed upper cross-section limits for ΔM =1 GeV as a function of the chargino mass are illustrated in Figure 4.11 (b).

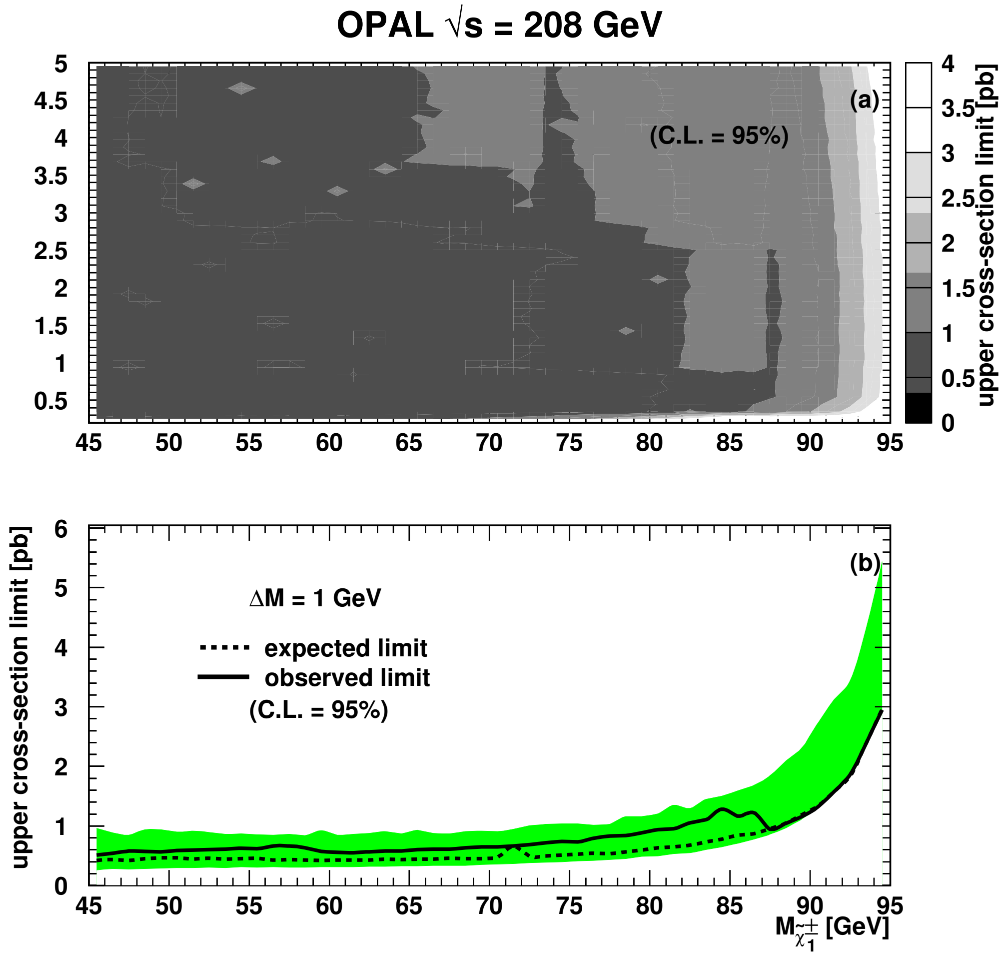

Figure 4.11: Upper signal cross-section limit rescaled to $\sqrt{s} = 208$ GeV at the 95% confidence level as a function of the mass difference and the chargino mass (a) and for a constant mass difference of $\Delta M = 1$ GeV (b). The band in (b) indicates the $\pm 2\sigma$ interval around the median expected value.

4.3.3 Interpretation within the MSSM

Within the MSSM the chargino and neutralino masses depend on four parameters (see Section 1.3.1): the ratio of the two Higgs vacuum expectation values, $\tan\beta$; the Higgs mixing parameter, μ and the $U(1)$ and $SU(2)$ gaugino mass parameters, M_1 and M_2 respectively. Unless specified, in the following the value of $\tan\beta$ was set to 1.5. As explained earlier in Section 2.3 within the MSSM small mass differences, ΔM, occur in the following two scenarios:

- In the higgsino-like scenario is $|\mu| \ll M_2$, the lightest chargino, $\tilde{\chi}_1^\pm$, is almost a higgsino. In this scenario the lightest chargino and neutralino are mass-degenerate ($M_{\tilde{\chi}_1^\pm} \sim M_{\tilde{\chi}_1^0} \simeq |\mu|$) for very large values of M_2.

- If $M_2 \ll |\mu|$ and $M_1/M_2 > 1$, the lightest chargino, $\tilde{\chi}_1^\pm$, is dominated by the gaugino component and is degenerate in mass with the lightest neutralino with $M_{\tilde{\chi}_1^\pm} \sim M_{\tilde{\chi}_1^0} \sim M_2$.

Figure 4.12 shows the cross-sections used to calculate the mass exclusion limits for the gaugino-like and higgsino-like scenarios. Since the coupling of the higgsino component of the chargino does not couple to the sneutrino, the cross-sections in case of the gaugino-like scenario are more sensitive to the interfering t-channel production and therefore more sensitive to the sneutrino mass.

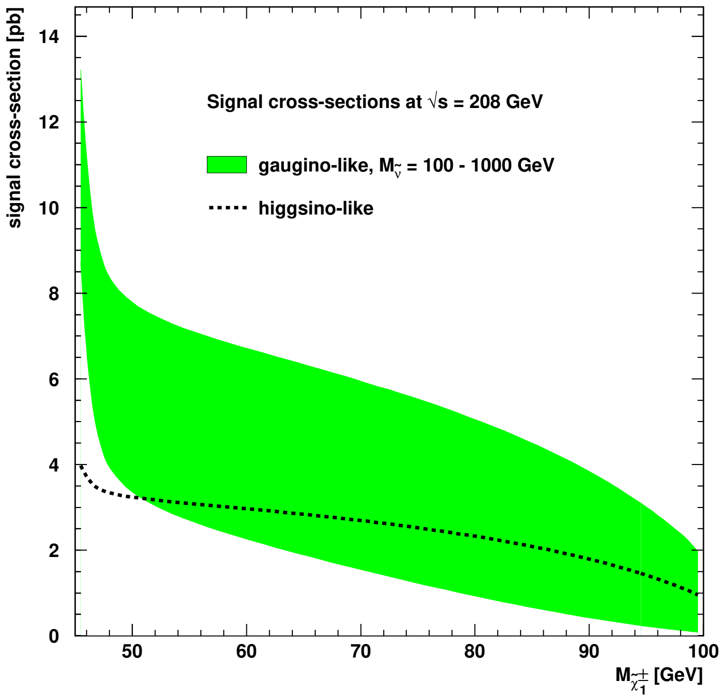

Figure 4.12: Signal cross-sections as a function of the chargino mass at $\sqrt{s} = 208$ GeV. The shaded band shows the cross-sections in case of a gaugino-like chargino for sneutrino masses ranging from 100 to 1000 GeV. The dashed line corresponds to the higgsino-like scenario.

A scan in the MSSM parameter space was carried out. For fixed values of R_S, $M_{\tilde{\nu}_e}$ and $\tan\beta$ the parameters μ, M_2 were varied. From this scan the chargino mass exclusion regions for both the gaugino-like and higgsino-like scenario were derived as presented in Figure 4.13. These results correspond to the lower chargino mass limits listed in Table 4.6. The limits are valid for 0.5 GeV $\leqslant \Delta M \leqslant$ 5.0 GeV and zero chargino lifetime assuming a 100% branching ratio $\tilde{\chi}_1^{\pm} \to \tilde{\chi}_1^0 W^{\pm(\star)}$.

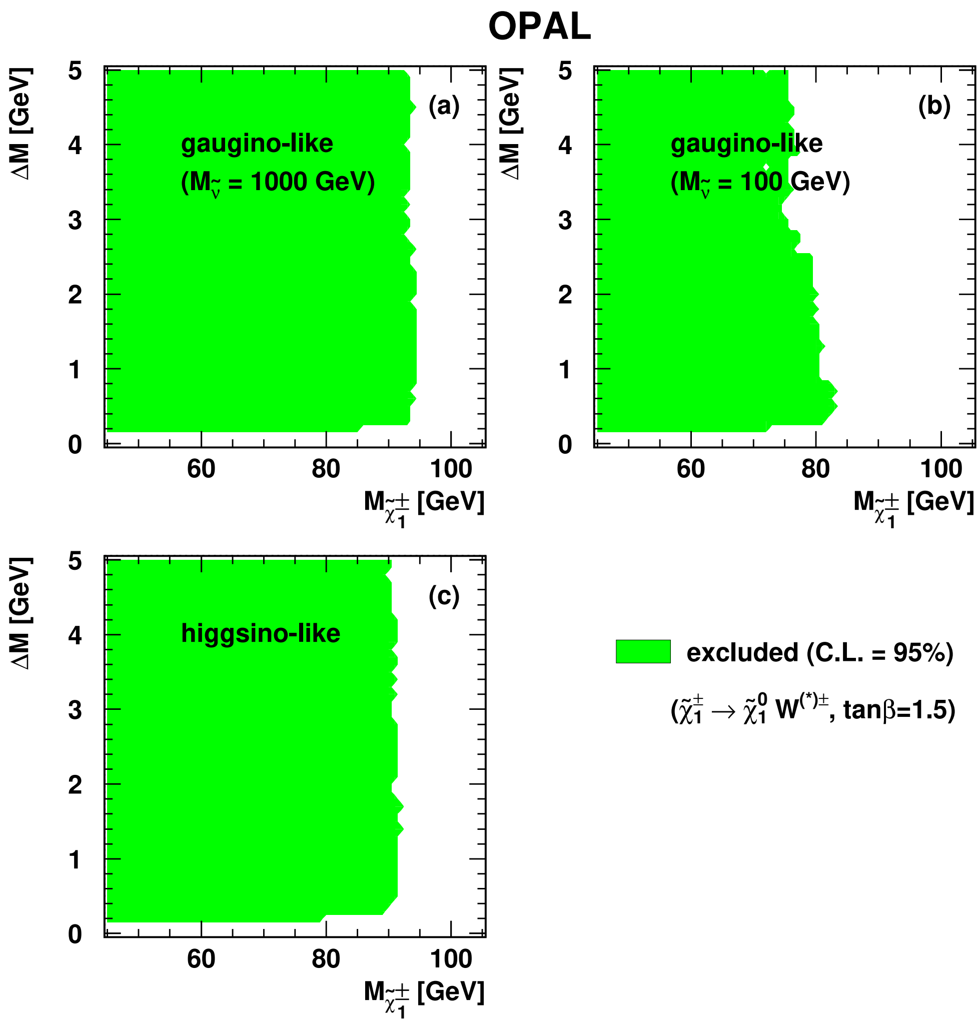

Figure 4.13: Lower mass limits at the 95% confidence level for various scenarios. These limits are valid for the case of a 100% branching ratio $\tilde{\chi}_1^{\pm} \to \tilde{\chi}_1^0 W^{\pm(\star)}$. The limits shown for $\Delta M < 0.5$ GeV are only valid with the assumption of a zero chargino lifetime. For the gaugino-like scenario with a light sneutrino (b) the same signal efficiencies as in the case of a heavy sneutrino (a) were assumed.

scenario	lower $M_{\tilde{\chi}_1^\pm}$ limit (95% C.L.)
higgsino-like	89 GeV
gaugino-like ($M_{\tilde{\nu}_e} = 1000\,\mathrm{GeV}$)	92 GeV
gaugino-like ($M_{\tilde{\nu}_e} = 100\,\mathrm{GeV}$)	74 GeV

Table 4.6: Lower chargino mass limits at the 95% C.L. within the mSUGRA framework. The limits are valid for 0.5 GeV $\leqslant \Delta M \leqslant$ 5.0 GeV and zero chargino lifetime.

The higgsino-like results are also valid in mSUGRA models (see Section 2.3), whereas the gaugino-like scenario results require a relaxed M_1/M_2 relation (Equation (2.10)) for an interpretation within an mSUGRA-like framework. The mass limits can be directly translated into exclusion regions for the above mentioned MSSM parameters as shown in Figure 4.14.

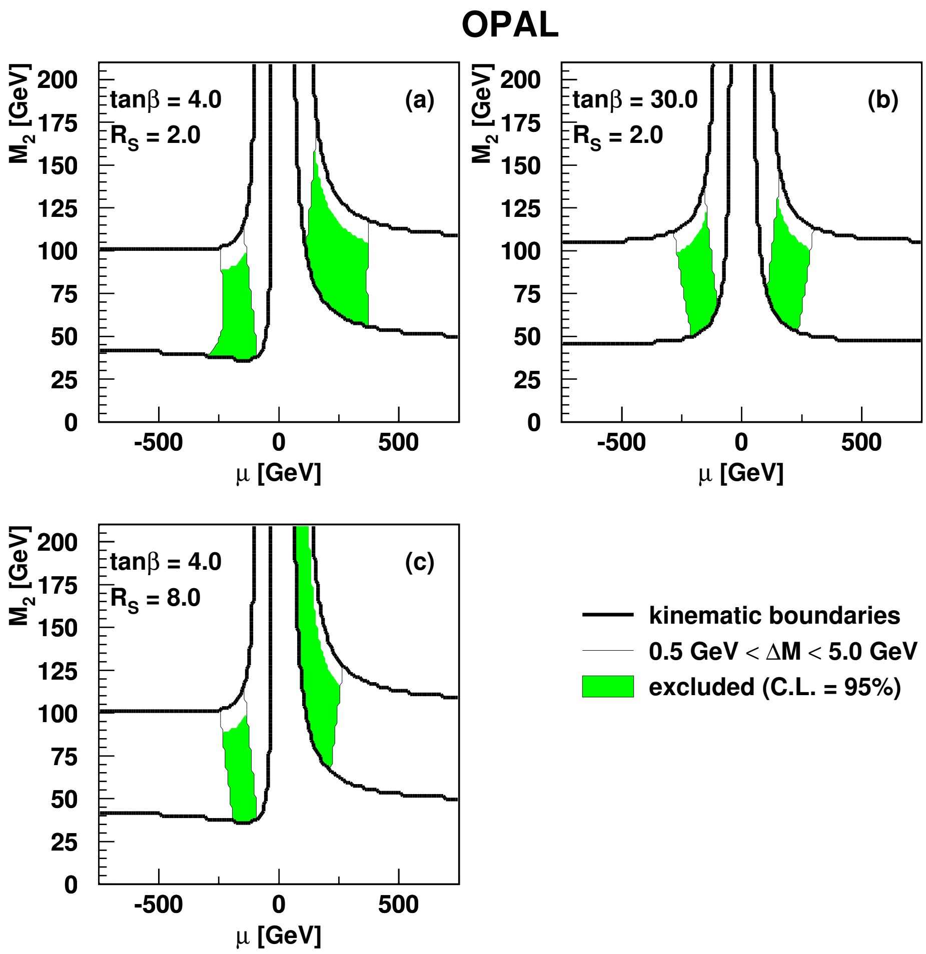

Figure 4.14: Exclusion regions at 95% C.L. in the μ-M_2 plane within the unconstrained MSSM framework for two values of R_S and two different values of $\tan\beta$. The kinematic boundaries (45 GeV $< M_{\tilde{\chi}_1^\pm} <$ 104 GeV) are shown by the thick line. The thin line indicates the ΔM region considered. The shaded areas are the regions excluded by this analysis for $M_{\tilde{\chi}_1^\pm} <$ 92 GeV.

4.3.4 Interpretation within the AMSB Framework

Alternatives to gravity mediated SUSY breaking scenarios can have the SUSY breaking not directly communicated from the hidden to the visible sector, as in the Anomaly Mediated SUSY Breaking Scenario (AMSB).

In this scenario the chargino is gaugino-like and the $R_S = M_1/M_2$ ratio is ~ 2.8. AMSB models are described by the following parameters: a universal scalar mass at the GUT scale, m_0; the gravitino mass $m_{3/2}$; $\tan\beta$ and signμ. AMSB scenarios are not implemented in the SUSYGEN generator. However, the obtained mSUGRA gaugino-like scenario results can be re-interpreted in order to derive exclusion limits for the AMSB scenario. The ISAJET generator [76] contains a package to calculate AMSB chargino and neutralino mass spectra as a function of the AMSB parameters. These mass spectra were compared with the gaugino-like scenario mass spectra calculated with SUSYGEN and it was tested which chargino/neutralino mass combinations were already excluded. From this comparison a map between the AMSB and mSUGRA parameters was produced which was then used to derive exclusion regions within the AMSB parameter space as illustrated in Figure 4.15.

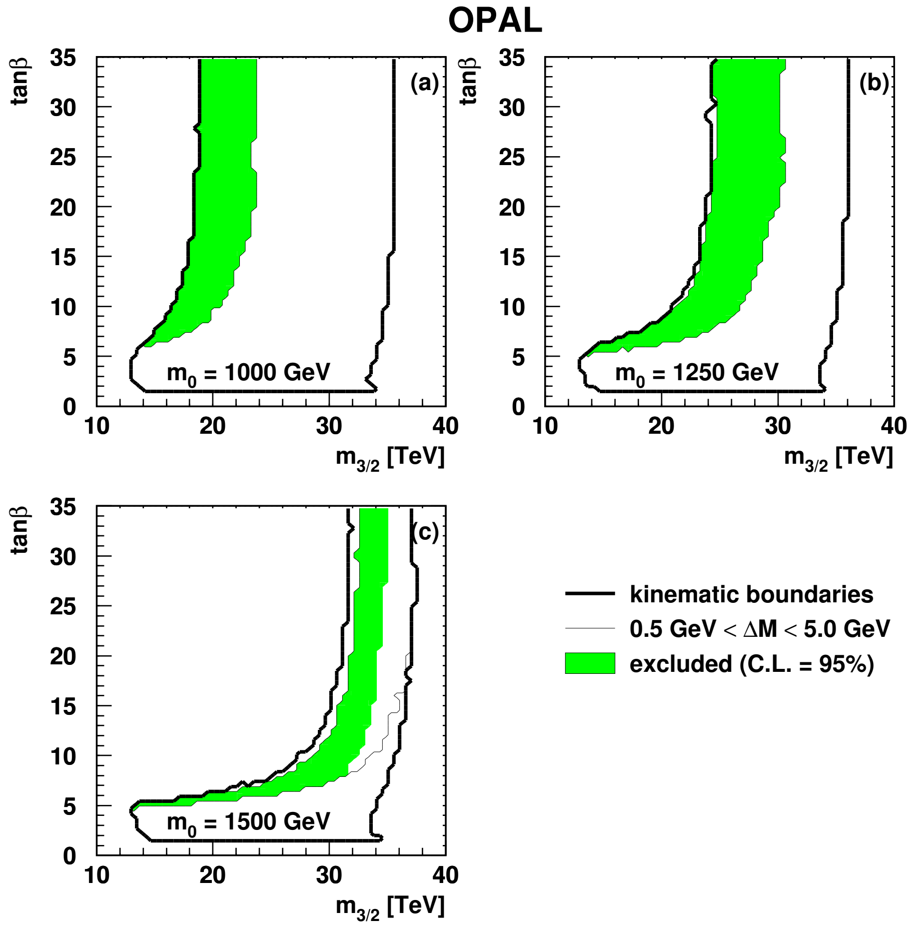

Figure 4.15: Exclusion regions at 95% C.L. in the $\tan\beta$-$m_{3/2}$ plane for various values of m_0 within the AMSB framework. The kinematic boundaries (45 GeV $< M_{\tilde{\chi}_1^\pm} <$ 104 GeV) are shown by the thick line. The region below $\tan\beta = 1.5$ is theoretically inaccessible. The thin line indicates the ΔM region considered. The shaded areas are the regions excluded by this analysis.

4.4 Discussion of the Results

The present analysis proved the feasibility of the ISR method. Although the signal detection efficiencies turned out to be very small ($\mathcal{O}(1\%)$) the method is sensitive over almost the full kinematically allowed mass region due to the large cross-section. Cross-section and mass limits exclude the existence of almost mass-degenerate charginos and neutralinos in all considered SUSY scenarios. The two-photon veto requirement (Equation (2.9)) does not allow to extend the limits to the kinematic boundary. The next round of chargino searches definitely requires new experiments with a better angular coverage and of course a higher centre-of-mass energy. In general the analysis reached its goal to close the sensitivity gap described in Section 2.2. The next task will be the combination of all three search strategies in order to derive a ΔM-independent chargino mass limit.

The obtained results are competitive with the results from the other LEP collaborations, ALEPH, DELPHI and L3. All of them applied the ISR method in order to retain sensitivity in the small ΔM region. Figure 4.16 shows the mass exclusion regions of all LEP experiments.

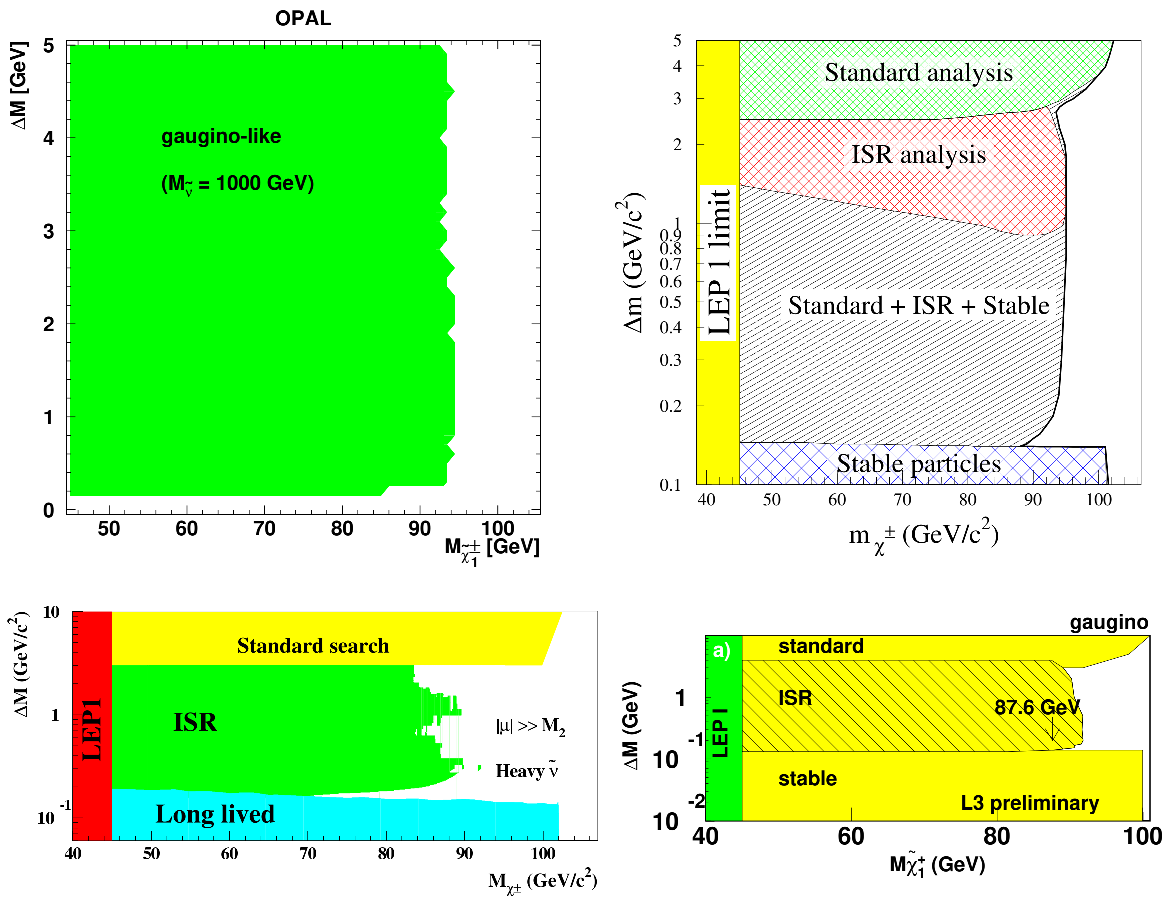

Figure 4.16: Overview on the chargino mass limits in the small ΔM region for the gaugino-like scenario obtained by the four LEP experiments: OPAL (upper left corner, this analysis), ALEPH (upper right corner, [100]), DELPHI (lower left corner, [101]) and L3 (lower right corner, [102]).

The exclusion regions for the considered mass difference range (0.5 GeV $<$ 5.0 GeV) are very similar. The individual mass limits of all experiments are summarised in Table 4.7. The quoted lower mass limits depend strongly on the investigated ΔM region and considered scalar-neutrino mass, $M_{\tilde{\nu}}$, and thus differ from experiment to experiment. A similar effect arises from different detector configurations (especially in the forward region coverage and in the size of the magnetic field).

	gaugino [GeV]	higgsino [GeV]	ΔM [GeV]	$M_{\tilde{\nu}_e}$ [GeV]	$\sqrt{s}$ [GeV]
ALEPH	88	88	> 0	> 500	189–209
DELPHI	70	75	> 0	> 500	189–209
L3	87.6	85.9	> 0	–	189–209
OPAL	92	89	0.5 – 5	> 1000	189–209
LEP	92.4	91.9	0.06 – 10	> 1000	189–209

Table 4.7: Summary of the gaugino-like scenario and higgsino-like scenario mass limits at 95% C.L. from ALEPH, DELPHI, L3 and OPAL. L3 does not quote a number for the sneutrino mass. The last line shows the limits obtained from the combination of all four experiments. The LEP combination does not take into account the systematic uncertainties of the individual experiments.

A first preliminary LEP wide combination for the ΔM range 0.06 – 10 GeV was performed. The results from this analysis were provided for 0.5 GeV $< \Delta M <$ 5.0 GeV. The combination does not take into account systematic uncertainties of the individual experiments. The combined mass exclusion regions are illustrated in Figure 4.17. In the small ΔM regime the lower mass limits were increased by $O(3\,\mathrm{GeV})$. The overall mass limits are listed in Table 4.7. The lowest limits are obtained in the region of $\Delta M \sim 200$ MeV.

The ISR method will definitely belong to the analysis repertoire at future colliders. If SUSY is realized in Nature also the discovery of almost mass-degenerate charginos and neutralinos will be possible. Moreover, as it will be shown in the next Chapter the ISR method allows to perform precision measurements. However, necessary for a discovery will be a deeper understanding of two-photon events and a more accurate knowledge of ISR.

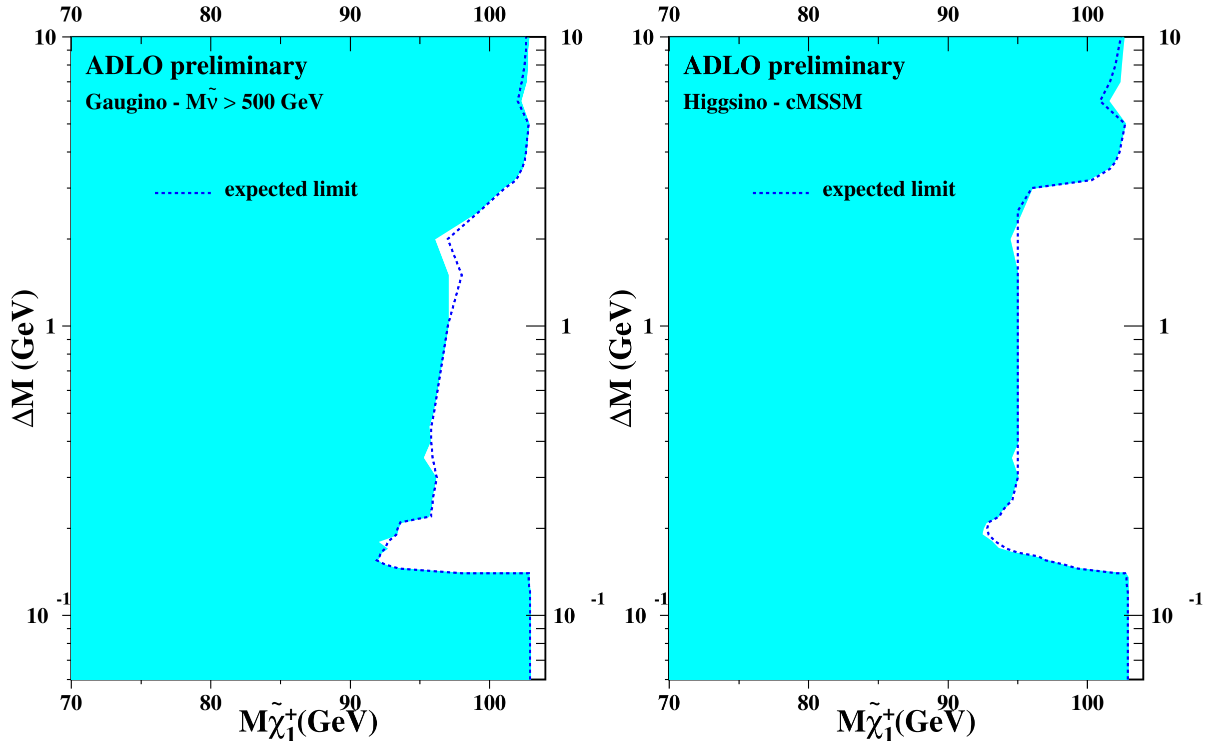

Figure 4.17: LEP combined mass exclusion regions for 0.06 GeV $< \Delta M <$ 10 GeV. The shaded areas indicate the observed limits while the lines indicate the expected limits. The limits were obtained from the combination of all introduced search strategies (Chapter 2). Compared to the results of the single experiments the lower mass limits in the small ΔM region (0.5 GeV $<$ $\Delta M <$ 5.0 GeV) could be increased by $O(3\,\mathrm{GeV})$. The lowest limits are obtained in the region of $\Delta M \sim$ 200 MeV. The results are preliminary.

Chapter 5

The TESLA Physics Study

Although none of the LEP analyses showed an evidence for SUSY, it is certainly not justifiable to rule out a supersymmetric world. The current results reduce the MSSM parameter space by a good fraction and while constraining the possible SUSY scenarios they still leave enough room for a realisation of SUSY in Nature. To explore the remaining parameter space higher centre-of-mass energies and thus new colliders are required. If SUSY exists then it will be discovered at one of the next generation accelerators: Tevatron, LHC or TESLA. In a physics study the small ΔM regime at the TESLA Linear Collider was examined. This Chapter describes the results of this study. The first part deals with the special characteristics of a Linear Collider and their influence on the detector design, which in turn has a significant impact on the ISR method. In the second part the possibilities of precision measurements with the ISR method are examined. On purpose it does not describe the discovery potential of TESLA but rather the possibilities the ISR method leaves to extract the chargino and neutralino mass in case of nearly mass degeneracy.

5.1 Beam Dynamics in e^+e^- Collisions

5.1.1 The Pinch Effect and Beamstrahlung

Two colliding electron and positron bunches will focus each other in the field in the oncoming bunch. This effect is called the pinch effect. The trajectories of the particles inside the bunch are bent and the particles emit an electromagnetic radiation, the beamstrahlung. The focusing will lead to a reduction of the effective beam dimension and hence to an increase of the luminosity[1], described by the luminosity enhancement factor, H_D. This advantageous effect is balanced by the energy loss of the beam particles due to beamstrahlung which smears out the centre-of-mass energy. This smearing occurs in addition to the energy spread due to initial state radiation[2]. The average beamstrahlung energy loss, δ, of a beam particle can be expressed in terms of the beam dimensions $\sigma_{x,y,z}$ in x, y and z, the number of particles per bunch, N, the energy of the particle,

[1] The opposite effect occurs in case of two colliding bunches with same sign of charge.

[2] While initial state radiation is emitted by a particle within the field of another particle, beamstrahlung is emitted within the collective field of the oncoming bunch.

E, and the Lorentz factor, $\gamma = E/mc^2$, [103]:

$$\delta \propto \frac{\gamma}{E\sigma_z}\left(\frac{N}{\sigma_x+\sigma_y}\right)^2 \propto \frac{1}{E}\frac{\sigma_z}{\gamma}\Upsilon^2, \tag{5.1}$$

where Υ is the so-called beamstrahlung parameter. Two things can be derived from Equation (5.1):

- Since beam dimensions at machines like LEP are orders of magnitudes larger than the ones foreseen for TESLA (see Table 3.1) the beamstrahlung effects will play a more significant role at accelerators of the next generation.

- Since the longitudinal beam dimension has an upper bound due to the so-called hourglass effect [104] only the transverse beam dimensions can be used to tune the energy loss. In order to minimise the energy loss and retain at the same time a sufficiently large luminosity ($\mathcal{L} \propto \frac{1}{\sigma_x\sigma_y}$, see Equation (3.2)) elliptic beam cross-sections are chosen with a large ratio σ_x/σ_y. However, even with this choice the expected average energy loss per bunch particle is at the order of $O(1\mathrm{GeV})$.

Figure 5.1 illustrates the effect of beamstrahlung on the luminosity.

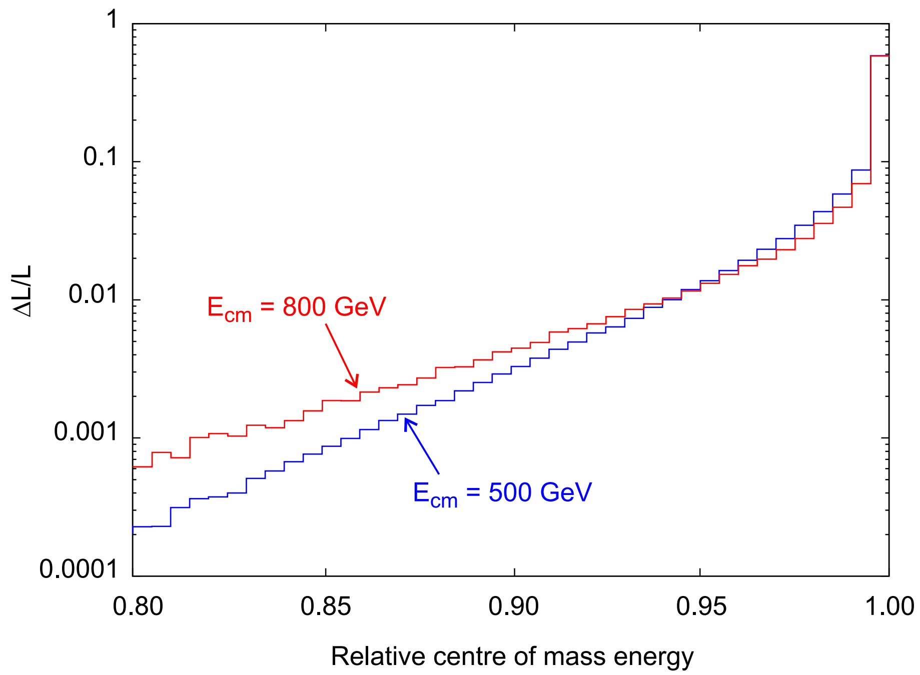

Figure 5.1: TESLA luminosity spectra for 500 and 800 GeV centre-of-mass energy as shown in [39]. The broadening of the spectra is due to beamstrahlung. ISR effects are not taken into account.

The total power of the beamstrahlung is of order $O(360\,\mathrm{kW})$ at $\sqrt{s} = 500$ GeV and more than doubles for $\sqrt{s} = 800$ GeV [39]. Fortunately, the beamstrahlung photons are very well collimated around the beam axis and leave the detector through the beam pipe[3]. Anyhow, secondary particles produced by these photons might have an impact on the detector performance. This beam induced background can be roughly divided in three categories:

Neutron Background

Although the beamstrahlung photons are collimated around the beam axis, the photons might hit beam line elements further downstream. An illustration of this is shown in Figure 5.2. Neutrons are then be produced via photo-nuclear reactions within electromagnetic showers. These neutrons can drift back into the detector region and might harm sensitive detector components like the VTX. The neutron background was studied [105, 106] using the program package FLUKA99 [107]. The number of neutrons inside the detector originating directly from beamstrahlung photons was found to be negligible. No significant background is expected from this source [41].

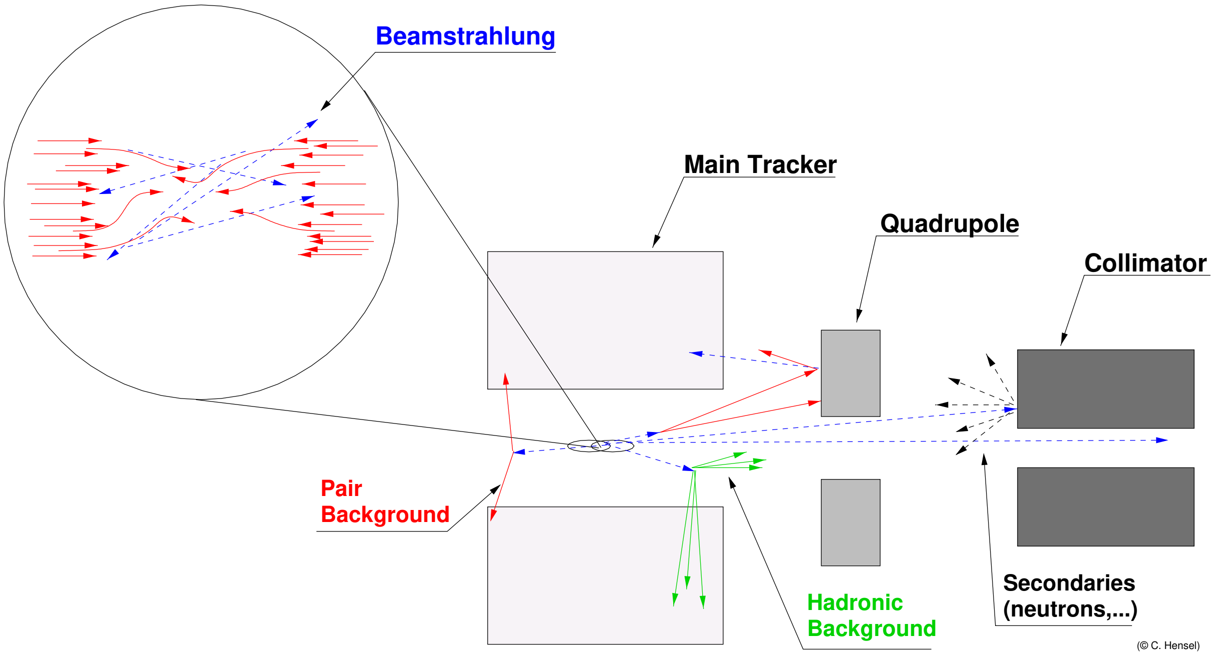

Figure 5.2: Detector sketch showing the origin of beamstrahlung and production of beam induced background, neutron background, hadronic background and pair background.

Hadronic Background

The beamstrahlung photons may also interact hadronically ($e^+e^- \rightarrow e^+e^-\gamma\gamma \rightarrow e^+e^-$ hadrons)[4]. These processes are not a severe background in terms of detector occupancies. But the hadronic

[3] The beamstrahlung has then collimated inside the beam pipe. Calculations show that this is possible.

[4] These processes are sometimes called 'mini-jet background'. There exists a huge variation in terminology, and depending on where the line is drawn between mini-jets and 'soft' hadronic hadronic background, more or less jet-like events can be included.

background might overlap with real physics events or even fake real physics events and distort the measurements. Simulation studies [88, 108] showed that the number of charged particles originating from hadronic background inside the central detector is low and that the time resolution of the TPC should allow to disentangle these tracks.

Pair Background

As every photon is always accompanied by virtual e^+e^- pairs (vacuum polarisation) which can be put 'on-shell' within an electromagnetic field, beamstrahlung photons are also a source for low energetic e^+e^- pairs. The pair production via an interaction of a photon with the collective field of the oncoming bunch is called coherent pair production [109] while the production via an interaction with the field of an individual particle is called incoherent pair production [110]. The size of the beamstrahlung parameter, Υ, determines which mechanism overweighs the pair production process. For small values ($\Upsilon < 1$) the latter one dominates [103].

At TESLA with $\Upsilon \approx 0.03$ more than of 10^5 pair particles[5] are produced per BX. Three diagrams contribute to the incoherent pair production: Breit-Wheeler, Bethe-Heitler and Landau-Lifshitz (see Figure 5.3, for a detailed description see, for example [111]). The e^+e^- pairs carry a total energy of roughly 360 TeV (800 TeV) at a centre-of-mass energy of $\sqrt{s}$ =500 GeV (800 GeV). This amount of energy might be a crucial problem, in particular for the small ΔM analysis. The e^+e^- pair particles are less well collimated as the beamstrahlung photons and are partly deflected into the detector. However, due to their low energy they curl in the magnetic field and are constrained to rather low radii, so that especially the detector forward direction is affected which has a significant impact on the solid angular coverage usable for the ISR method. Even those e^+e^- particles which leave the detector through the beam pipe cannot be neglected since those particles are bent inside the quadrupol field of the final focusing magnet. The secondary particles (e.g. neutrons) produced by the deflected pair particles inside the magnet material are an additional background source. In the following Section computer simulation results are presented concentrating only on the primary e^+e^- particles.

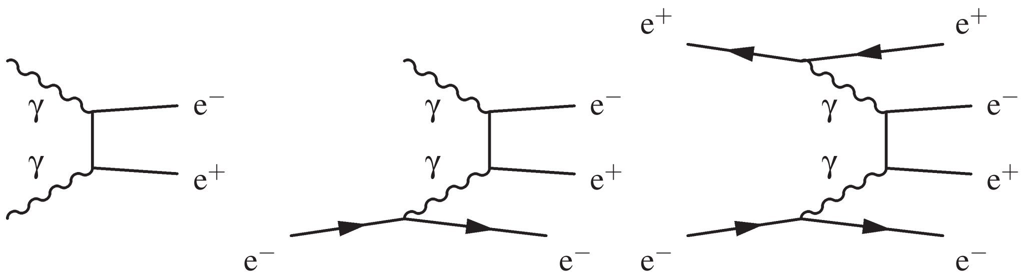

Figure 5.3: The incoherent pair production processes: Breit-Wheeler, Bethe-Heitler and Landau-Lifshitz (from left to right).

For sake of completeness the other beam induced background sources not directly related to beamstrahlung are listed below.

[5] counting only particles with energies above 5 MeV

Synchrotron Radiation

Photons are also emitted within the final focus system. This synchrotron radiation has to be collimated before it produce further hits. Synchrotron radiation emitted in the final doublet of magnet optics cannot be collimated. One has to assure that these photons can leave the the detector on the opposite side.

Beam-gas Interactions

In order to reduce beam-gas interactions the vacuum system and the beam pipe are designed for a vacuum of 10^{-7} mbar.

Muon Background

Beam particles which hit collimators of the final focus system will also produce secondary particles. The muons among these secondaries will be detected as off-axis tracks in the detector if not shielded within the accelerator tunnel.

5.1.2 Pair Background and the TESLA Detector

Kinematics

The large amount of energy carried away by the pair particles might represent a severe problem for the lifetime of detector components and their performance. The histograms in Figure 5.4 show the energy spectrum, the transverse momentum and the angular distribution of the pair particles at the interaction point, simulated with Guinea Pig (see Section 3.3.2).

The scatter plot in Figure 5.5 shows that the $p_{\mathrm{T}}^{\mathrm{e}}$-$\theta^{\mathrm{e}}$ combinations of the pair particles are not evenly spread within the plane. Interesting to note are the two clusters of particles formed by the particles which are, depending on their charge, either focused or defocused within the field of the oncoming bunch. The maximum deflection angle, $\theta^{\mathrm{e}}_{\mathrm{max}}$, of a pair particle, which occurs in Figure 5.5 as a sharp cluster edge, depends on the energy of $E^{\mathrm{e}} = \varepsilon\frac{\sqrt{s}}{2}$ of the particle and can be written at first order [112]:

$$\theta^{\mathrm{e}}_{\mathrm{max}}(\varepsilon) = \sqrt{4\frac{\ln\left(\frac{D'}{\varepsilon}+1\right)D'\bar{\sigma}_x^2}{\sqrt{3}\varepsilon\sigma_z}} \tag{5.2}$$

where $D' = Nr_{\mathrm{e}}\sigma_z/(\gamma\bar{\sigma}_x^2)$ describes the disruption parameter for a round beam using an average beam dimension $\bar{\sigma}_x^2 = \langle\sigma_x\rangle$ and r_{e} is the classical electron radius. As already pointed out in [113] a few pairs will already be produced with large intrinsic angles. These particles are also shown in the scatter plot Figure 5.5 as dots above the maximum angle edge.

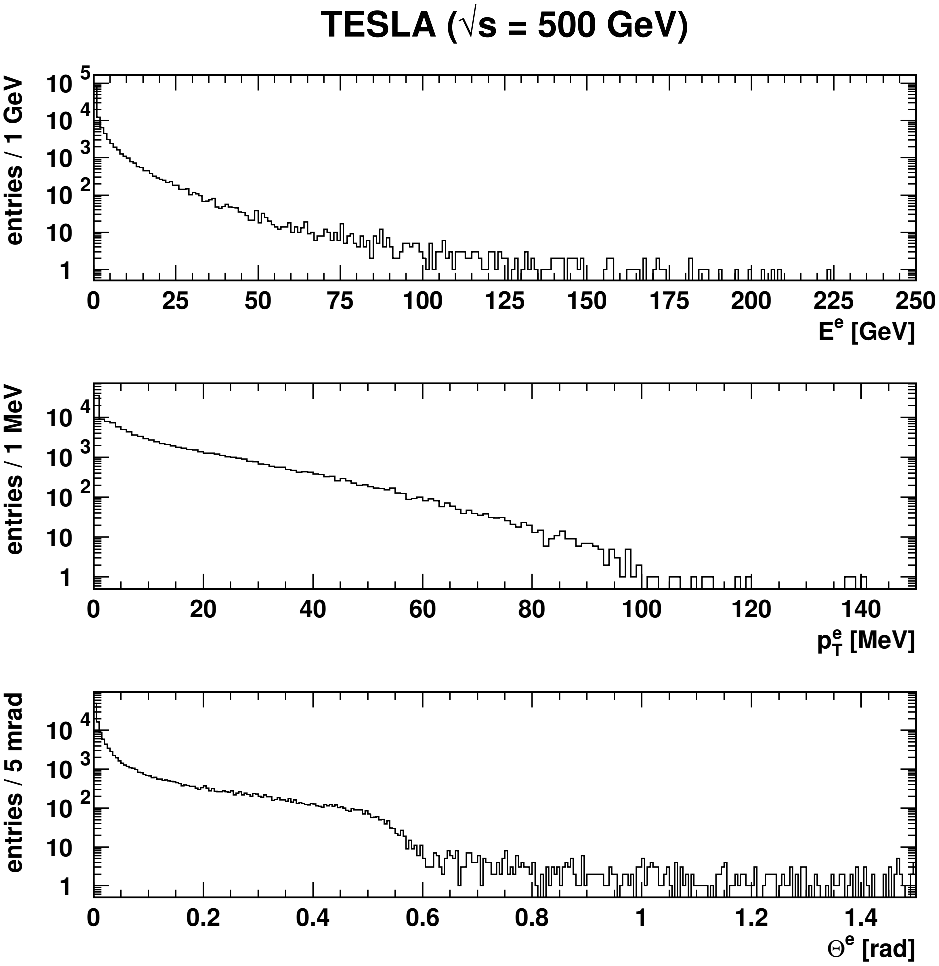

Figure 5.4: Energy spectrum, transverse momentum and polar angular distribution of all pair particles produced in one BX by beamstrahlung.

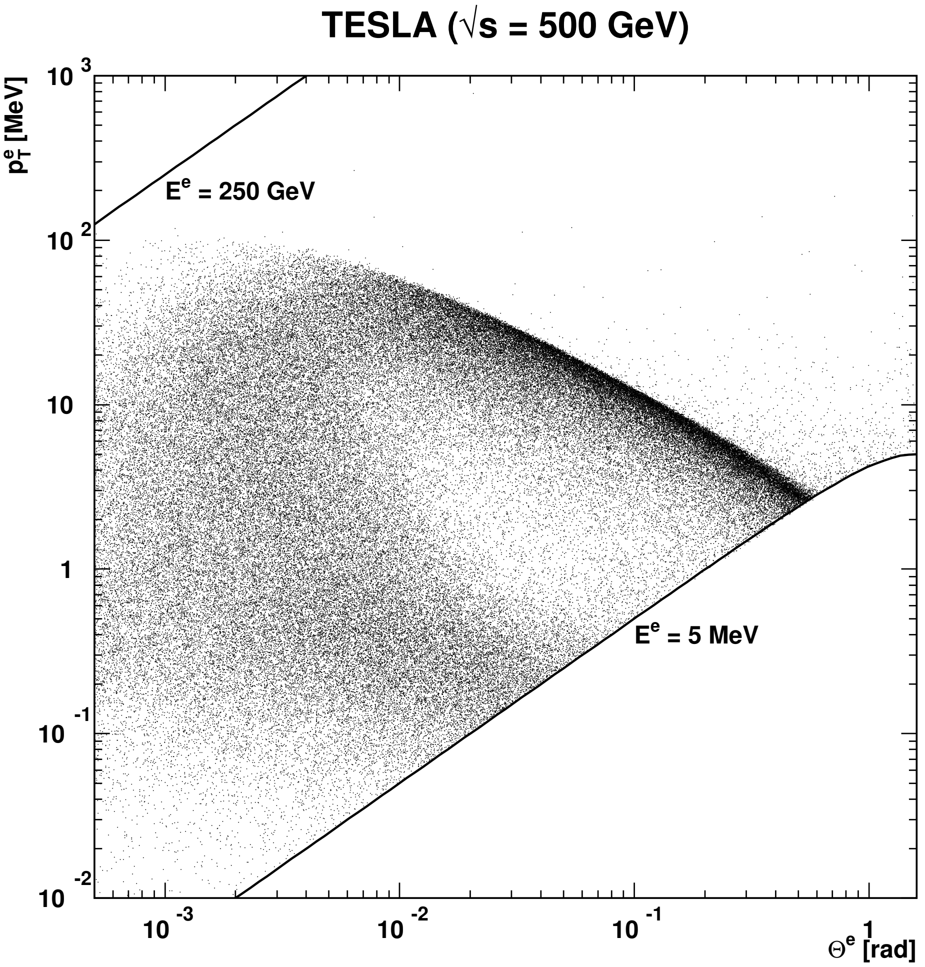

Figure 5.5: Transverse momentum p_T^e versus polar angle θ^e of all pair particles produced in one BX via incoherent pair production. The lines indicate maximum and minimum particle energy. The accumulation of particles in the lower left corner represents all particles focused within the field of the incoming bunch. Particles with the same charge as the particles of the oncoming bunch are defocused and form the sharp edge slightly above the centre.

Within its magnetic field the pair particles will traverse the detector on helix-like tracks[6]. The longitudinal momentum, $p_{\mathrm{L}}^{\mathrm{e}}$, and the transverse momentum $p_{\mathrm{T}}^{\mathrm{e}}$, are needed to describe the particle track (see Figure 5.6). The helix radius, R, and the helix pitch, D, of a particle with the electric charge e within a magnetic field, B, is given as:

$$R = \frac{p_{\mathrm{T}}^{\mathrm{e}}}{eB} \tag{5.3}$$

$$D = \frac{2\pi p_{\mathrm{L}}^{\mathrm{e}}}{eB} \tag{5.4}$$

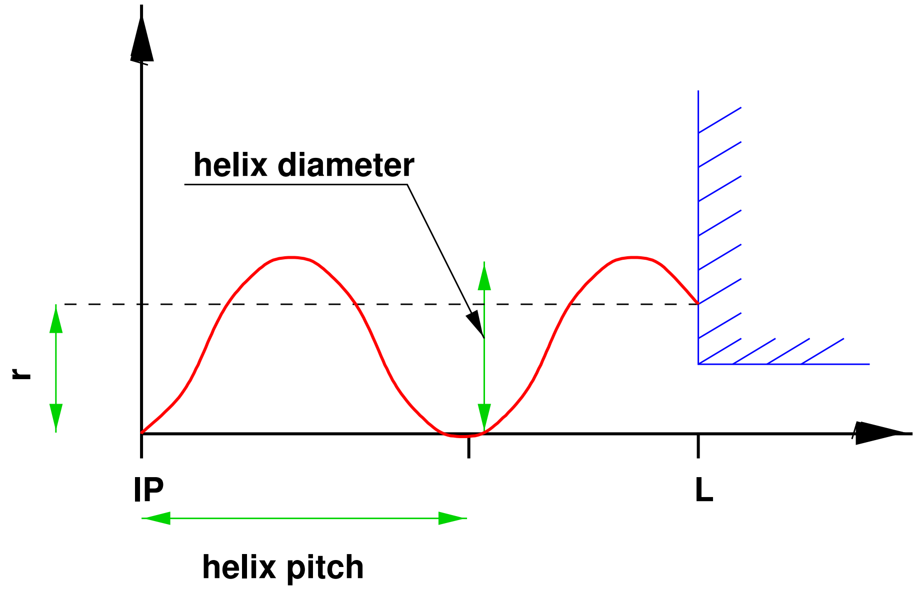

Figure 5.6: Illustration of a helix track of a pair particle hitting a detector component at a distance L from the interaction point, IP, at a radius r.

Equivalently, the transverse momentum $p_{\mathrm{T}}^{\mathrm{e}}$ and the polar angle θ^{e} can be used for the description of R and D. Based on the $p_{\mathrm{T}}^{\mathrm{e}}$-$\theta^{\mathrm{e}}$ distribution of the pair particles and using Equation (5.3) and Equation (5.4) the vertical distance to the beam axis of each pair particle as a function of the distance to the interaction point (IP) can be calculated. Figure 5.7 shows the envelope of the pair particles. It is defined as the minimum vertical distance to the beam axis which is greater or equal as the maximum vertical distance to the beam axis of 99 % of the pair particles. In order to reduce particle showers the beam pipe should at least enclose this envelope.

[6] Assuming a homogeneous magnetic field and that the particles do not lose energy on their way the helix radius is fixed.

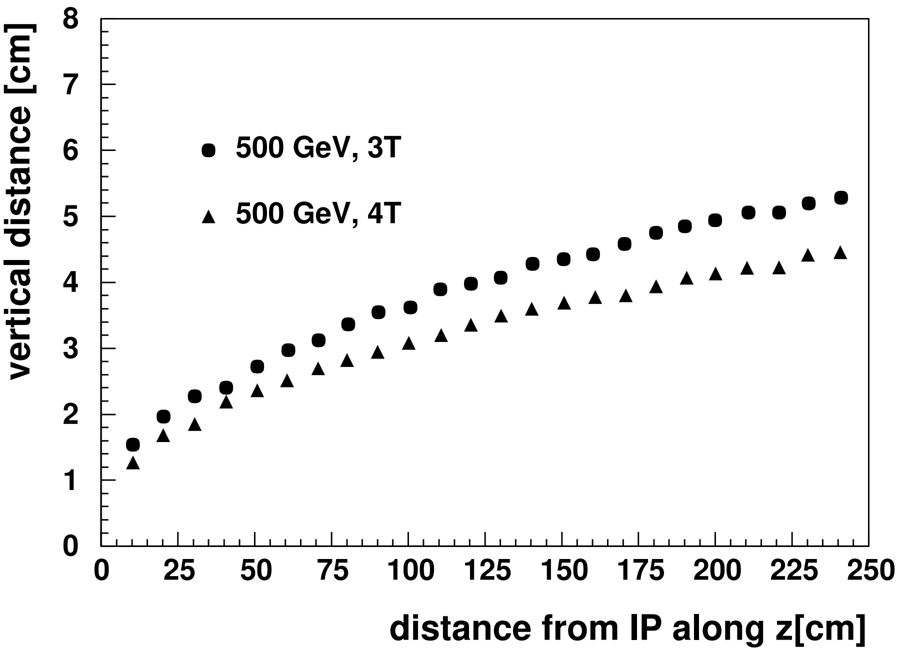

Figure 5.7: The envelope of the pair particles produced via incoherent pair production as a function of the distance to the IP. The envelope is defined as the minimum vertical distance to the beam axis which larger or equal as the maximum vertical distance to the beam axis of 99 % of the pair particles. Clearly visible the effect of the magnetic field. A larger magnetic field forces the pair particles on smaller radii, the envelope becomes smaller.

Detector Performance

The influence of pair particles on the innermost layer off the VTX is illustrated in Figure 5.8. It shows the expected hit density at various radii as a function of the z-coordinate within a magnetic field of 3 T. It varies from $O(0.1\,\mathrm{hits/mm^2BX})$ at $|z| \lesssim 7.5$ cm to $O(0.7\,\mathrm{hits/mm^2BX})$ at $|z| \gtrsim 10$ cm for a layer radius of 1.2 cm. The hit densities are even smaller for larger radii and are as small as $O(0.2\,\mathrm{hits/mm^2BX})$ at $|z| \gtrsim 10$ cm for a layer radius of 1.5 cm. The sharp edge in the hit density distribution at $|z| \approx 7.5$ cm is due to the slope of the envelope. It is obvious that, for example, for a CCD VTX, as proposed in [41], with an active pixel density of 2500 pixel/mm^2 the resulting detector occupancy has basically no effect on the detector performance.

However, as shown in Figure 3.8 the structure of the layer geometry of the CCD-based VTX is adjusted to the hit density distribution. The first layer is situated at a radius of $r = 1.5$ cm and its length ranges from $|z| \lesssim 5$ cm. The layers at radii of $r = 2.6,\ 3.7,\ 4.8$ and $6.0\ cm$ are longer and reach $|z| \approx 12.5$ cm.

Figure 5.9 summarises the number of hits per layer and BX for the CCD-based VTX. One should mention that the hits are produced by only a couple of pair particles ($O(20-30)$), mainly particles which are produced with large intrinsic angles, which curl several times through the same layer. The overall effect on the VTX and its performance is negligible.

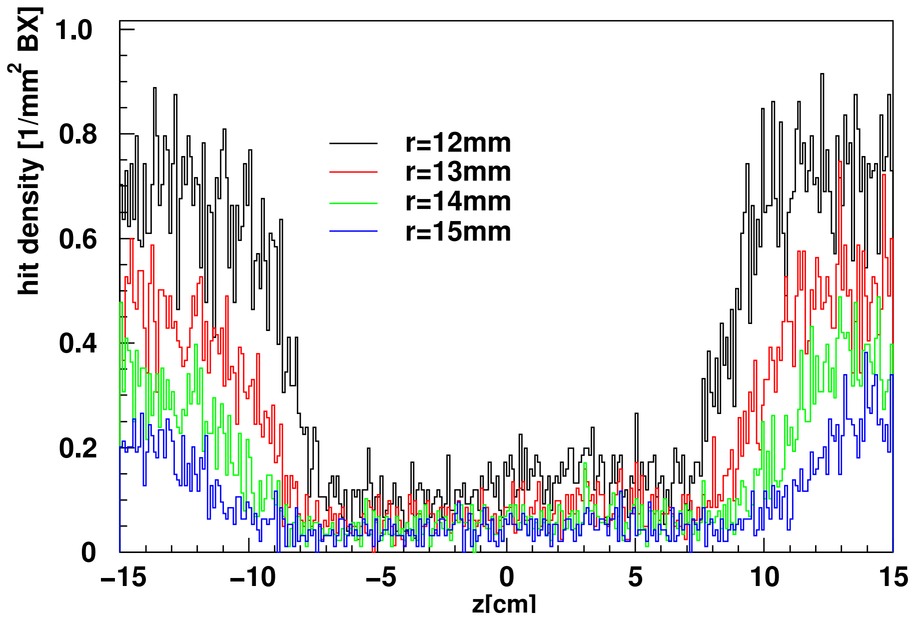

Figure 5.8: Hit density of pair particles produced by beamstrahlung at various radii from the beam pipe at a function of the z-coordinate. The magnetic field was set to 3 T.

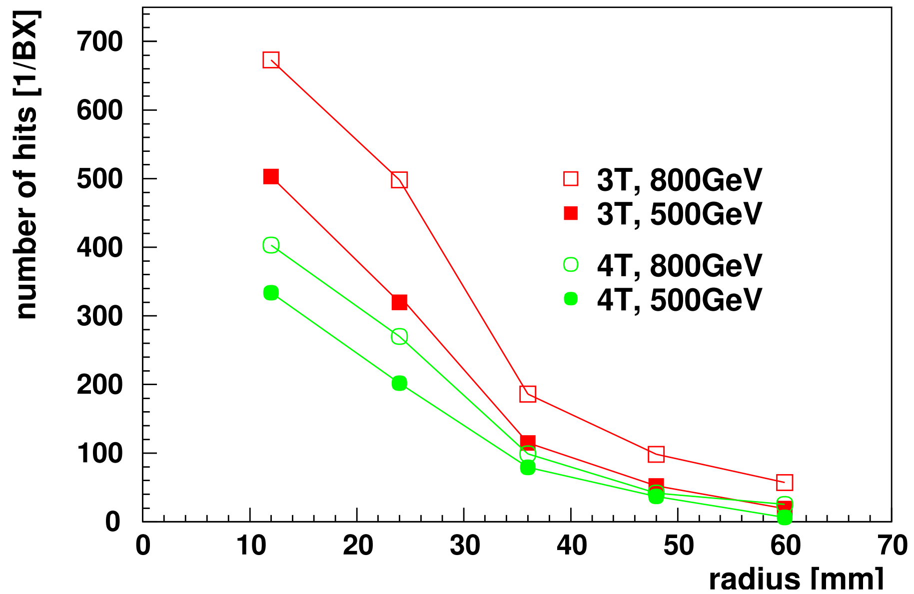

Figure 5.9: Number of hits of pair particles produced by beamstrahlung per BX in the five layers of the VTX. VTX layout as proposed in [114].

Further downstream the effect of the pair particles on the detector is more severe. As shown in Figure 5.10 the pair particles dump a total energy of several tens of TeV per BX outside a radius of $r = 0.9\,\text{cm}$ at distance of $d = 2.1\,\text{m}$ from the IP. Notable is the sharp drop in the distributions at $r \approx 5\,\text{cm}$. It is a relic from the particular p_T^e-θ^e distribution of the pair particles at production time shown in Figure 5.5.

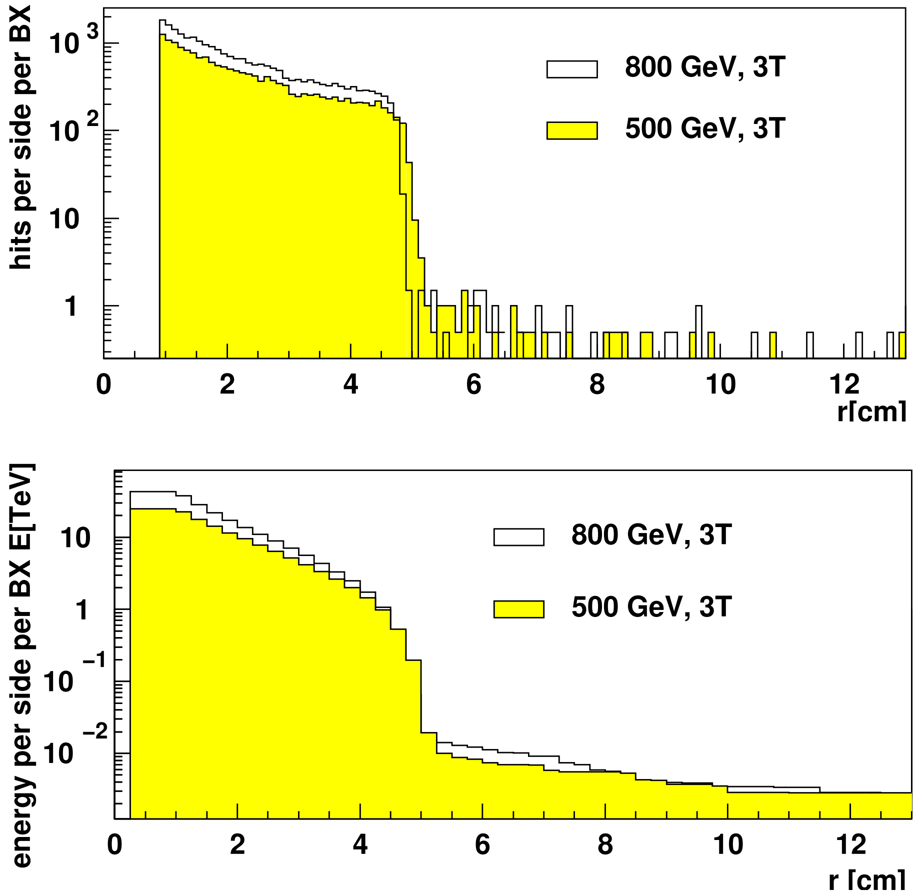

Figure 5.10: Hit distribution and energy sum of all pair particles produced in one BX via incoherent pair production outside a radius r at a distance of $d = 2.1\,\text{m}$ from the IP. The sharp drop in the distributions at $r \approx 5\,\text{cm}$ is a relic from the particular p_T^e-θ^e distribution of the pair particles at production time shown in Figure 5.5.

In one of the first TESLA detector design iterations [114] the forward region at this position was envisaged as illustrated in Figure 5.11. A system of three masks is noticeable. The masks were proposed in order to protect the detector from backscattering secondaries produced by the large amount of pair particles. In Figure 5.12 the number of hits per BX of secondary particles at the inner side of the conical mask is plotted. Most of the particles hit the conical mask at the position around the LCAL. These are shower particles leaking into the mask. The amount of particles hitting the mask in front of the LCAL is small and the conical nose of the mask seems to be redundant. Extensive studies [108] showed that although the mask proposal fulfils its purpose a redesign was desirable. Especially the conical shaped mask should be subject to revision. Its benefit does not nearly balance the fact that it introduces a dead spot inside the detector between the ECAL and the, at that time called, LCAL component. The wish for better angular coverage led to a complete redesign of the forward region.

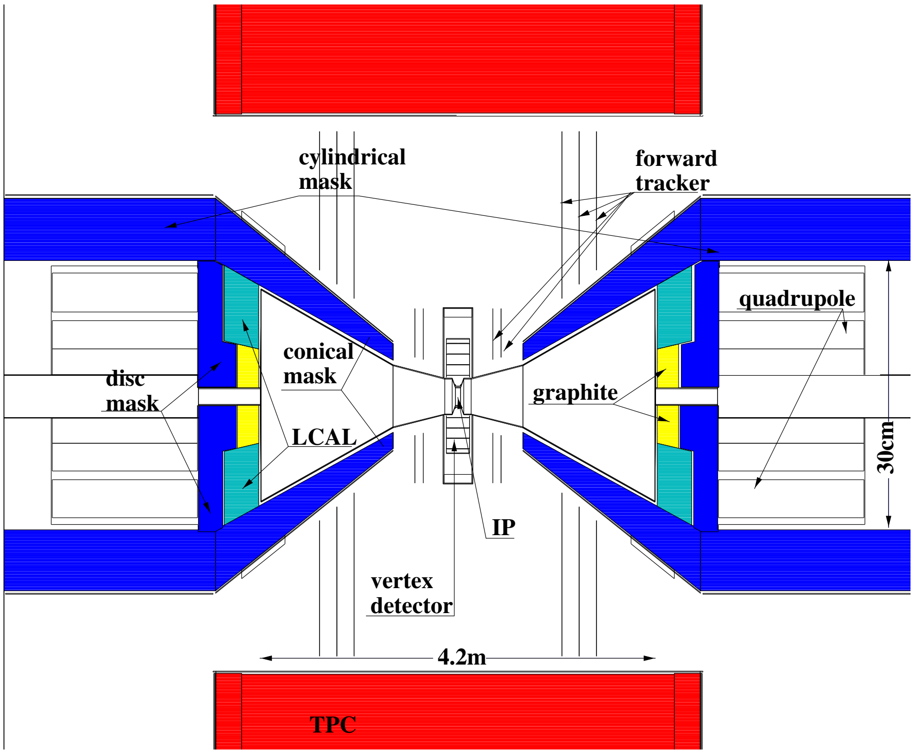

Figure 5.11: Design of the forward region as proposed in [114].

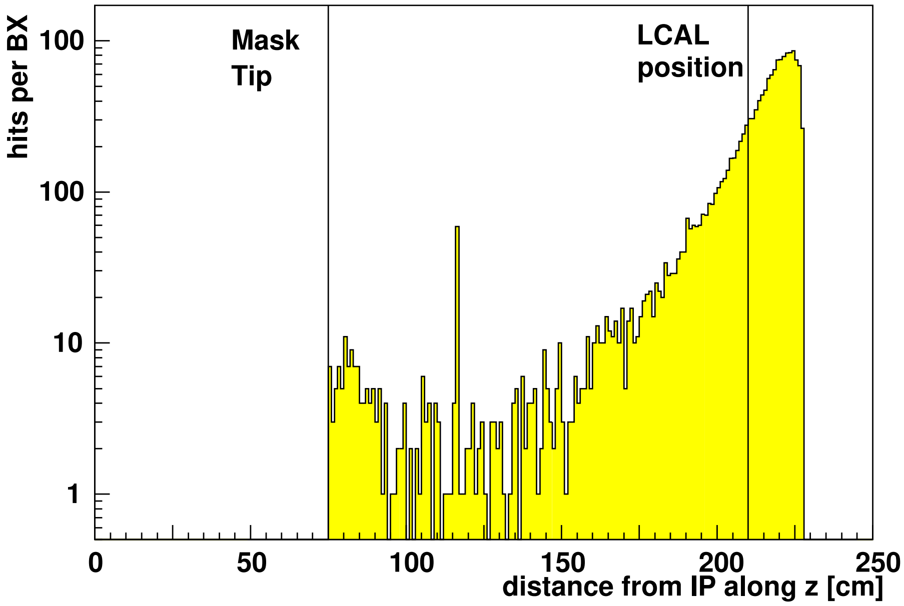

Figure 5.12: Number of hits per BX of secondary particles originating from pair particles produced via incoherent pair production at the inner side of the conical mask. The distribution corresponds to $\sqrt{s} = 500\,\mathrm{GeV}$ and $B = 3\,\mathrm{T}$. The vertical lines indicate the tip of the mask and the position of the LCAL.

The currently preferred [41] forward region layout was already discussed in Section 3.2.2 and is shown again in Figure 5.13. Parts of the conical mask remained in the new layout but the complete tip of the mask was replaced by the LAT filling the sensitivity gap between ECAL and LCAL. For the new design the envelope of the pair particles and the hit distribution at the position of the LCAL was taken into account. Making use of the sharp edge in this distribution one assures that more or less all particles hit the plane enclosed by the LCAL diameter. Since the number of pair particles and their energy is very sensitive to luminosity variations within one bunch train the LCAL signals can be used as a feedback for the beam delivery system in order to tune the beam [71]. For high energetic particles the LCAL may even serve as a low angle calorimeter providing an angular coverage down to 4.6 mrad. The LAT is not affected by the pair particles and allows energy measurements down to 27.5 mrad in a very clean environment.

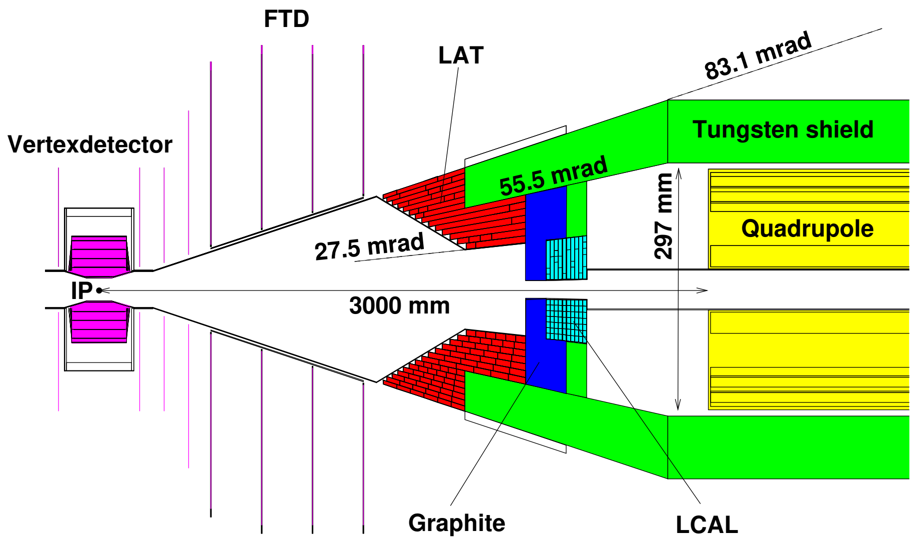

Figure 5.13: The redesigned TESLA forward and mask region (see also Figure 5.11).

The r-ϕ distribution of the energy sum of all pair particles produced in one BX via incoherent pair production hitting the surface of the LAT and the LCAL is shown in Figure 5.14. The energy distribution is asymmetric in ϕ and results from the flat beam cross-section. Averaging over all ϕ-segments leads to the radial energy energy distribution depicted in Figure 5.15. The corresponding energy deposition in the active layers of the LAT and LCAL is depicted in Figure 5.16. The electromagnetic showers produced by the pair particles reaches its maximum (in terms of deposited energy) in the eighth (fourth) layer in the LCAL (LAT).

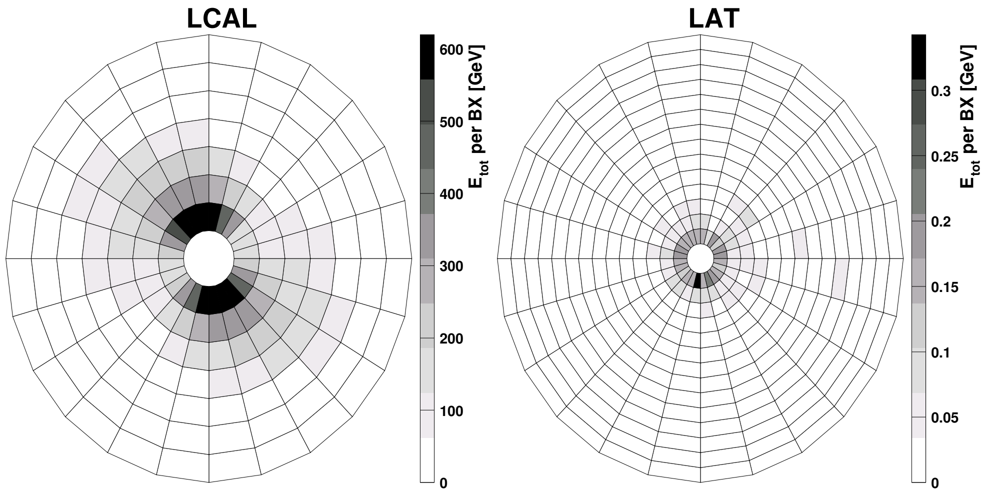

Figure 5.14: Distribution on the radial and azimuthal segments of the total energy, E_{tot}, of all pair particles produced in one BX via incoherent pair production at $\sqrt{s}$ = 500 GeV hitting the surface of the LCAL (left) and the LAT (right). The magnetic filed was set to 4 T. The asymmetric energy distribution in ϕ results from the flat beam cross-section.

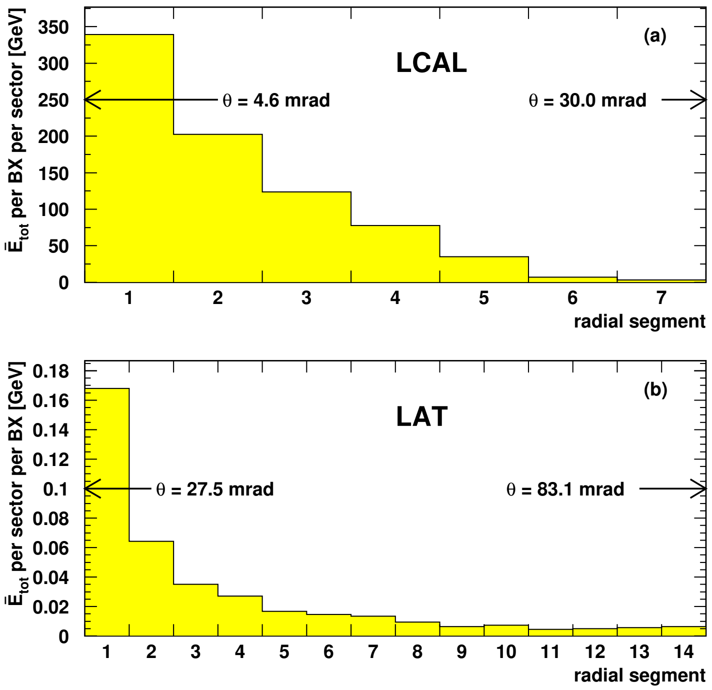

Figure 5.15: Radial energy distributions, $\bar{E}_{\text{tot}}$, of all pair particles produced by beamstrahlung at the surface of the LCAL and the LAT. The energy distributions were averaged over the all 24 sectors and 100 BXs. The magnetic field was set to 4 T.

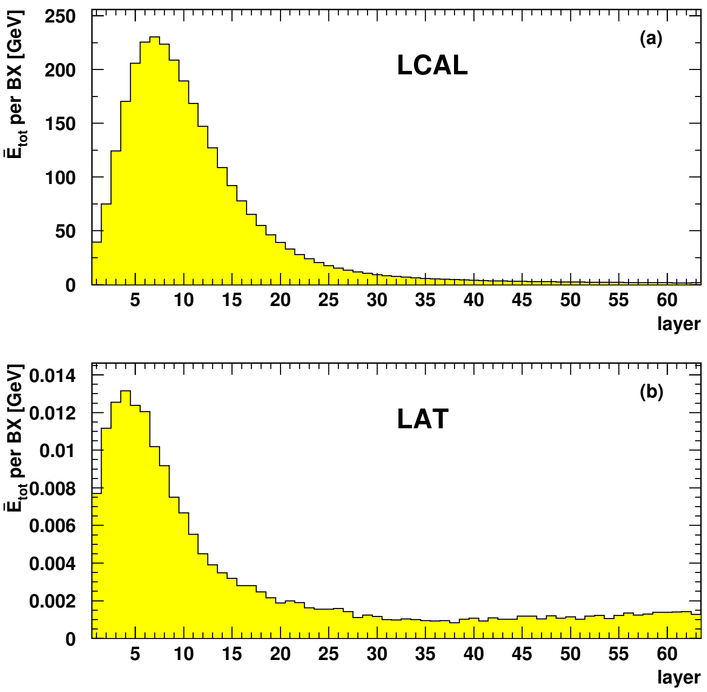

Figure 5.16: Energy deposition of all pair particles produced via incoherent pair production as a function of the LCAL (upper plot) and LAT (lower plot) layers. The first layer is the one close to the IP. The energy distributions show the sum of the energies deposited in all ϕ sectors and all radial sectors. The energy distribution of 100 BXs were averaged.

It is substantial for the ISR method to tag beam electrons from two-photon events up to energies of 250 GeV. The deposited energies from pair particles in the LAT are negligible and the energy of additional electrons from two-photon interactions is a clear electron signature. From the energy depositions in the LCAL it is not obvious that the same is true for the LCAL. A series of computer simulations were made to qualitatively test the LCAL behaviour. In a first step an average background energy deposition in the LCAL was calculated. A total of 100 TESLA BX was simulated and the energy deposition of the pair particles in the forward detectors was averaged. This information was used as 'expected' pair background signal. A two-photon sample at a centre-of-mass energy of $\sqrt{s}$ =500 GeV was produced with the BDK generator. To assure that at least one beam electron is scattered into the LCAL a cut was applied corresponding to Equation (2.9). In a next step the LCAL response to these electrons was computed and overlayed with the response of the LCAL to all pair particles produced in one BX. One example of a 106 GeV two-photon beam electron is shown in Figure 5.17 – Figure 5.19. By subtracting the expected background signal the track of two-photon beam electron inside the LCAL can be reconstructed.

Three further examples are illustrated in Figure 5.20 – Figure 5.22. Depicted are the deposited energies in the radial and layer segments for the ϕ sector of interest. The two-photon beam electrons can be easily identified not only by their larger shower depth.

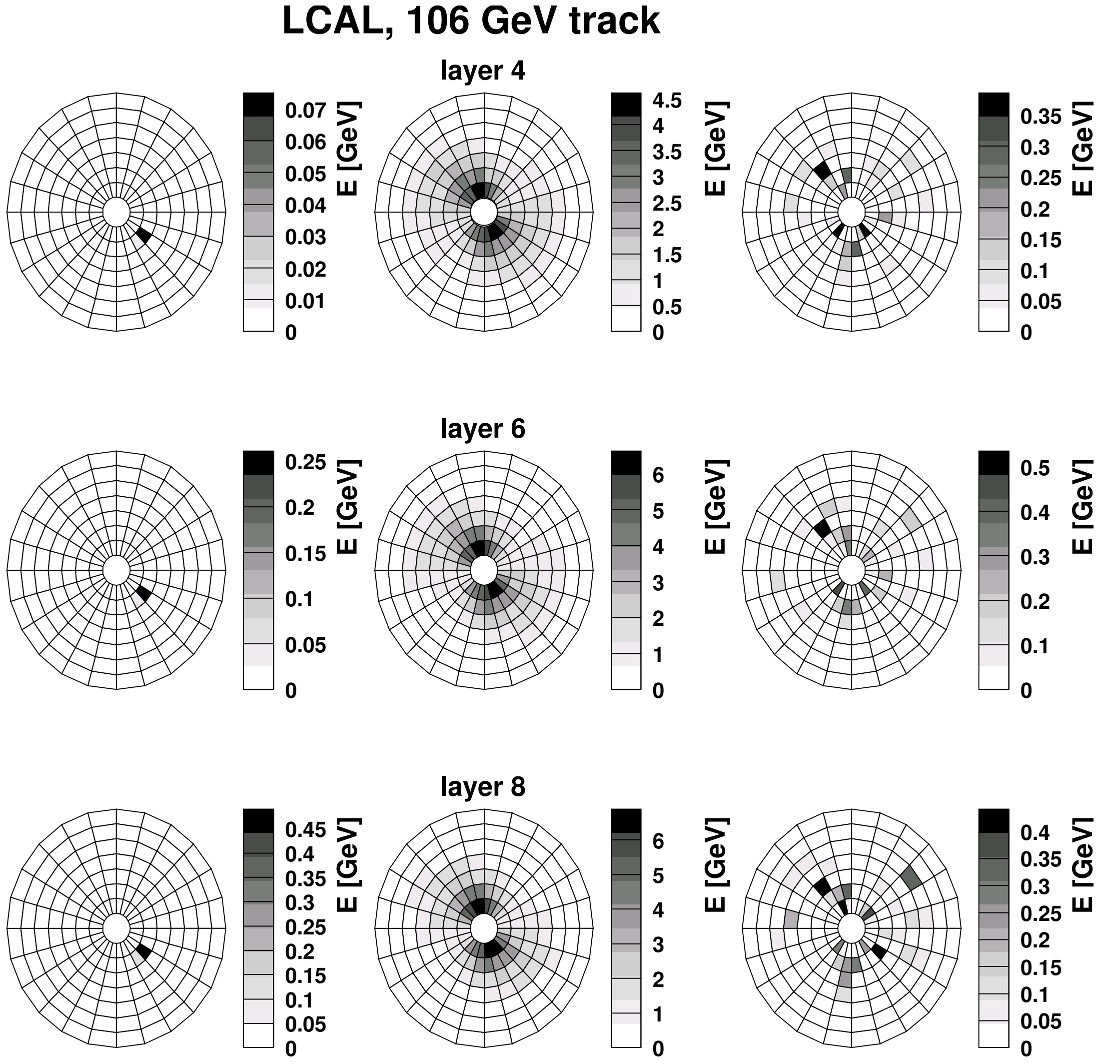

Figure 5.17: Energy distribution in r-ϕ in various layers (4, 6, 8) of the LCAL from a 106 GeV two-photon beam electron only (left column) and overlayed with the energy deposition from pair particles of one BX (middle column). The right column shows the energy distribution after subtracting an averaged (100 BX) energy distribution of pair particles. The two-photon beam electron is clearly visible. Additional distributions of other layers are shown in Figure 5.18 and Figure 5.19.

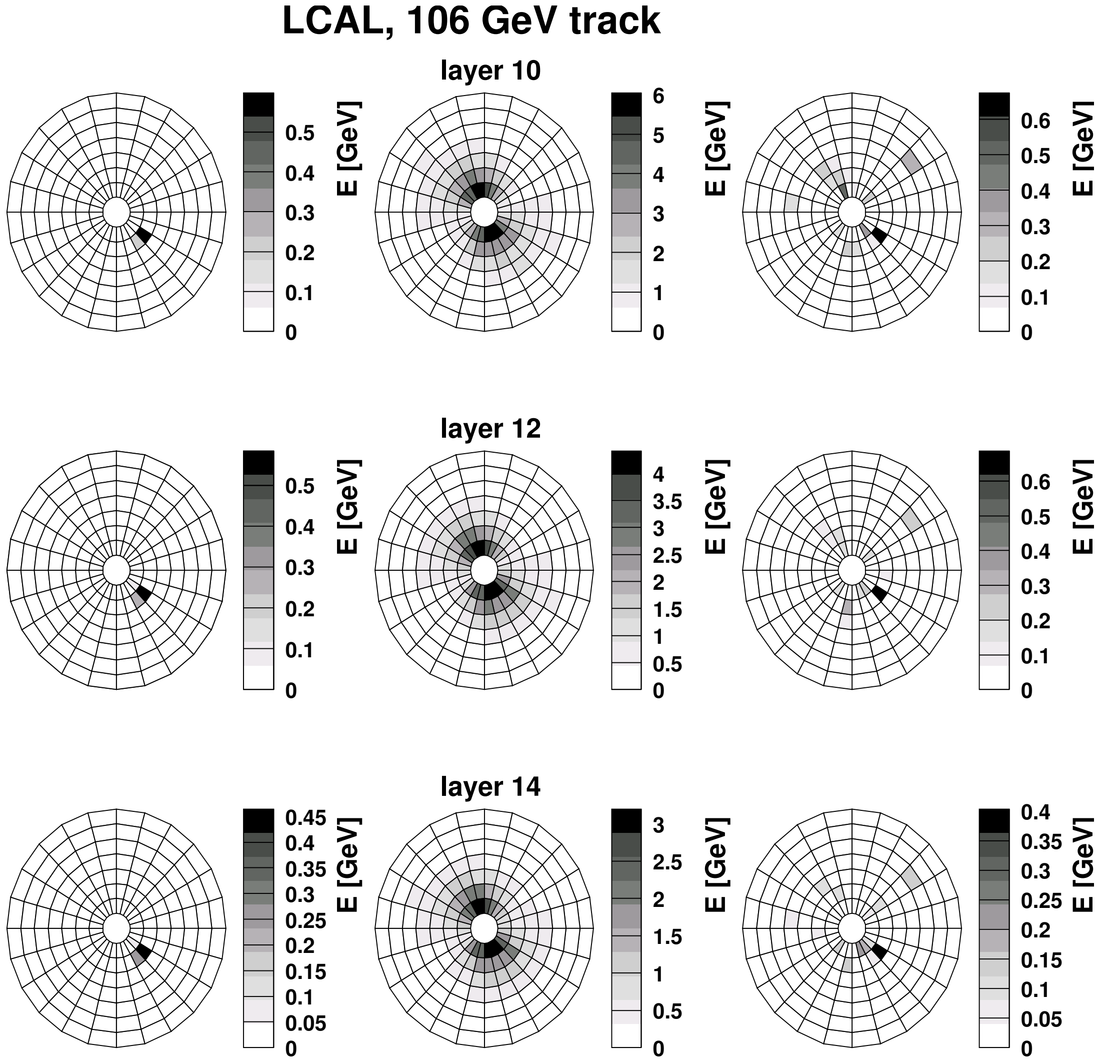

Figure 5.18: Energy distribution in r-ϕ in various layers (10, 12, 14) of the LCAL from a 106 GeV two-photon beam electron only (left column) and overlayed with the energy deposition from pair particles of one BX (middle column). The right column shows the energy distribution after subtracting an averaged (100 BX) energy distribution of pair particles. The two-photon beam electron is clearly visible. Additional distributions of other layers are shown in Figure 5.17 and Figure 5.19.

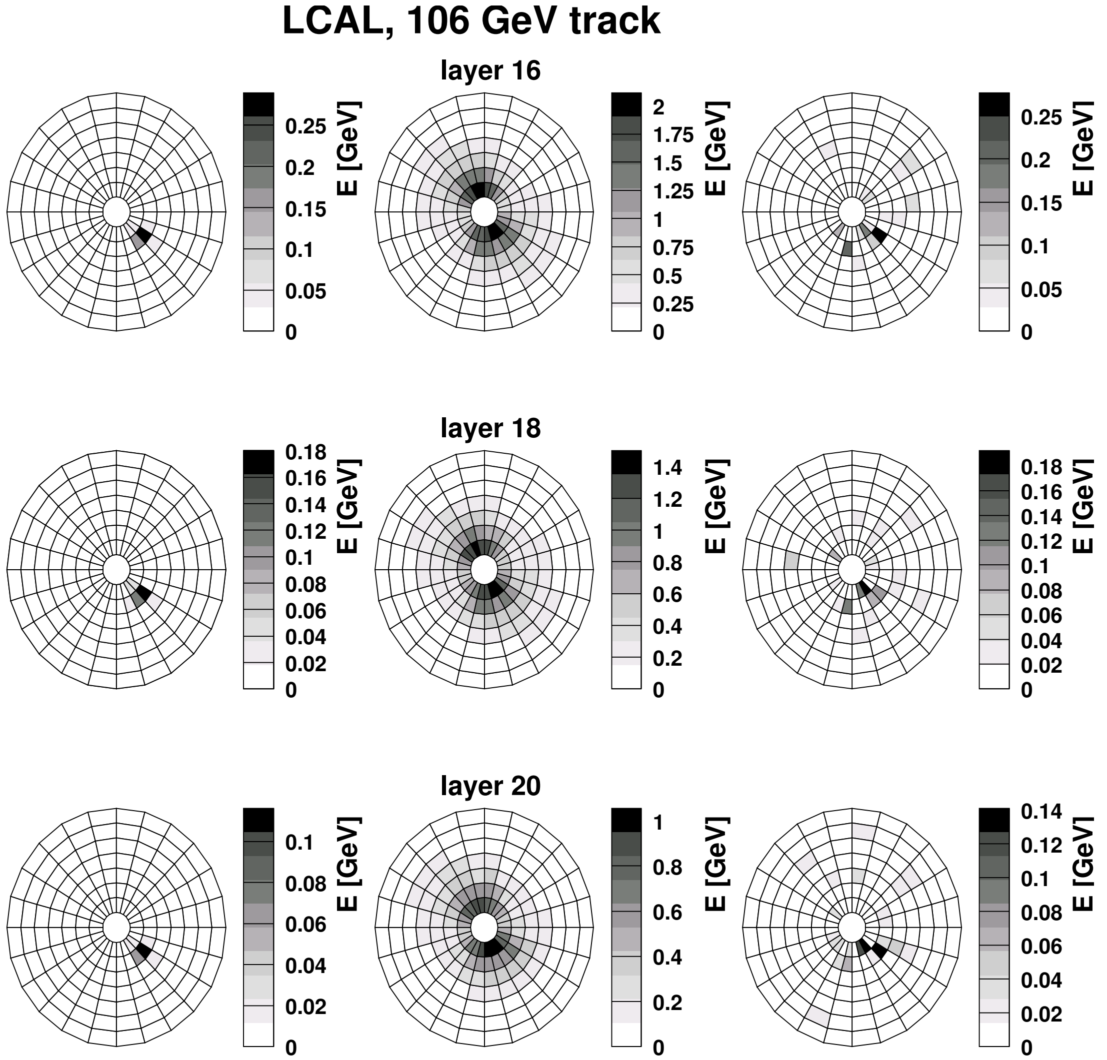

Figure 5.19: Energy distribution in r-ϕ in various layers (16, 18, 20) of the LCAL from a 106 GeV two-photon beam electron only (left column) and overlayed with the energy deposition from pair particles of one BX (middle column). The right column shows the energy distribution after subtracting an averaged (100 BX) energy distribution of pair particles. The two-photon beam electron is clearly visible. Additional distributions of other layers are shown in Figure 5.17 and Figure 5.18.

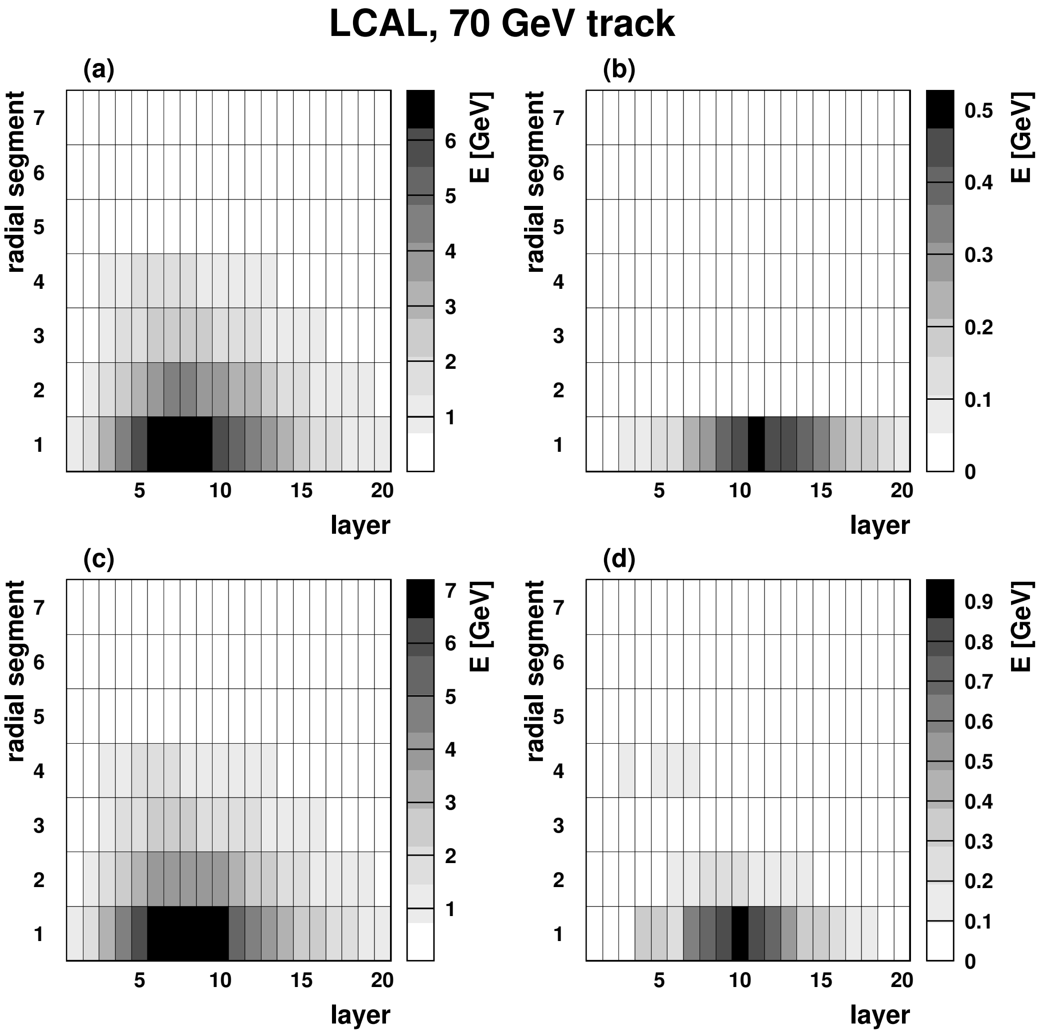

Figure 5.20: Radial and longitudinal energy deposition distribution of the pair background only (a), a 70 GeV two-photon beam electron only (b) and the energy sum of pair background and two-photon beam electron (c). The resulting energy distribution after subtracting the expected background energy deposition is depicted in (d). Shown is the ϕ segment of interest. Interesting to note that the beam electron can be identified even at a very low polar angles (first radial segment) and a rather moderate energy.

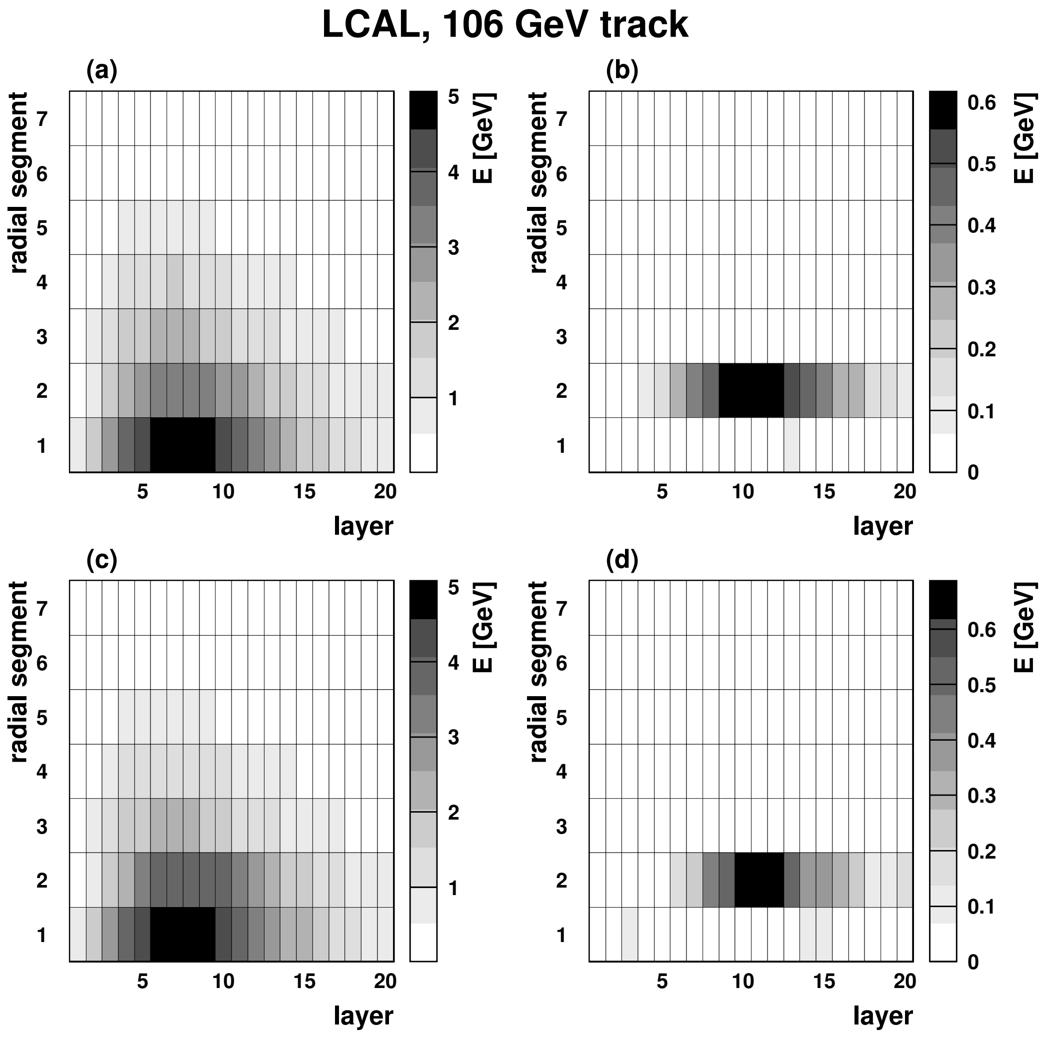

Figure 5.21: Radial and longitudinal energy deposition distribution of the pair background only (a), a 106 GeV two-photon beam electron only (b) and the energy sum of pair background and two-photon beam electron (c). The resulting energy distribution after subtracting the expected background energy deposition is depicted in (d). Shown is the ϕ segment of interest.

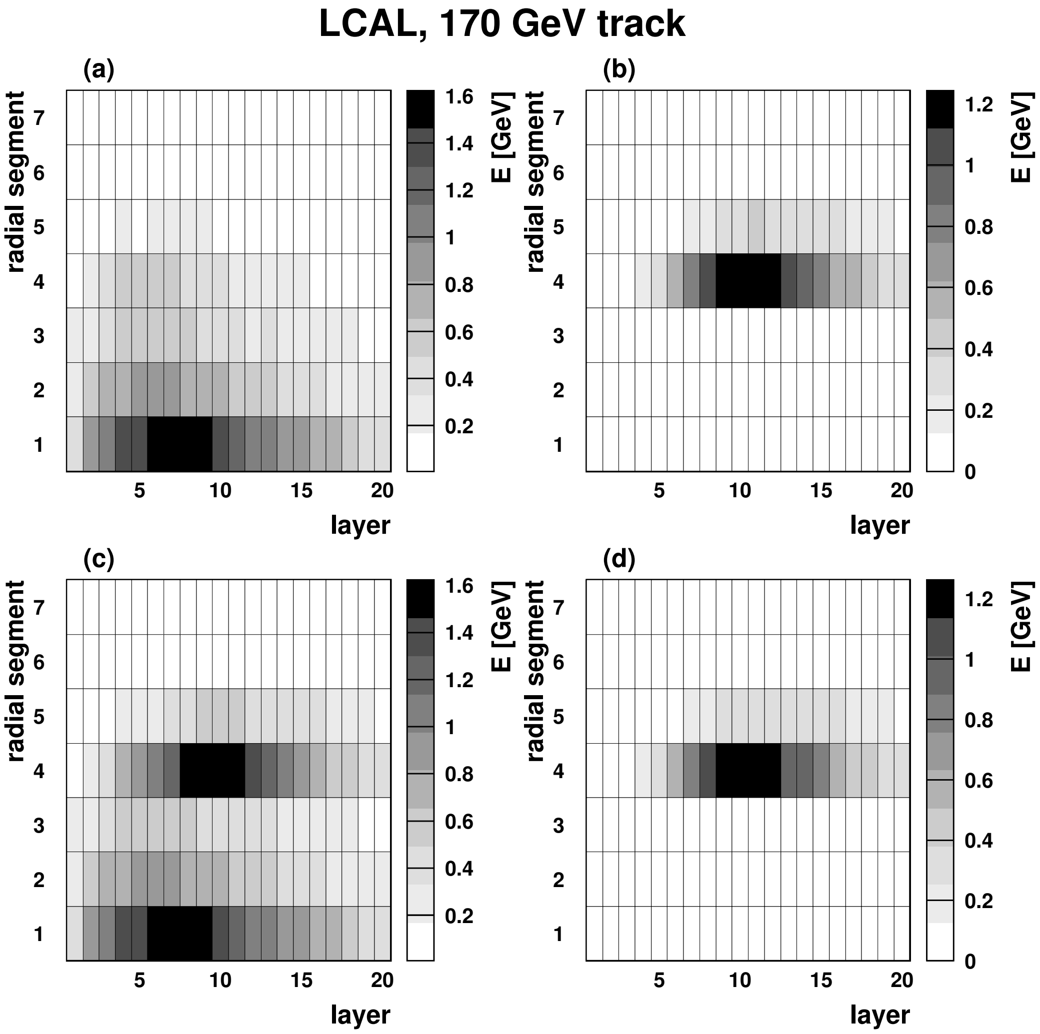

Figure 5.22: Radial and longitudinal energy deposition distribution of the pair background only (a), a 170 GeV two-photon beam electron only (b) and the energy sum of pair background and two-photon beam electron (c). The resulting energy distribution after subtracting the expected background energy deposition is depicted in (d). Shown is the ϕ segment of interest. In this case the energy of the two-photon beam electron is large enough that it can be identified even without subtracting the background contribution.

The shown examples are very promising and the LCAL performance seems to be good enough to identify even single high energy particles. However, for a final statement on the LCAL tagging probability more quantitative studies are needed which go beyond the scope of this thesis. The development of LCAL cluster and track finding algorithms is essential as well as a detailed study of the LCAL granularity and possible fluctuations of the pair particle background. For the in the following presented studies only the LAT was considered as tagging device, bearing in mind that this is a rather conservative assumption.

5.2 The Physics Study

5.2.1 The Time after Tevatron and LHC

The next place to look for the discovery of new particles is the Tevatron. Until the turn on of the LHC the Tevatron will be the machine with the highest centre-of-mass energy ever reached. At least the discovery potential of the LHC is large enough to unveil SUSY if it is realised at low energies. Due to the large centre-of-mass energy, it will be possible to detect SUSY particles at the LHC. Mass determinations with an accuracy of a few percent are envisaged. However, most of the underlying SUSY parameters will not be accessible at the LHC. Only at lepton colliders like TESLA precision measurements of SUSY particles widths and branching ratios, the determination of couplings, the extraction of mixing parameters and measurement of measurement of CP violating phases will be possible.

Figure 5.23 shows examples of mass spectra for three SUSY breaking scenarios. They represent typical spectra which can be considered as starting point for a TESLA study. In each scenario the lightest charginos and neutralinos have masses between 100 and 200 GeV. As indicated the AMSB scenario is a good candidate for the ISR method. A study was carried out to test to which extent chargino and neutralino masses in this mass region can be measured at TESLA using the ISR method.

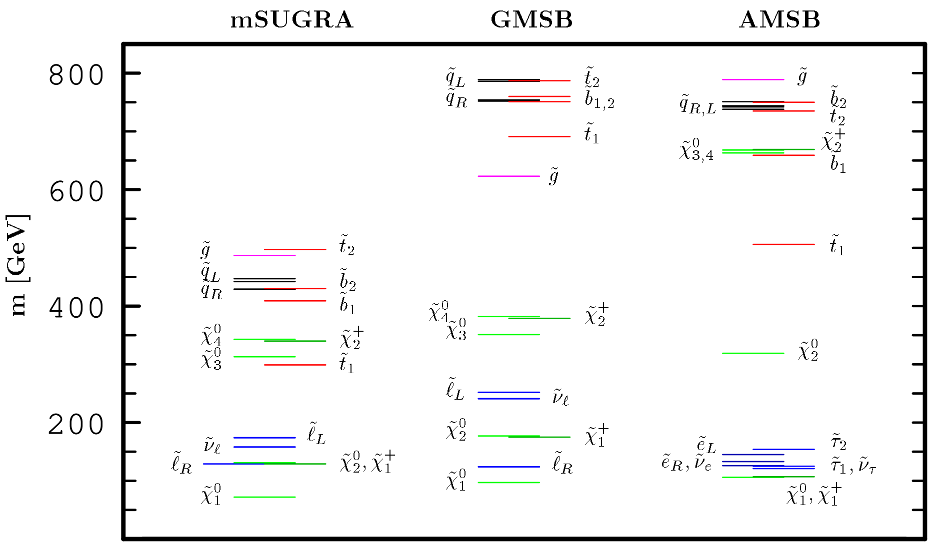

Figure 5.23: Examples of mass spectra in mSUGRA, GMSB and AMSB models for $\tan\beta = 3$, $\mathrm{sign}\mu > 0$. The other parameters are $m_0 = 100\,\mathrm{GeV}$, $m_{1/2} = 200\,\mathrm{GeV}$ for mSUGRA; $M_{\mathrm{mess}} = 100\,\mathrm{TeV}$ $N_{\mathrm{mess}} = 1$, $\Lambda = 70\,\mathrm{TeV}$ for GMSB and $m_0 = 200\,\mathrm{GeV}$, $m_{3/2} = 35\,\mathrm{TeV}$ for AMSB [41].

5.2.2 Monte Carlo Samples and Detector Simulation

The choice of the SUSY scenario was driven by the Snowmass Points and Slopes,SPS , benchmark scenarios[7]. The SPS 9 point describes an AMSB oriented SUSY scenario with almost degenerate charginos and neutralinos with masses around 170 GeV and a mass difference in the order of $O(0.5\ GeV)$. For this study a chargino mass of $M_{\tilde{\chi}_1^\pm} = 172$ GeV and a mass difference of $\Delta M = 0.4$ GeV was chosen. The signal Monte Carlo Samples were generated using SUSYGEN as described in Section 3.3.2 and the input parameters were chosen according to the SPS 9 proposal. The polar angle of the ISR photon was required to lie in the TESLA ECAL angular coverage ($|\cos\theta^\gamma| < 0.996$). Table 5.1 summarises the used parameter set and the corresponding chargino mass and mass difference.

parameter	value
M_1/M_2	2.0
μ	< 0
$\tan\beta$	1.5
$M_{\tilde{\nu}}$	310 GeV
$M_{\tilde{\chi}_1^\pm}$	172 GeV
ΔM	0.4 GeV
σ	0.218 pb

Table 5.1: Parameters describing the chosen SUSY scenario for the TESLA study.

Physics background, that is to say non machine related background, was not considered for this study . Extrapolating from LEP experiences background-free measurements were assumed. Nevertheless, the large luminosity at TESLA might lead to sizeable effects of small background contributions, which played only a subordinate role at LEP. The overlap of events, e.g. $e^+e^- \to \gamma Z^\star \to \gamma\nu\bar{\nu}$ events with $M_{Z^\star} \gg M_{Z^0}$ overlapping with $e^+e^- \to e^+e^-\gamma^\star\gamma^\star \to e^+e^-\pi^+\pi^-$ events, is only one example for this class of processes. On the other hand, the large amount of accumulated luminosity will still allow to increase the cut on the transverse energy of the ISR photon (Equation (2.9)) which simply will reduce a possibly increased background level due to a reduction of the available phase space while a good fraction of the selected signal sample will be retained.

All Monte Carlo samples were produced at centre-of-mass energies of $\sqrt{s} = 500$ GeV. The considered accumulated TESLA luminosity was 500 fb $^{-1}$. In the following the phrases data or data sets will be used to describe the simulated TESLA measurement while samples with multiple TESLA statistics will be regarded in terms of Monte Carlo samples.

SIMDET [93] (see Section 3.3.2) was used for the detector simulation. The magnetic field was set to 4 T. If not explicitly mentioned a minimal accessible angle within the detector of $\theta_D^{min} = 30$ mrad (well within the LAT coverage) was assumed.

[7] At Snowmass 2001 [45] a consensus was reached to define a list of SUSY models as benchmarks to be investigated in future collider studies. Various scenarios, so-called Snowmass Points and Slopes (SPS), were proposed in terms of a few parameters describing ‘typical’ to ‘extreme’ R_P conserving supersymmetry breaking mechanisms of mSUGRA, GMSB and AMSB. A complete description of all scenarios can be found in [115].

5.2.3 Measuring the Chargino Mass

Starting from a signal selection as discussed in Chapter 4 only two parts of a selected event can be used to extract information of the chargino and the neutralino mass. While the visible decay products and the reduced visible energy, E_{vis}, carry information on the mass difference, the ISR photon and its energy, E^{γ}, are related to the chargino mass. From the energy of ISR photon the recoil mass, M_{rec}, of the photon can be derived as follows:

$$M_{\mathrm{rec}}^2 = s - 2\sqrt{s}E^{\gamma}. \tag{5.5}$$

The recoil mass can be interpreted as the invariant mass, $M_{\chi^+\chi^-}$, of the chargino system. It is obvious that the recoil mass has to be at least twice the chargino mass. At this threshold the charginos are produced in rest. The double chargino mass, $2 \times M_{\tilde{\chi}_1^\pm}$ can be identified as the starting point of this spectrum. Interesting to note that only detector effects can smear out the M_{rec} in the direction of lower values. The additional radiation of beamstrahlung photons will shift the threshold to larger values, only.

Taking into account only ECAL resolution effects an estimate of the expected error, $\Delta M_{\tilde{\chi}_1^\pm}$, on the measured chargino mass can be derived: With Equation (5.5) the energy of ISR photons at the threshold for a chargino mass of $M_{\tilde{\chi}_1^\pm}$=172 GeV can be calculated to $E^{\gamma} \approx 132$ GeV. The TESLA ECAL energy resolution is given by Equation (3.8) and thus the error on the ISR photons at the threshold is $\Delta E^{\gamma} \approx 2.5$ GeV. This error propagates through the M_{rec} calculation and the chargino mass can be derived with an accuracy of $\Delta M_{\tilde{\chi}_1^\pm} \approx 1.8$ GeV. Typically, only a few events accumulate around the threshold and the threshold method should suffer from an additional non-negligible statistical error.

Using the information contained in the shape of the M_{rec} spectrum leads to a more precise measurement of the chargino mass. Figure 5.24 compares the recoil mass spectrum of the TESLA measurement and two Monte Carlo samples with different chargino masses. Although detector effects smear out the threshold, the dependency between threshold position and chargino mass is clearly visible.

The shape of the spectrum, especially the middle part is to first order linear. A simple straight line fit can be used to derive the chargino mass. The fitted curve is described by the slope, m, and the intercept, b. With these two parameters the fitted chargino mass, M_{fit}, is given as:

$$M_{\mathrm{fit}} = -\frac{b}{2m} \tag{5.6}$$

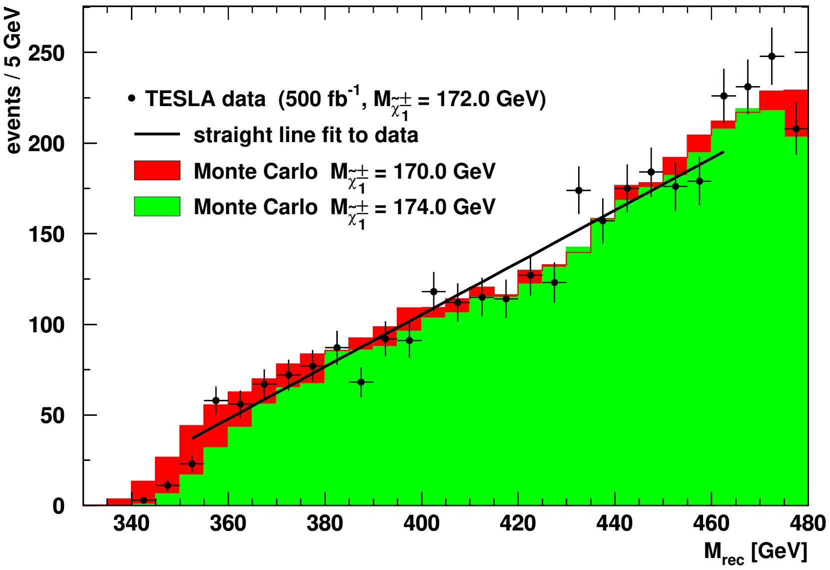

Figure 5.24: ISR photon recoil mass spectrum. The TESLA data are indicated by points with error bars (statistical error). The shaded histograms correspond to Monte Carlo simulations with two different chargino masses. The middle part of the spectra a in first linear. A straight line fit to the data points is indicated by the thick line. The slope and the intercept of the line can be used to extract the chargino mass as described in the text.

A couple of Monte Carlo samples with different chargino masses, ranging from 170 GeV to 174 GeV, were produced in order to derive a calibration curve which connects the fitted chargino mass and the true chargino mass, M_{true}. The result is shown in Figure 5.25. The linear dependency between M_{fit} and M_{true} was interpolated with straight line fit. Together with a fit to the data recoil mass spectrum a chargino mass of 171.47 ± 1.79 GeV was extracted. The error of the result seems to be rather large, but contains statistical contributions as well contributions from detector effects and beamstrahlung. Taking into account the simpleness of the described method the result it is still reasonable. The size of the error depends on the used fit. A more refined fitting function of the recoil mass spectrum, accounting for detector effects and ISR energy spectrum characteristics will definitely improve the accuracy.

5.2.4 Measuring the Mass Difference

As mentioned before the visible decay products and their energy can be used to measure the mass difference, ΔM. At mass differences below 1 GeV the chargino branching ratios are dominated by decays via a single charged pion as shown in Figure 5.26.

The first step to extract ΔM is to identify the decay products, in this case the pions, and measure their energy, E_π. If the chargino mass is already known the pions can then be boosted into the restframe of the chargino system. The energy of the boosted pion, $E_\pi^\star$, is given by:

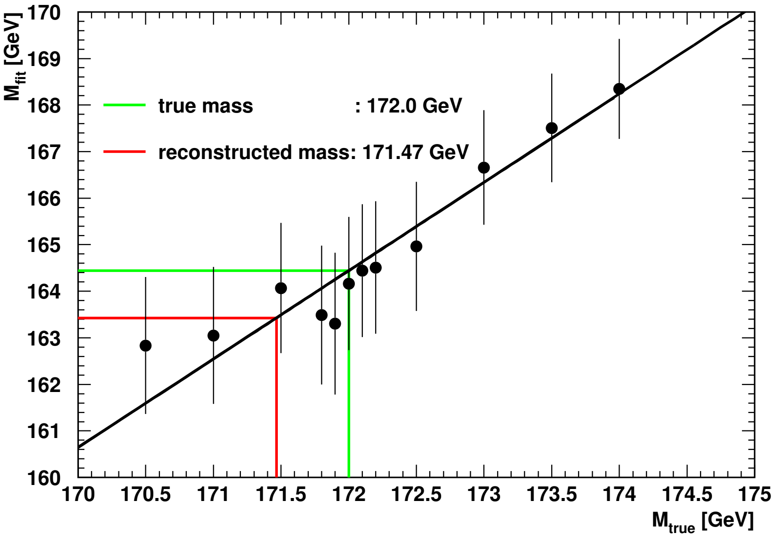

Figure 5.25: Calibration curve showing the dependency between fitted chargino mass, M_{fit}, and true chargino mass, M_{true}. The points with error bars (statistical error) show the fit results from the Monte Carlo samples, while the horizontal and vertical lines indicate the position of the fitted and true chargino mass of the data sample.

$$E^{\star}_{\pi} = \frac{(\sqrt{s} - E^{\gamma})E^{\gamma} - \mathbf{P}^{\pi} \cdot \mathbf{P}^{\gamma}}{2M_{\tilde{\chi}^{\pm}_{1}}} \tag{5.7}$$

where $\mathbf{P}^{\pi}$ describes the three-momentum of the pion and $\mathbf{P}^{\gamma}$ the three-momentum of the ISR photon, using the fact that the ISR photon determines the momentum of the chargino system. In the second step only pions in events around the recoil mass threshold are considered. The charginos in these events are produced almost at rest and $E^{\star}_{\pi}$ corresponds to the mass difference. This is shown in Figure 5.27 (a). Plotted is $E^{\star}_{\pi}$ versus M_{rec}. For all events close to the recoil mass threshold the $E^{\star}_{\pi}$ distribution can be described by a Gaussian with a mean value equals ΔM (Figure 5.27 (b)). All events with

$$M_{\text{rec}} < 2 \times M_{\tilde{\chi}^{\pm}_{1}} + 10\,\text{GeV} \tag{5.8}$$

were considered. Beyond this value the $E^{\star}_{\pi}$ distribution is less Gaussian-like. Although the number of events is small, the Gaussian fit provides an accurate value for the mass difference: $\Delta M_{\text{fit}} = 394 \pm 5\,\text{MeV}$. The error was estimated as $\delta\Delta M_{\text{fit}}/\sqrt{N^{\pi}}$, where N^{π} is the number of pions and $\delta\Delta M_{\text{fit}}$ is the width of the Gaussian fit. The situation becomes worse if beamstrahlung is also taken into account. As indicated in Figure 5.27 (c) the $E^{\star}_{\pi}$ distribution is smeared out. This effect is due to the fact that the chargino system is not well defined anymore in the presence of additional beamstrahlung photons disappearing in the beam pipe. The number of events used for the ΔM fit is drastically reduced and the fit result is less accurate (Figure 5.27 (d)), though

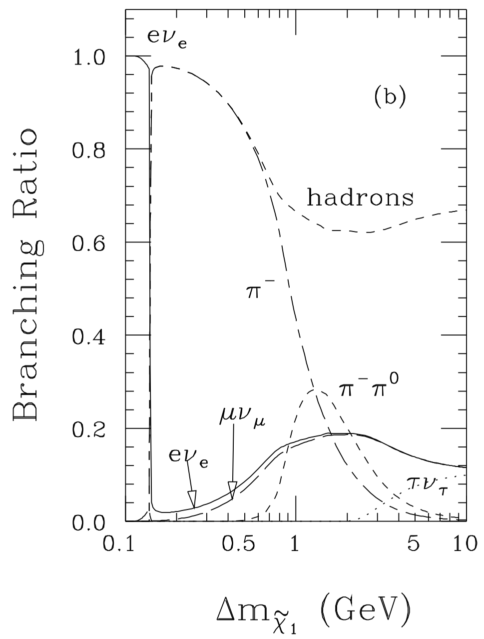

Figure 5.26: Chargino branching ratios as a function of the mass difference as calculated in [33]. The ΔM region of interest, $M_\pi < \Delta M < 1$ GeV, is dominated by chargino decays via a single charged pion.

still acceptable, and slightly shifted to a larger value. The negative effect of beamstrahlung increases with increasing chargino mass. An extreme example is depicted in Figure 5.27 (e) and Figure 5.27 (f). At chargino masses around 230 GeV the Gaussian fit fails and an extraction of the mass difference is impossible.

It was also studied if a reduction of the minimal accessible angle θ_D^{min} and therefore a less tighter cut on E_T^γ helps to increase the number of accepted events and improve the fit results. The minimal accessible angle was changed from $\theta_D^{min} = 30$ mrad, corresponding to $E_T^\gamma \gtrsim 0.029\sqrt{s} \approx 14.6$ GeV, to $\theta_D^{min} = 5$ mrad, corresponding to $E_T^\gamma \gtrsim 0.005\sqrt{s} \approx 2.5$ GeV. The results are compared in Figure 5.28. The effect of a smaller θ_D^{min} on ΔM_{fit} is almost negligible. Although the total number of accepted events increases significantly, the number of events around the M_{rec} threshold only doubles and the fit result does not improve. The reason for this is the energy of the ISR photons in events around the M_{rec} threshold. Events fulfilling the requirement of Equation (5.8) are accompanied by ISR photons with energies ranging from $E^\gamma \approx 122$ GeV to $E^\gamma \approx 132$ GeV. These photons, reconstructed in the ECAL with $|\cos\theta^\gamma| < 0.996$ carry a transverse momentum of at least $p_T \gtrsim 10.9$ GeV. That is to say, most of the events which are additionally selected after relaxing the E_T^γ requirement lie outside of the considered M_{rec} range.

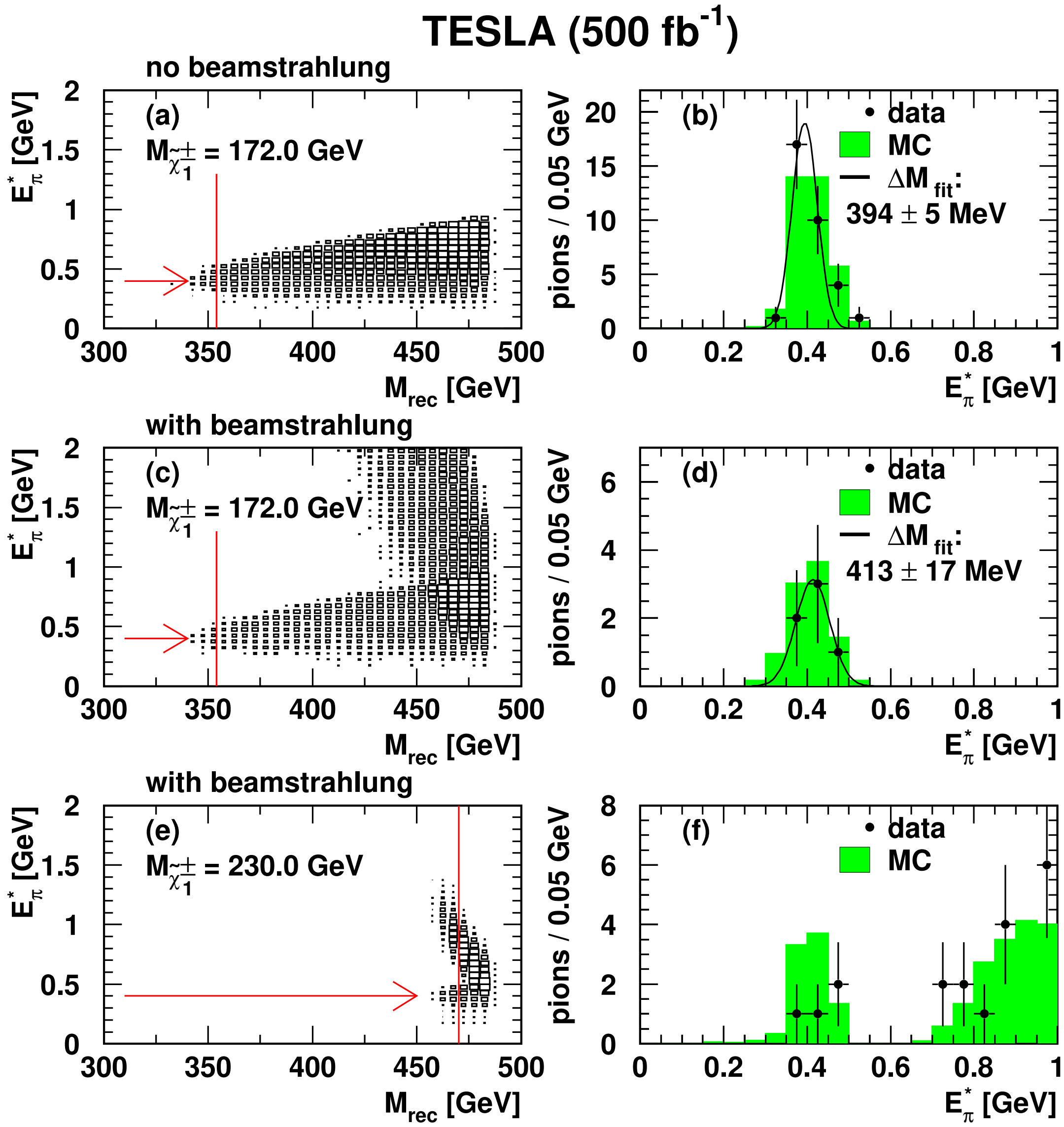

Figure 5.27: Left column: $E^\star_\pi$ versus M_{rec} distribution for various chargino masses and with and without beamstrahlung effects. The arrows indicate the value of ΔM. The vertical line denotes the M_{rec} value below the $E^\star_\pi$ distribution is approximately Gaussian ($2 \times M_{\tilde{\chi}^\pm_1} + 10$ GeV). Right column: $E^\star_\pi$ distributions after the cut on M_{rec}. The TESLA data are indicated by points with error bars (statistical error). The shaded histograms correspond to Monte Carlo simulations.

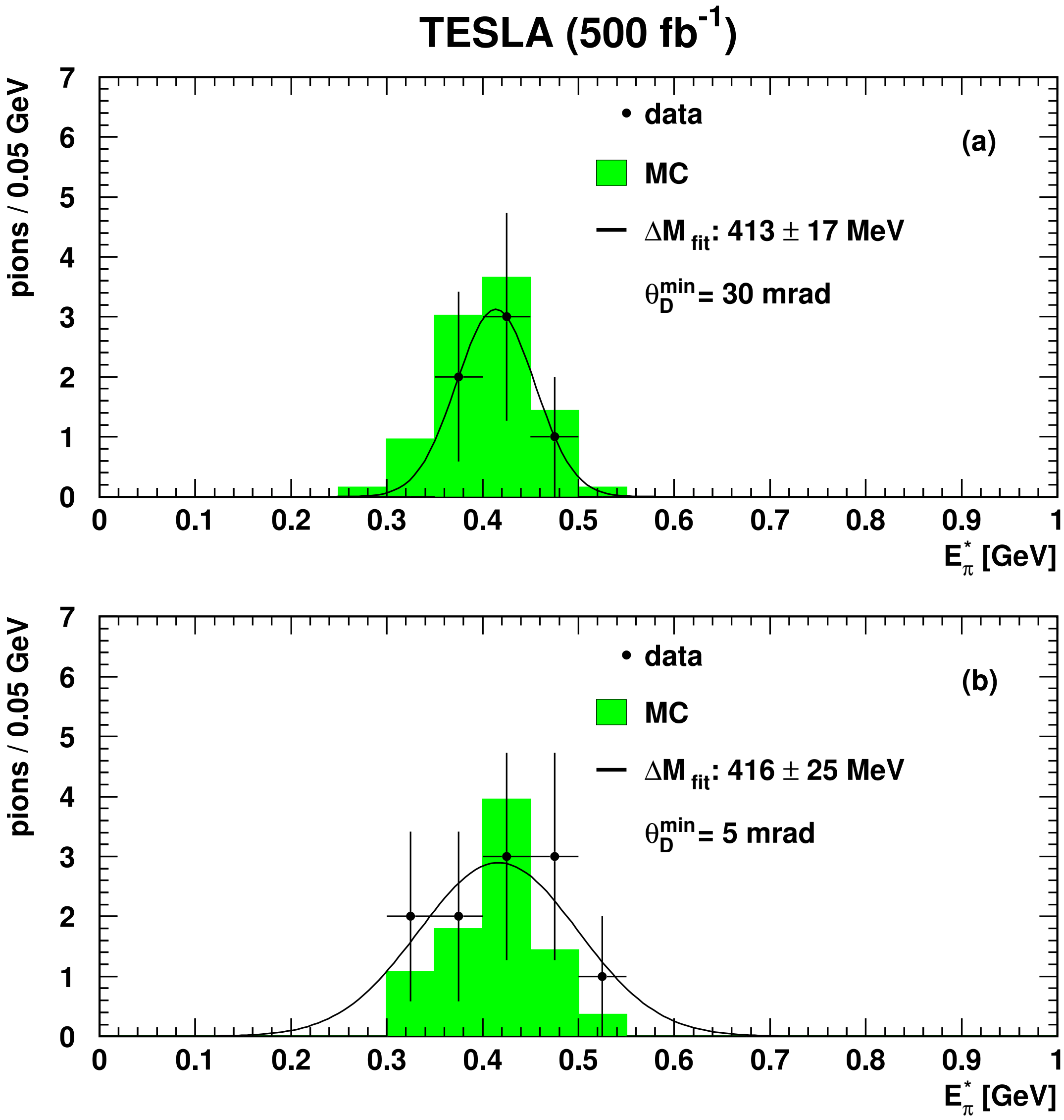

Figure 5.28: $E^\star_\pi$ distribution for two different values of θ_D^{min}. The TESLA data are indicated by points with error bars (statistical error). The shaded histograms correspond to Monte Carlo simulations. Although the smaller angle allows the selection of larger signal sample the effect is only marginal for the $E^\star_\pi$ distribution.

A better reconstruction of the mass difference can be obtained if the full information contained in the $E^{\star}_{\pi}$-$M_{\rm rec}$ distribution is exploited. In a first step the cut requirement in Equation (5.8) is relaxed. Figure 5.29 (a) illustrates the $E^{\star}_{\pi}$ distributions for three different cut values around the $M_{\rm rec}$ threshold. With increasing cut values the shape of the distributions become less and less Gaussian and the means are shifted to higher values. In a second step the mean values, $\bar{E}^{\star}_{\pi}$, of the $E^{\star}_{\pi}$ distribution is plotted against the cut value as shown in Figure 5.29 (b). The error on the mean values is calculated from the root mean squared, RMS, of the distribution: $\delta\bar{E}^{\star}_{\pi} = \mathrm{RMS}/\sqrt{N^{\pi}}$. The linear dependency between $\bar{E}^{\star}_{\pi}$ and the cut value is obvious from Figure 5.29 (b). Finally, a linear fit to the data points allows an extrapolation to a cut value of 0 GeV. From this a mass difference of $\Delta M_{\rm fit} = 401 \pm 7$ MeV was extracted for a minimal accessible angle of $\theta_{\rm D}^{\rm min} = 30$ mrad and including beamstrahlung effects.

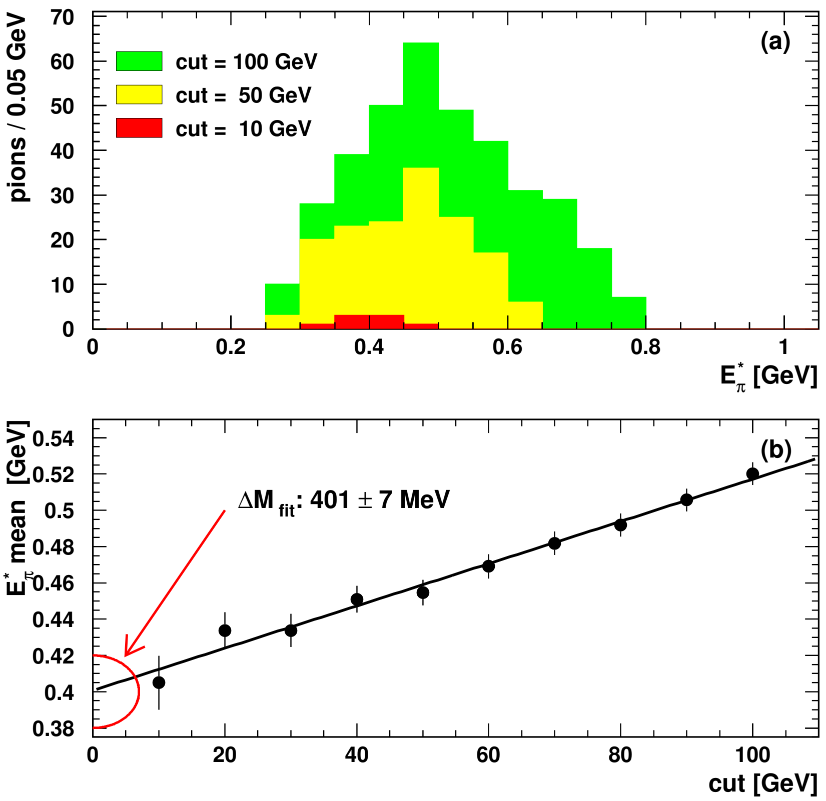

Figure 5.29: (a): $E^{\star}_{\pi}$ distribution for three different cut values around the $M_{\rm rec}$ threshold. With increasing cut values the shape of the distributions become less and less Gaussian and the means are shifted to higher values. (b): mean value of the $E^{\star}_{\pi}$ distribution as a function of the cut values around the $M_{\rm rec}$ threshold. The dots are the data points with error bars derived from the root mean squared of the $E^{\star}_{\pi}$ distributions. The black line indicates the result of a straight line fit to the data points. Extrapolating the fit down to a cut value of 0 GeV results in $\delta\Delta M_{\rm fit} = 401 \pm 7$ MeV.

5.2.5 Discussion of the Results

This Section proved the feasibility of using the ISR method for precision measurements. Several estimates and methods were introduced to extract the chargino mass and mass difference. It was demonstrated that the chargino mass and the mass difference can be extracted with rather simple procedures. The accuracies reached are in the order of $O(1\%)$. These results are very promising since they represent already a rather small upper limit in accuracy for more elaborate approaches.

The ISR method will allow more than measuring chargino and neutralino masses. As discussed in [35] the ISR method will be even a suitable method to extract further SUSY parameters making use of polarised beam and exploiting the dependency of the signal cross-section on the SUSY parameters.

Summary

The reasons to believe that supersymmetry is a basic concept of Nature are manifold. The introduction of an additional symmetry to the Standard Model which connects bosons and fermions leads to an improved predictive power of the theory and solves at the same time a series of conceptual problems of the Standard Model. The Minimal Supersymmetric Standard Model is, from the theoretical point of view, one of the most well elaborated extensions to the Standard Model.

Among the new particles introduced in the MSSM are the charginos and neutralinos. This thesis deals with the search for nearly mass degenerate charginos and neutralinos in e^+e^- collisions and thus with the experimental verification of the existence of supersymmetry. In the case of charginos and neutralinos with small mass differences a dedicated search strategy (the ISR method) is needed since the 'standard' searches are either insensitive (search for heavy stable charged particles) or suffer from a huge background coming mainly from two-photon interactions (search for missing energy plus jets and/or isolated leptons). The expected large chargino production cross-section allows to restrain the search in case of near mass degeneracy to a subsample of signal events. By requiring that the signal events are accompanied by a detectable energetic photon from initial state radiation with a sufficiently large transverse momentum, signal events become distinguishable from two-photon events.

Following this method a search was performed analysing a data set corresponding to $\sim$ 570 pb^{-1} collected in 1998, 1999 and 2000 at centre-of-mass energies between 188 and 209 GeV with the OPAL detector. No evidence was found for charginos and neutralinos with mass differences between 0.5 GeV and 5.0 GeV. The number of selected candidates is in good agreement with the number of expected background events. The level of expected background was of order $O(<10\ \text{events})$. Two different signal scenarios, the higgsino-like and the gaugino-like scenario, were considered. Although the signal selection efficiency was in both scenarios as small as $O(\sim 1\%)$ the number of expected signal events exceeded the background level over the full considered mass difference range almost up to the kinematic limit by a factor of $O(5–10)$.

Chargino production cross-section limits for the case of small mass differences were derived for the MSSM. Chargino mass limits for the unconstrained MSSM and the mSUGRA frameworks were calculated yielding a lower mass limit of 74 GeV at the 95% confidence level for the gaugino-like scenario in case of light sneutrinos ($M_{\tilde{\nu}_e} > 100$ GeV). The derived limits were translated into exclusion regions for the SUSY parameters M_1, M_2, μ and $\tan\beta$. The results were also interpreted in the AMSB framework where exclusion regions for $m_{3/2}$, $\tan\beta$ and m_0 were calculated.

The obtained results are compatible with the results presented by the other LEP experiments, ALEPH, DELPHI and L3. The results of this analysis were provided for a first LEP-wide combination of chargino searches with mass differences ranging from 0.06 GeV to 10 GeV. Using the combined input a lower mass limit for a higgsino-like chargino of 91.9 GeV was computed in this ΔM region.

Though the search result of this analysis is negative, the analysis definitely proved the feasibility of the applied ISR method. The main goal, a coverage of the sensitivity gap between the 'standard' searches, was reached, assuring that a chargino was not missed in the small ΔM regime.

In a next step the results of this analysis shall be combined with the outcomes of the 'standard' chargino searches in order to obtain an overall chargino mass limit setting a benchmark for future experiments.

In the second part of this thesis the use of the ISR method at the next generation Linear Collider TESLA was studied. Rather than the discovery potential the possibility of precision measurements was examined. A detailed investigation of the beam-induced background was performed in order to test the detector performance. Especially the detector forward region was subject of this study which is of particular importance for the ISR method important. It was found that, provided efficient cluster search algorithms for the forward calorimeters can be applied, a larger angular coverage, compared to existent detectors, can be used for the ISR method at the TESLA detector. This will lead to a significant increase of the signal selection efficiency.

With a physics study it was shown that the chargino and neutralino mass can be extracted with the ISR method with an accuracy of $O(1\%)$. These are very promising results motivating further studies in order to answer the question which additional SUSY parameters can be measured using the ISR method.

Bibliography

[1] E. Noether, Kgl. Ges. d. Wiss. Nachrichten, Math-phys. Klasse (1918).

[2] S. R. Coleman and J. Mandula, Phys. Rev. **159**, 1251 (1967).

[3] R. Haag, J. T. Lopuszanski, and M. Sohnius, Nucl. Phys. **B88**, 257 (1975).

[4] P. W. Higgs, Phys. Lett. **12**, 132 (1964).
F. Englert and R. Brout, Phys. Rev. Lett. **13**, 321 (1964).
G. S. Guralnik, C. R. Hagen, and T. W. B. Kibble, Phys. Rev. Lett. **13**, 585 (1964).

[5] G. Kane, *Supersymmetry – Squarks, Photinos, and the Unveiling of the Ultimate Laws of Nature* (Perseus Books Group, 2000).

[6] S. P. Martin, *A Supersymmetry Primer*, hep-ph/9709356.

[7] U. Amaldi, W. de Boer, and H. Furstenau, Phys. Lett. **B260**, 447 (1991).

[8] S. Weinberg, Phys. Rev. **D13**, 974 (1976).
S. Weinberg, Phys. Rev. **D19**, 1277 (1979).

[9] N. Polonsky, Lect. Notes Phys. **M68**, 1 (2001), hep-ph/0108236.

[10] R. S. Chivukula, *Models of Electroweak Symmetry Breaking*, hep-ph/9803219.
K. D. Lane, *Technicolor 2000*, hep-ph/0007304.
C. Quigg, Acta Phys. Polon. **B30**, 2145 (1999), hep-ph/9905369.

[11] N. Arkani-Hamed, S. Dimopoulos, and G. R. Dvali, Phys. Rev. **D59**, 086004 (1999), hep-ph/9807344.

[12] P. H. Frampton and C. Vafa, *Conformal Approach to Particle Phenomenology*, hep-th/9903226.

[13] S. Dawson, *SUSY and Such*, hep-ph/9612229.

[14] M. E. Peskin, *Beyond the Standard Model*, hep-ph/0203114.

[15] D. I. Kazakov, *Beyond the Standard Model (In Search of Supersymmetry)*, hep-ph/001228.

[16] J. R. Ellis, *Supersymmetry for Alp Hikers*, hep-ph/0203114.

[17] J. Wess and B. Zumino, Nucl. Phys. **B70**, 39 (1974).

J. Wess and B. Zumino, Phys. Lett. **B49**, 52 (1974).

[18] D. V. Volkov and V. P. Akulov, JETP Lett. **16**, 438 (1972).

[19] H. P. Nilles, Phys. Rept. **110**, 1 (1984).

[20] H. E. Haber and G. L. Kane, Phys. Rept. **117**, 75 (1985).

[21] D. Z. Freedman, P. van Nieuwenhuizen, and S. Ferrara, Phys. Rev. **D13**, 3214 (1976).

S. Deser and B. Zumino, Phys. Lett. **B62**, 335 (1976).

D. Z. Freedman and P. van Nieuwenhuizen, Phys. Rev. **D14**, 912 (1976).

P. Van Nieuwenhuizen, Phys. Rept. **68**, 189 (1981).

[22] V. Trimble, Ann. Rev. Astron. Astrophys. **25**, 425 (1987).

B. Sadoulet, Rev. Mod. Phys. **71**, S197 (1999).

M. S. Turner and J. A. Tyson, Rev. Mod. Phys. **71**, S145 (1999), astro-ph/9901113.

N. A. Bahcall, J. P. Ostriker, S. Perlmutter, and P. J. Steinhardt, Science **284**, 1481 (1999), astro-ph/9906463.

[23] S. Weinberg, *The quantum theory of fields. Vol. 3: Supersymmetry* (Cambridge, UK: Univ. Pr., 2000).

[24] S. Dimopoulos and D. W. Sutter, Nucl. Phys. **B452**, 496 (1995), hep-ph/9504415.

[25] M. Carena, M. Quiros, and C. E. M. Wagner, Nucl. Phys. **B461**, 407 (1996), hep-ph/9508343.

S. Heinemeyer, W. Hollik, and G. Weiglein, Phys. Lett. **B440**, 296 (1998), hep-ph/9807423.

[26] S. Y. Choi, J. Kalinowski, G. Moortgat-Pick, and P. M. Zerwas, Eur. Phys. J. **C22**, 563 (2001), hep-ph/0108117.

[27] J. R. Ellis, J. S. Hagelin, D. V. Nanopoulos, K. A. Olive, and M. Srednicki, Nucl. Phys. **B238**, 453 (1984).

[28] J. F. Gunion and H. E. Haber, Nucl. Phys. **B278**, 449 (1986).

[29] J. Rosiek, Phys. Rev. **D41**, 3464 (1990).

[30] M. Dine, A. E. Nelson, and Y. Shirman, Phys. Rev. **D51**, 1362 (1995), hep-ph/9408384.

M. Dine, A. E. Nelson, Y. Nir, and Y. Shirman, Phys. Rev. **D53**, 2658 (1996), hep-ph/9507378.

J. A. Bagger, K. T. Matchev, D. M. Pierce, and R.-j. Zhang, Phys. Rev. **D55**, 3188 (1997), hep-ph/9609444.

S. Dimopoulos, S. Thomas, and J. D. Wells, Nucl. Phys. **B488**, 39 (1997), hep-ph/9609434.

S. P. Martin, Phys. Rev. **D55**, 3177 (1997), hep-ph/9608224.

S. Dimopoulos and G. F. Giudice, Phys. Lett. **B393**, 72 (1997), hep-ph/9609344.

G. F. Giudice and R. Rattazzi, Phys. Rept. **322**, 419 (1999), hep-ph/9801271.

[31] L. Randall and R. Sundrum, Nucl. Phys. **B557**, 79 (1999), hep-th/9810155.

[32] G. F. Giudice, M. A. Luty, H. Murayama, and R. Rattazzi, JHEP **12**, 027 (1998), hep-ph/9810442.

[33] C. Chen, M. Drees, and J. Gunion, Phys. Rev. Lett. **76**, 2002 (1996), hep-ph/9512230.

C. H. Chen, M. Drees, and J. F. Gunion, *Addendum/Erratum for 'Searching for Invisible and Almost Invisible Particles at e+e- Colliders' and 'A Non- standard String/SUSY Scenario and its Phenomenological Implications'*, hep-ph/9902309.

[34] K. Riles *et al.*, Phys. Rev. **D42**, 1 (1990).

[35] J. F. Gunion and S. Mrenna, Phys. Rev. **D64**, 075002 (2001), hep-ph/0103167.

[36] C. H. Chen, M. Drees, and J. F. Gunion, Phys. Rev. **D55**, 330 (1997), hep-ph/9607421.

[37] R. Assmann, M. Lamont, and S. Myers, Nucl. Phys. Proc. Suppl. **109**, 17 (2002).

[38] F. Richard (ed.), J. R. Schneider (ed.), D. Trines (ed.), and A. Wagner (ed.), *TESLA Technical Design Report Part I: Executive Summary*, hep-ph/0106314.

[39] R. Brinkmann (ed.) *et al.*, *TESLA: The Superconducting Electron Positron Linear Collider with an Integrated X-Ray Laser Laboratory. Technical Design Report. Part. II: The Accelerator*, DESY-01-011.

[40] J. A. Aguilar-Saavedra *et al.*, *TESLA Technical Design Report Part III: Physics at an e+e- Linear Collider*, hep-ph/0106315.

[41] T. Behnke (ed.), S. Bertolucci (ed.), R. D. Heuer (ed.), and R. Settles (ed.), *TESLA: The Superconducting Electron Positron Linear Collider with an Integrated X-Ray Laser Laboratory. Technical Design Report. Part. IV: A Detector for TESLA*, DESY-01-011.

[42] G. Materlik (ed.) and T. Tschentscher (ed.), *TESLA: The Superconducting Electron Positron Linear Collider with an Integrated X-Ray Laser Laboratory. Technical Design Report. Part V: The X-Ray Free Electron Laser*, DESY-01-011.

[43] H. Abramowicz *et al.*, *TESLA Technical Design Report, Part VI, Appendices*, DESY-01-011.

[44] M. Anselmino *et al.*, *Electron Scattering with Polarized Targets at TESLA*, hep-ph/0011299.

[45] T. Abe *et al.*, *Linear Collider Physics Resource Book for Snowmass 2001*, Resource Book for Snowmass 2001, 30 Jun - 21 Jul 2001, Snowmass, Colorado.

T. Abe *et al.*, *Linear Collider Physics Resource Book for Snowmass 2001. 1: Introduction*, hep-ex/0106055.

T. Abe *et al.*, *Linear Collider Physics Resource Book for Snowmass 2001. 2: Higgs and Supersymmetry Studies*, hep-ex/0106056.

T. Abe *et al.*, *Linear Collider Physics Resource Book for Snowmass 2001. 3: Studies of Exotic and Standard Model Physics*, hep-ex/0106057.

T. Abe *et al.*, *Linear Collider Physics Resource Book for Snowmass 2001. 4: Theoretical, Accelerator, and Experimental Options*, hep-ex/0106058.

[46] N. Akasaka *et al.*, *JLC Design Study*, KEK-REPORT-97-1.

K. Abe *et al.*, *ACFA Linear Collider Working Group*, hep-ph/0109166.

[47] K. Ahmet *et al.*, Nucl. Instrum. Meth. **A305**, 275 (1991).

[48] K. Kawagoe, *Calorimeters in the OPAL Detector*, prepared for 'International Conference on Calorimetry in High-energy Physics', Batavia, IL, 29 Oct - 1 Nov 1990.

[49] P. P. Allport *et al.*, Nucl. Instrum. Meth. **A324**, 34 (1993).

[50] P. P. Allport *et al.*, Nucl. Instrum. Meth. **A346**, 476 (1994).

[51] J. R. Carter *et al.*, Nucl. Instrum. Meth. **A286**, 99 (1990).

[52] M. Hauschild *et al.*, Nucl. Instrum. Meth. **A314**, 74 (1992).

[53] O. Biebel *et al.*, Nucl. Instrum. Meth. **A323**, 169 (1992).

[54] G. Aguillion *et al.*, Nucl. Instrum. Meth. **A417**, 266 (1998).

[55] G. Abbiendi *et al.*, Eur. Phys. J. **C14**, 373 (2000), hep-ex/9910066.

[56] J.-G. An *et al.*, Nucl. Instrum. Meth. **A267**, 396 (1988).

[57] J.-G. An *et al.*, Nucl. Instrum. Meth. **A267**, 386 (1988).

[58] C. Beard *et al.*, Nucl. Instr. Meth. **A286**, 117 (1990).

[59] P. W. Jeffreys *et al.*, Nucl. Instrum. Meth. **A290**, 76 (1990).

[60] M. D. Rousseau, R. M. Brown, P. W. Jeffreys, M. Edwards, and M. Sproston, IEEE Trans. Nucl. Sci. **30**, 479 (1983).

[61] P. W. Jeffreys *et al.*, *A Phototriode Instrumented Lead Glass Calorimeter for Use in a Strong Magnetic Field in OPAL*, submitted to Int. Europhysics Conf. on High Energy Physics, Bari, Italy, Jul 18-24, 1985.

[62] R. M. Brown *et al.*, IEEE Trans. Nucl. Sci. **32**, 736 (1985).

[63] C. J. S. Damerell, *A CCD-Based Vertex Detector for TESLA*, LC-DET-2001-023.

[64] G. Deptuch *et al.*, *Design and Testing of Monolithic Active Pixel Sensors for Charged Particle Tracking*, LC-DET-2001-017.

[65] P. Fischer *et al.*, *A DEPFET Based Pixel Vertex Detector for the Detector at TESLA*, LC-DET-2002-004.

P. Fischer, W. Neeser, M. Trimpl, J. Ulrici, and N. Wermes, *Readout Concepts for DEPFET Pixel Arrays*, hep-ex/0209074.

[66] M. Battaglia *et al.*, *A Pixel Vertex Tracker for the TESLA Detector*, hep-ex/0102046.

[67] J. Hauschildt, *Studies on a Silicon Intermediate Tracker for the TESLA Detector*, LC-DET-2001-036.

[68] T. Behnke *et al.*, *Performance Study of the Proposed TESLA Detector Using a Realistic Track Reconstruction Package*, LC-DET-2001-029.

[69] G. Acquistapace *et al.*, *CMS, The Magnet Project: Technical Design Report*, CERN-LHCC-97-10.

[70] R. Santonico and R. Cardarelli, Nucl. Instrum. Meth. **187**, 377 (1981).

[71] O. Napoly and D. Schulte, *Luminosity Monitor Options for TESLA*, contributed to '19th International Linear Accelerator Conference (Linac 98)', Chicago, Illinois, 23-28 Aug 1998.

[72] R. Nisius, Phys. Rept. **332**, 165 (2000), hep-ex/9912049.

[73] S. Katsanevas and P. Morawitz, Comput. Phys. Commun. **112**, 227 (1998), hep-ph/9711417.

[74] S. Thomas and J. D. Wells, Phys. Rev. Lett. **81**, 34 (1998), hep-ph/9804359.

[75] W. Beenakker *et al.*, *WW Cross-sections and Distributions*, hep-ph/9602351.

[76] H. Baer, F. E. Paige, S. D. Protopopescu, and X. Tata, *ISAJET 7.48: A Monte Carlo Event Generator for pp, anti-p p, and e+e- Reactions*, hep-ph/0001086.

[77] R. Engel, Z. Phys. **C66**, 203 (1995).

R. Engel, J. Ranft, and S. Roesler, Phys. Rev. **D52**, 1459 (1995), hep-ph/9502319.

R. Engel and J. Ranft, Phys. Rev. **D54**, 4244 (1996), hep-ph/9509373.

[78] G. Marchesini *et al.*, Comput. Phys. Commun. **67**, 465 (1992).

[79] J. Vermaseren, Nucl. Phys. **B229**, 347 (1983).

[80] F. A. Berends, P. Daverveldt, and R. Kleiss, Nucl. Phys. **B253**, 421 (1985).

F. A. Berends, P. H. Daverveldt, and R. Kleiss, Comput. Phys. Commun. **40**, 271 (1986).

F. A. Berends, P. H. Daverveldt, and R. Kleiss, Comput. Phys. Commun. **40**, 285 (1986).

F. A. Berends, P. H. Daverveldt, and R. Kleiss, Comput. Phys. Commun. **40**, 309 (1986).

[81] M. Skrzypek, S. Jadach, W. Placzek, and Z. Was, Comput. Phys. Commun. **94**, 216 (1996).

M. Skrzypek, S. Jadach, M. Martinez, W. Placzek, and Z. Was, Phys. Lett. **B372**, 289 (1996).

[82] J. Fujimoto *et al.*, Comput. Phys. Commun. **100**, 128 (1997), hep-ph/9605312.

[83] S. Jadach, B. F. L. Ward, and Z. Was, Comput. Phys. Commun. **130**, 260 (2000), hep-ph/9912214.

[84] G. Montagna, M. Moretti, O. Nicrosini, and F. Piccinini, Nucl. Phys. **B541**, 31 (1999), hep-ph/9807465.

[85] D. Karlen, Nucl. Phys. **B289**, 23 (1987).

[86] S. Jadach, W. Placzek, and B. F. L. Ward, Phys. Lett. **B390**, 298 (1997), hep-ph/9608412.

[87] F. A. Berends and R. Kleiss, Nucl. Phys. **B186**, 22 (1981).

[88] D. Schulte, *Study of Electromagnetic and Hadronic Background in the Interaction Region of the TESLA Collider*, PhD thesis, University of Hamburg, 1997, DESY-TESLA-97-08.

[89] J. Allison *et al.*, Comput. Phys. Commun. **47**, 55 (1987).

J. Allison *et al.*, Nucl. Instrum. Meth. **A317**, 47 (1992).

[90] R. Brun, R. Hagelberg, M. Hansroul, and J. C. Lassalle, *GEANT: Simulation Program for Particle Physics Experiments. User Guide and Reference Manual*, CERN-DD-78-2-REV.

[91] C. Hawkes, D. Lellouch, M. Redmond, O. Schaile, and M. Schröder, *ROPE Users' Guide*, OPAL-Offline Note16/OFFL-0487, last update March 2002.

[92] T. Behnke and G. A. Blair, *BRAHMS - Version 102: A Monte Carlo for a detector at a 500-GeV to 800-GeV linear collider*, LC-PHSM-2001-005.

[93] M. Pohl and H. J. Schreiber, *SIMDET - Version 3: A parametric Monte Carlo for a TESLA detector*, DESY-99-030.

M. Pohl and H. J. Schreiber, *SIMDET - Version 4: A parametric Monte Carlo for a TESLA detector*, hep-ex/0206009.

[94] S. Mihara and S. Yamashita, *MT 3.00 A new Algorithm to Calculate Energy Flow Based on MT Package*, OPAL Technical Note 574.

T. Omori, S. Asai, and I. Nakamura, *Attempt to Compensate Energy in OPAL Calorimeter Complex Based on MT Package*, OPAL Technical Note 447.

T. Omori, S. Asai, I. Nakamura, and I. Yamashita, *A Matching Algorithm: MT Package*, OPAL Technical Note 381.

[95] G. Abbiendi *et al.*, Eur. Phys. J. **C16**, 185 (2000), hep-ex/0002012.

[96] G. Abbiendi *et al.*, Eur. Phys. J. **C18**, 253 (2000), hep-ex/0005002.

[97] D. Ward and C. Ward, *WWFIX – Fixups for the W Mass Analysis*, OPAL Technical Note 715.

[98] T. Junk, Nucl. Instrum. Meth. **A434**, 435 (1999), hep-ex/9902006.

[99] R. D. Cousins and V. L. Highland, Nucl. Instrum. Meth. **A320**, 331 (1992).

[100] A. Heister *et al.*, Phys. Lett. **B533**, 223 (2002), hep-ex/0203020.

[101] J. Abdallah *et al.*, *Searches for Supersymmetric Particles in e+e- Collisions up to 208 GeV, and Interpretation of the Results within the MSSM*, 2002-027-CONF-561.

[102] P. Achard *et al.*, *Search for Supersymmetry in e+e- Collisions at* $\sqrt{s} = 202 - 208$ *GeV*, L3 note 2707.

[103] K. Yokoya and P. Chen, *Beam-Beam Phenomena in Linear Colliders*, Tsukuba KEK - KEK-Prepr.-91-002 (91/04,rec.Jul.) 36 p.

[104] M. Venturini and W. Kozanecki, *The Hourglass Effect and the Measurement of the Transverse Size of Colliding Beams by Luminosity Scans*, Presented at IEEE Particle Accelerator Conference (PAC2001), Chicago, Illinois, 18-22 Jun 2001.

[105] O. Napoly, I. Reyzl, and N. Tesch, *Interaction Region Layout, Feedback and Background Issues for TESLA*, Prepared for 4th International Workshop on Linear Colliders (LCWS 99), Sitges, Barcelona, Spain, 28 Apr - 5 May 1999.

[106] G. Wagner, *Neutron Background Studies at the TESLA Collider*, LC-DET-2001-048.

[107] A. Fasso, A. Ferrari, J. Ranft, and P. R. Sala, Program FLUKA99, manual and code available from the authors.

A. Fasso, A. Ferrari, J. Ranft, and P. R. Sala, *FLUKA: Present Status and Future Developments*, Talk given at 4th International Conference on Calorimetry in High-energy Physics, La Biodola, Italy, 19-25 Sep 1993.

[108] C. Hensel, *Beam Induced Background at a TESLA Detector*, LC-DET-2000-001.

[109] P. Chen, Disruption, beamstrahlung and beamstrahlung pair creation, contributed to DPF Summer Study Snowmass '88, High Energy Physics in the 1990's, Snowmass, Colo., Jun 27 - Jul 15, 1988.

[110] M. S. Zolotorev, E. A. Kuraev, and V. G. Serbo, *Estimates of Electromagnetic Background Processes for the VLEPP Project*, SLAC-TRANS-0227.

[111] V. B. Berestetsky, E. M. Lifshitz, and L. P. Pitaevsky, *Quantum Electrodynamics (Course Of Theoretical Physics, 4)* (Oxford, Uk: Pergamon, 1982).

[112] D. Schulte, *Simulation des Untergrundes durch inkohärente Paaerzeugung in Linearbeschleunigern*, Diploma thesis, University of Hamburg, 1993, TESLA 93-39.

[113] P. Chen, T. Tauchi, and D. V. Schroeder, *Pair Creation at Large Inherent Angles*, In 'Snowmass 1990, Proceedings, Research directions for the decade' 751-756.

[114] R. Brinkmann (ed.), G. Materlik (ed.), J. Rossbach (ed.), and A. Wagner (ed.), *Conceptual Design of a 500 GeV e+ e- Linear Collider with Integrated X-Ray Laser Facility. Vol. 1, 2*, Hamburg, Germany: DESY (1997) 1183 p. DESY-97-048 1183 p. (ECFA 97-182).

[115] B. C. Allanach *et al.*, *The Snowmass Points and Slopes: Benchmarks for SUSY Searches*, hep-ph/0202233.

Danksagung

An dieser Stelle möchte ich all jenen danken, die mich in den letzten Jahren direkt, indirekt, bewusst oder unbewusst unterstützt und damit die Fertigstellung dieser Arbeit erst erlaubt haben.
Mein besonderer Dank gilt Herrn Prof. Dr. Rolf-Dieter Heuer für seine Unterstützung und Förderung während all der Jahre. Der Besuch von Meetings, Sommerschulen und Konferenzen und ein verlängerter Aufenthalt am CERN waren sehr motivierend und wurden erst durch ihn ermöglicht.
Ich möchte mich bei Frau Prof. Dr. Beate Naroska, Herrn Prof. Dr. Friedrich-Wilhelm Büßer und Herrn Dr. Eckhard Fretwurst für die Erstellung von Gutachten beziehungsweise für die Leitung der Disputation bedanken.
Dr. Klaus Desch danke ich für seine hervorragende, detailierte und stets geduldige Betreuung. Ohne die Anleitung von Dr. Ties Behnke wären viele meiner TESLA-Studien gar nicht erst möglich gewesen.
Alle Mitglieder meiner Hamburger Arbeitsgruppe, FLC, haben dazu beigetragen, dass ich die letzten Jahre in einer außergewöhnlichen Arbeitsatmosphäre verbracht habe. Ein herzliches Dankeschön geht an all diejenigen, mit denen ich das Vergnügen hatte, das Büro zu teilen. Markus, Mathieu und Wolfgang gebührt großer Dank. In vielen Diskussionen und Gesprächen, sowohl während als auch nach der Arbeitszeit, habe ich ihre Freundschaft schätzen gelernt. Petra danke ich für ihre Freundschaft und die Zeit, die ich mit ihr als Kollege und Mitbewohner verbringen durfte.
Nicht unerwähnt sollen weitere (Ex-)DESY-Kollegen bleiben. Christian, Nicolai und Rainer haben auf ihre eigene Art zum Gelingen dieser Arbeit beigetragen.
Auch durch die OPAL Kollaboration am CERN, bei deren Mitgliedern ich mich für die freundliche Aufnahme bedanke, habe ich große Unterstützung erfahren. Ich möchte mich bei Dr. Rob McPherson für sein reges Interesse und seine Unterstützung während der letzten Jahre bedanken. Dr. Christoph Rembser hatte einen sehr motivierenden Einfluss auf meine Arbeit. Für seine Hilfe möchte ich mich ebenso bedanken wie für die Hilfe von Dr. Katja Klein.
Trotz oder vielleicht sogar wegen ihres fehlenden direkten Bezugs zur Materie, hatte eine ganze Reihe von Menschen einen nicht unerheblichen Anteil am Gelingen dieser Arbeit. Für ihre Freundschaft und ihren Zuspruch möchte ich mich bedanken bei Christian, Ebba, Guido, Harald, Jörg, Stephie und Tülay.
Mein gesamtes Studium wäre jedoch ohne meine Familie, bei der ich mich ganz besonders bedanken möchte, gar nicht erst möglich gewesen.

it's times like these you learn to live again
F. F.

Erklärung: Hiermit versichere ich, die vorliegende Arbeit unter Angabe der wesentlichen Literatur selbstständig angefertigt zu haben.

(Carsten Hensel)